

Copyright  
by  
Bryce Hedrick Wagner III  
2010

**The Dissertation Committee for Bryce Hedrick Wagner III Certifies that this  
is the approved version of the following dissertation:**

**An Analysis of Salt Welding**

**Committee:**

---

Martin Jackson, Supervisor

---

Mark Cloos, Co-Supervisor

---

Mike Hudec

---

Ron Steel

---

Mrinal Sen

---

Frank Peel

**An Analysis of Salt Welding**

**by**

**Bryce Hedrick Wagner III, B.S.**

**Dissertation**

Presented to the Faculty of the Graduate School of

The University of Texas at Austin

in Partial Fulfillment

of the Requirements

for the Degree of

**Doctor of Philosophy**

**The University of Texas at Austin**

**May, 2010**

## **Dedication**

*To Amanda, my incredible wife.*

*May we continue to walk beside each other, always and forever.*

*To my mother and father, Bryce Jr. and Kathy.*

*Your continued support and love inspire me to this day.*

*To my grandparents Marilyn and Dan Davis, whose zest for life was exceeded  
only by their love for family. We miss you very much.*

## **Acknowledgements**

Over the course of the last four years, I have spent countless hours, long days, and late nights preparing and assembling this dissertation, but I would be lying if I told you I did it alone. I'd like to take this opportunity to thank the great many individuals and organizations that made my dissertation research possible.

First and foremost, I owe an incredible debt of gratitude to my research supervisors Dr. Martin Jackson at the Bureau of Economic Geology and Dr. Mark Cloos in the Department of Geological Sciences, who guided my dissertation research and professional development. Martin has been my day-to-day supervisor and his creativity and knowledge of salt tectonics and structural geology have been an inspiration since day one. Meetings and discussions with Martin are always enjoyable and productive, and he has proven a diligent supervisor, mentor, and friend. Mark has served as my liaison to the Department of Geological Sciences and is a constant reminder of my obligations as a student and as a budding geoscientist. What his direct questions and candid reviews lack in finesse he more than makes up for with his incredible breadth of knowledge and above all else a desire for each student to perform at their best. Many students in the graduate school

consider Mark's presence on a committee a hassle; I consider it a blessing. It is my privilege to have worked with you both these past four years.

I owe very special thanks to Dr. Mike Hudec at the Bureau of Economic Geology, whose expertise in practical aspects of salt tectonics is unparalleled. Mike's role in my dissertation research was limited primarily to serving on my dissertation committee, but his role in my development as a geoscientist has been invaluable. In a project wholly unrelated to my dissertation research, Mike and I completed two weeks of field work analyzing folds and fault along the north flank of the Onion Creek Diapir in the Paradox Basin, Utah. Mike also invited me to attend and assist with a field trip he runs to the area. I thoroughly enjoyed the time we spent working together in Utah, even when I was wheezing and panting my way up a goat trail to obtain last field measurement of the day.

Special thanks to Dr. Ron Steel from the Department of Geological Sciences, Dr. Mrinal Sen of the Institute for Geophysics, and Dr. Frank Peel of BHP Billiton for serving on my dissertation committee. Each of you greatly improved the quality of the dissertation with insightful reviews. Frank Peel also provided a number of unique ideas that greatly enhanced the content of the dissertation. Thank you all for your time.

I am also grateful to the other members of the Applied Geodynamics Laboratory at the Bureau of Economic Geology, including Tim Dooley, Angela McDonnell, Nancy Cottington, Jose Dirkzwager, Monica Pequeno, and Mike Braunschiedel who either facilitated my research or otherwise made my experience in the group that much more enjoyable.

Many of the concepts included in the dissertation were first conceived during my summers spent as an intern at Devon Energy Corporation and I'd like to thank the entire Brazil Exploration Team for providing a comfortable and intellectually stimulating home away from home. My supervisor Dr. Wagner Peres, my mentors Ron McWhorter and Wendy Sudhakar, and my teammates Joe Paul, Harry Aasmayr, Glenn Latimer, Gerald Montgomery, Joe Hayden, Erin Duerichen, Trevor Aitken, Mark Houston, Ken German, and Raquel Janoe all contributed in some fashion to my dissertation research and my experience as an intern. Thank you all for accepting me as one of your own, and I wish you all the best of luck in the future.

No modern scientific venture would be complete without technical challenges and setbacks, and Chuck Garza, Reuben Reyes, and Dallas Dunlap at the Bureau of Economic Geology proved invaluable to getting my work back on track after the many unavoidable software glitches, server

crashes and the like. Dallas Dunlap also provided hands-on training and troubleshooting for a variety of software packages used throughout my research, and Cari Breton provided support for ArcGIS. Many other staff members at the Bureau of Economic Geology were responsible for the behind-the-scenes operations of my employment as a research assistant, including Sammy Jacobo, Caryn Mills, and Claudia Gerardo who made even the most frustrating aspects of bureaucracy and paperwork pleasurable.

I'd also like to thank Dr. Robert Laudon and Dr. John Hogan at the Missouri University of Science and Technology who first introduced me to salt tectonics and structural geology and inspired me to pursue these interests as a graduate student.

Finally, I must thank the many students and professors at the Jackson School of Geosciences who became colleagues and friends during my time at the University of Texas at Austin. Daily interaction and weekly meetings with the "Cloos group" forced me to work diligently and think critically about my research, and I would not be here today without the friendship and support of Adam Lambert, Ryan Coppersmith, Andy Dewhurst, Ethan Lake, Esti Ucar, Gareth Cross, Julie Jackson, and Keith Trasko. I would like to extend my sincere appreciation to Ben Andrews, Miriam Barquero-Molina,

Erin Eastwood, Ryan Ewing, Jamie Levine, John Singleton, Kylara Martin, and Vishal Maharaj; you come from many disciplines but are particularly talented geoscientists and it has been my pleasure to interact with you. To all the other students with whom I have worked, I thank you for your support as well. Though the focus of graduate school is not intended to be coursework, I would also like to thank Dr. Randall Marrett, Dr. Sharon Mosher, Dr. Bill Carlson, Dr. David Mohrig, Dr. Gary Kocurek, Dr. Charlie Kerans, and Dr. William Fisher for giving inspired lectures and reminding me of my passion for all subjects geoscience.

This work was funded primarily by the Department of Geological Sciences at the University of Texas at Austin and the Applied Geodynamics Laboratory at the Bureau of Economic Geology. Additional support was provided by scholarships through the Department of Geological Sciences (Michael Bruce Duchin Endowed Scholarship, Devon Energy Scholarship), the Society of Exploration Geophysics Foundation (ExxonMobil Upstream Research Grant, Dallas Geophysical Society Scholarship), and through the ConocoPhillips SPIRIT Scholars Program.

To all of you, your support the past four years means the world to me, and I could not have done it without you.

## Preface

I first arrived as a PhD student at the University of Texas at Austin in the fall of 2006. I knew I wanted to study salt tectonics, but my exact path in that field was unclear. In November 2006, I attended the annual meeting of the Applied Geodynamics Laboratory, a salt tectonics research consortium run by Martin Jackson and Mike Hudec at the Bureau of Economic Geology. I was immediately intrigued by salt welds, areas of thinned or completely vanished salt.

In the fall of 2007 I wrote my research proposal in which I somewhat haphazardly planned to throw everything research tool I could think of at welds; numerical modeling, finite element modeling, seismic interpretation, geophysical modeling, sequence stratigraphy, analog modeling, and even field work. Some of these tools helped mold the final dissertation, but several of them occupied many hours only to turn into dead ends.

In the end, I settled on the results borne from numerical modeling, seismic interpretation, and geophysical modeling. The results presented herein represent only a portion of the many research avenues I pursued during this dissertation, but I believe they provide the greatest contribution to our understanding of salt welds.

# An Analysis of Salt Welding

Publication No. \_\_\_\_\_

Bryce Hedrick Wagner III, Ph.D.

The University of Texas at Austin, 2010

Supervisors: Martin Jackson

Mark Cloos

Salt can be removed by viscous flow and dissolution to form a *salt weld*. A *complete weld* forms when salt is completely removed by these processes. Where salt removal is incomplete, a *partial weld* forms. Though welds are frequently mentioned in the literature, the details of weld formation and the properties of salt welds are poorly understood.

In Chapter 1, I use analytical and numerical models to quantify the role of viscous flow during salt welding. Where salt flow is limited by boundary drag against the salt contacts, evacuation is slow and up to ~50 m of salt will be left behind in a partial weld. Where salt flow is laterally unrestricted, a vanishingly thin ( $\ll 1$  m) smear of salt will remain. I conclude that layer-

parallel wall rock translation or dissolution must act to remove any remnant salt to create a complete weld.

In Chapter 2, I characterize partial welds containing halite and anhydrite on reflection seismic data by treating welds as thin beds. Below the temporal resolution of reflection seismic data, typically ~25-50 m for modern surveys with peak frequencies of ~10-30 Hz, reflections from the upper and lower evaporite contacts converge and interfere to form a single composite reflection. Thus, partial and complete welds are typically indistinguishable using travel-time differences alone. I then use amplitude information from synthetics and seismic examples to estimate remnant evaporite thickness.

In Chapter 3, I investigate fluid flow near and through salt welds. I conclude dissolution during boundary flow can remove up to a few meters of salt per million years. Though dissolution plays a volumetrically insignificant but important role in weld formation, as runaway dissolution can create pathways for focused cross-weld migration of subsurface fluids. I identify features that influence cross-weld migration of subsurface fluids and then develop an empirical relationship between weld geometry and the tendency seal or leak hydrocarbons. I find that in the Campos Basin, offshore Brazil, salt welds containing remnant evaporites thinner than ~50 m that are broader than ~25 km<sup>2</sup> in area are likely to leak.

## Table of Contents

List of Tables.....	xv
List of Figures .....	xvi
<b>INTRODUCTION</b>	<b>1</b>
<b>CHAPTER 1: VISCOUS FLOW DURING SALT WELDING</b>	<b>7</b>
Abstract.....	7
Introduction .....	8
Viscous Flow .....	16
Hydraulic-Gradient Boundary Conditions.....	19
Displacement Boundary Conditions.....	28
Thinning of a Single Salt Layer .....	32
Thinning and Layer-Parallel Wall Rock Translation .....	46
Thinning of a Multilayered Evaporite Sequence .....	54
Discussion.....	69
Conclusions .....	73
Acknowledgements.....	74
<b>CHAPTER 2: SEISMIC CHARACTERIZATION OF SALT WELDS IN SALT TECTONICS REGIMES</b>	<b>75</b>
Abstract.....	75
Introduction .....	76
Seismic Properties of Evaporites, Welds and their Surroundings.....	83
Evaporite Welds as Thin Beds.....	94
Estimating Evaporite Thickness.....	106
Conclusions and Recommendations .....	116
Acknowledgements.....	118

<b>CHAPTER 3: SALT WELDS, DISSOLUTION, AND HYDROCARBON MIGRATION</b>	<b>119</b>
Abstract .....	119
Introduction.....	120
Fluid Flow and Salt.....	124
Dissolution.....	131
Hydrocarbon Migration Through Salt Welds .....	144
Case Study: Campos Basin, offshore Brazil .....	150
Conclusions.....	155
Acknowledgements .....	156
Appendix A: Viscous Flow Equations and Error Analysis .....	157
Temporal and Spatial Accelerations.....	157
Numerical Approximations .....	163
Appendix B: Viscous Flow MATLAB Code 1 .....	165
Appendix C: Viscous Flow MATLAB Code 2.....	168
Appendix D: Synthetic Seismogram MATLAB Code .....	173
Appendix E: Synthetic Seismogram MADAGASCAR Code .....	176
Glossary .....	182
References .....	183
Vita .....	218

## List of Tables

Table 1.1 Effect of shear displacement on welding.....	51
Table 1.2 Dynamic viscosities of common evaporites .....	55
Table 3.1 Brine density and viscosity used to model dissolution .....	139

## List of Figures

Figure 1.1 Examples of salt welds .....	12
Figure 1.2 Schematic cross sections illustrating model boundary conditions .....	15
Figure 1.3 Coordinate system and variables used to model viscous flow under hydraulic-gradient boundary conditions .....	21
Figure 1.4 Reynolds number during viscous flow of salt .....	23
Figure 1.5 Schematic cross section illustrating the difference between a traditional <i>salt weld</i> and a <i>fault weld</i> .....	25
Figure 1.6 Schematic diagram of model geometries used to model viscous flow during salt welding .....	34
Figure 1.7 Evolution of a single salt layer during viscous evacuation .....	36
Figure 1.8 Schematic cross section illustrating minibasin deformation during viscous evacuation .....	40
Figure 1.9 Sensitivity of salt evacuation to model parameters .....	43
Figure 1.10 Sensitivity of salt evacuation to initial salt thickness .....	45
Figure 1.11 Schematic cross sections illustrating the formation of a fault weld during homogenous stretching of the overburden .....	48
Figure 1.12 Schematic cross sections illustrating the formation of a fault weld during heterogenous stretching of the overburden .....	50
Figure 1.13 Evolution of a salt layer thinning due to viscous evacuation and layer-parallel wall rock displacement .....	53

Figure 1.14 Velocity profiles through multilayered evaporites with varying rheology and thickness .....	59
Figure 1.15 Evolution of multilayered evaporite thickness during welding .....	61
Figure 1.16 Differential evacuation of multilayered evaporites .....	64
Figure 1.17 Crossplot of volume % anhydrite and evaporite thickness from forty-one wells data from the Campos Basin, offshore Brazil.....	66
Figure 1.18 Potential effect of thin, low-viscosity evaporites on borehole stability.....	68
Figure 1.19 Welding in natural geometries that minimize the limitations of boundary drag .....	72
Figure 2.1 Example reflection-seismic section through a seismic weld .....	78
Figure 2.2 Crossplot of resolvable halite thickness and peak frequency.....	82
Figure 2.3 Examples of the complicated internal structure of welds .....	88
Figure 2.4 Synthetic seismogram illustrating wave propagation through a complicated partial weld .....	90
Figure 2.5 Plot of reflection coefficients between common lithologies and halite or anhydrite .....	93
Figure 2.6 Inverted wedge model used to generate synthetic seismograms .....	95
Figure 2.7 Synthetic seismograms of a Type I weld .....	98
Figure 2.8 Synthetic seismograms of a Type II weld .....	101
Figure 2.9 Synthetic seismograms of a Type III weld .....	103
Figure 2.10 Synthetic seismograms of a Type IV weld.....	105

Figure 2.11 Example Type I weld from the Gulf of Mexico .....	109
Figure 2.12 Example Type IV weld from the Gulf of Mexico .....	112
Figure 2.13 Example Type III weld from the Campos Basin .....	115
Figure 3.1 Schematic cross section illustrating hypothetical hydrocarbon migration through permeable salt welds .....	123
Figure 3.2 Schematic diagram illustrating types of fluid flow near salt structures .....	126
Figure 3.3 Hydrocarbon sealing capacity of continuous halite .....	130
Figure 3.4 Crossplot of brine composition and brine volume required to completely dissolve 1 km <sup>3</sup> of halite .....	134
Figure 3.5 Schematic cross-section illustrating the development of a caprock sheath during dissolution by boundary flow .....	137
Figure 3.6 Model of dissolution by boundary flow .....	141
Figure 3.7 Model of dissolution by diffuse crossflow .....	143
Figure 3.8 Schematic cross sections illustrating factors that control weld permeability .....	146
Figure 3.9 Schematic cross section illustrating the relationship between subhorizontal weld timing, sedimentation, and hydrocarbon expulsion .....	148
Figure 3.10 Basemap of the Campos Basin, offshore Brazil including wells and welds used for this study .....	153
Figure 3.11 Crossplot of remnant evaporite thickness and partial weld area .....	154
Figure A.1 First spatial acceleration term in Equation A.1 .....	160
Figure A.2 Second spatial acceleration term in Equation A.1 .....	162
Figure A.3 Crossplot of time step and model deviation for forward-difference approximation .....	164

## INTRODUCTION

*Salt tectonics* is a general term referring to the deformation of evaporites, especially rock salt (e.g., Hudec and Jackson, 2007). Salt, used here to describe any rock composed primarily of halite, is capable of crystal-plastic creep at surface temperatures and differential stresses less than 1 MPa. Dry salt creeps by dislocation climb along the [110] crystallographic plane and its equivalents (e.g., Carter and Hansen, 1983). In salt with as little as 0.05 wt. % water, creep is dominated by solution-precipitation (Urai et al., 1986) and grain boundary diffusion (Ter Heege et al., 2005a). Salt can be approximated as a Newtonian viscous fluid in which viscosity is constant with respect to strain rate.

Early salt-tectonics research approximated salt and the surrounding sediments behaving as viscous fluids over geologic time. Nettleton (1934) proposed that the buoyancy of low-density salt confined by high-density overburden resulted in a Rayleigh-Taylor instability, causing salt diapirs to rise as the two fluids overturned. However, in many salt basins, such as the Gulf of Mexico, salt can flow horizontally up to ~200 km but flow vertically only a few kilometers (e.g., Worrall and Snelson, 1989). Furthermore, shallow (< 1-2 km deep) salt diapirs rise well above the depths of density inversion for siliclastic sediments (~2-4 km depending on grain density, Hudec et al., 2009). These phenomena cannot be explained by buoyancy, so it is now widely accepted that

while buoyancy effects are important in some types of salt tectonics, such as active diapirism (e.g., Vendeville and Jackson, 1992a; b), basin-scale salt flow is commonly the result of differential loading by uneven sedimentation (e.g., Cohen and Hardy, 1996) or regional tectonism (e.g., Jackson et al., 2003). This understanding, coupled with the proliferation of quality three-dimensional seismic data, laid the foundation for modern salt research.

The concept of vanished salt had been known for some time (e.g., Trusheim, 1960), but salt welds were first formally named and described by Jackson and Cramez (1989). They defined a *salt weld* as the structure joining “two rock volumes formerly separated by salt.” Jackson and Cramez (1989) classified welds based on structural position; a *primary weld* forms in the autochthonous source layer, a *secondary weld* is a subvertical weld that forms in a salt stock or wall, and a *tertiary weld* forms in an allochthonous salt sheet or canopy. Rowan et al. (1999) classified fault-related welds on seismic data in the Gulf of Mexico based on the stratigraphic and structural architecture of the overburden. Beyond these attempts at classification and general usage in the literature, salt weld research has focused on seismic examples from salt basins around the world and a few field examples including those in the La Popa Basin, northern Mexico (e.g., Giles and Lawton, 1999) and the Flinders Ranges, Australia (e.g., Dyson and Rowan, 2004).

Salt welds record the expulsion of vast volumes of salt (Jackson and Cramez, 1989), influence the evolution of nearby salt structures (e.g., Ge and Jackson, 1998), juxtapose widely separate rock bodies (e.g., Rowan et al., 1999), control regional sedimentation patterns (e.g., Rowan and Weimer, 1998), and act as either barriers or pathways for migrating hydrocarbons and mineralizing fluids (e.g., Rowan, 2004). Salt welds are also internally complex and heterogeneous structures. Two main processes are known to produce welds, 1) viscous flow and 2) dissolution. Viscous flow forms folds and dismembers competent beds within the evaporite layer, resulting in high strains within and near the weld. Dissolution near the surface due to meteoric water can remove remaining soluble minerals, leaving insoluble residues, and (in welds shallower than ~1 km) voids or collapse structures. At depths > ~1 km, dissolution is a problem of water flux and geochemistry.

Alone, neither of these processes appears sufficient to completely remove salt to form a weld. Viscous flow is limited by boundary drag along the salt contacts: the thinner the salt the more difficult it becomes to squeeze out. Layer-parallel wall rock translation can avoid some of the limitations of boundary drag, but requires serendipitous geometry and displacement conditions. Dissolution requires the flux of large volumes of groundwater (greater than ~6 times the volume of salt being dissolved) that are undersaturated with respect to halite. Because of these limitations and numerous natural examples of “salt welds” that

contain some remnant salt, I introduce new terminology for clarity (see Glossary). Here, a *complete weld* contains no remnant salt and is equivalent to the classic definition by Jackson and Cramez (1989). In contrast, a *partial weld* contains up to ~50 m of remnant evaporites. Furthermore, I expand the term *salt weld* to refer to both complete and partial welds.

Weld completeness is a matter of utility and scale. For example, a weld is mechanically complete when any remnant evaporites can no longer be appreciably evacuated by viscous flow due to the limitations of boundary drag. To the seismic processor or interpreter, a weld is seismically complete when it produces only a single reflection on seismic data, even though a single reflection may actually represent several tens of meters of evaporites. To the structural geologist, a complete weld is one that results in overburden deformation, such as the initiation of inversion to form a turtle structure. To the explorationist, a complete weld is one across which hydrocarbons can migrate (or leak). In these examples, a “complete” weld for the purpose at hand may contain some remnant evaporites and so can be considered a partial weld using the aforementioned thickness criteria. However, there appears to be a direct correlation between remnant evaporite thickness and the degree of completeness in each of these examples. As evaporites thin, they increasingly resist viscous flow (Chapter 1), tend to produce singular reflections on seismic data (Chapter 2), and are more susceptible to cross-weld migration of subsurface fluids (Chapter 3).

In an effort to better understand the processes that form welds and these different perspectives, the primary goals of this dissertation were to:

1) Investigate salt weld formation by quantifying the contribution of viscous flow to salt welding. In Chapter 1, numerical and analytical models based on exact solutions to the Navier-Stokes equations were used to investigate viscous flow for various boundary conditions and flow parameters. This work was inspired by the pioneering numerical models of Cohen and Hardy (1996) and Ings and Shimeld (2006), who modeled salt evacuation but focused on how welding affected stratigraphy and structure in the overburden. More information on the derivation of the model equations can be found in Appendix A. The MATLAB source code used for modeling is included in Appendix B.

2) Characterize the seismic response of welds. Reflection seismology is the primary tool used to identify and characterize welds, but unfortunately much of the internal structure of salt welds is commonly below the resolving power of the data. Thus, characterizing salt welds is closely related to the problem of resolving a thin bed (e.g., Ricker, 1953; Widess, 1973; Kallweit and Wood, 1982). In Chapter 2, one-dimensional and two-dimensional synthetic seismograms constrain the seismic response of welds containing remnant halite or anhydrite

that are thinner than ~50 m and thus below seismic resolution to provide guidelines for interpretation. The source code used to generate synthetics for this purpose is in Appendix C and Appendix D.

3) Investigate the potential effects of fluid flow near and through salt welds, especially the role of dissolution in welding. In Chapter 3, concepts of fluid flow near and through salt are combined with the advanced understanding of welding provided in Chapter 1 and Chapter 2 to characterize fluid flow through salt welds. Furthermore, three-dimensional seismic mapping and well data yield an empirical relationship between weld geometry (e.g. weld area, remnant evaporite thickness) and the capacity of welds to seal hydrocarbons. This work was inspired by recent advances in understanding fluid flow near and through salt (e.g., Schoenherr et al., 2007) and builds on concepts of weld permeability proposed by Rowan (2004).

## CHAPTER 1: VISCOUS FLOW DURING SALT WELDING

### ABSTRACT

Salt may be partially removed by viscous flow from between wall rocks to form a *partial salt weld*. Welds in autochthonous and allochthonous salt can form significant structures in evaporite basins, where petroleum and mineral discovery may hinge on whether salt welds act as seals or windows for migrating hydrocarbons or dissolved metals. Little is known about salt evacuation during welding. I address this topic using analytical and numerical models, based on exact solutions to the Navier-Stokes equations for idealized geometries and boundary conditions, to explore the evolution of salt thickness through time during evacuation and establish how thin salt can become by viscous flow alone. Differential loading can drive salt flow, which is rate-limited by drag along the boundaries of a salt layer. Where salt flow is restricted, for example beneath a broad prograding sediment wedge, up to ~50 m salt can remain in a partial weld. Where salt flow is unrestricted, for example beneath a subsiding minibasin, viscous flow can remove all but a vanishingly thin ( $\ll 1$  m) salt layer. In both cases, any remaining salt must be removed by dissolution or faulting. Evacuation rate increases with increasing differential stress and decreasing flow length and salt viscosity, which is controlled by lithology, water content, and grain size. Layer-parallel wall rock translation may result in a fault weld but may also inhibit

evacuation if the displacement counteracts flow driven by a hydraulic gradient. Evacuation of multilayered evaporites depends on the distribution of layer thickness and viscosity, and multilayered evaporites can be compositionally modified during evacuation.

## INTRODUCTION

Salt, used here to describe any rock composed primarily of halite, may creep as a viscous fluid. Salt creep occurs under a wide range of geologic conditions (Hudec and Jackson, 2007) and tens to hundreds of kilometers of extension or shortening can detach on sheared salt layers (e.g., Laubscher, 1961; Duval et al., 1992; Brun and Fort, 2004; Dooley et al., 2009). Over time, an initially tabular salt deposit may evolve into an enormous variety of diapirs, canopies and other salt structures. As salt flows into these structures, the source layer may thin to form partial weld. Here, a *partial salt weld* describes a body of salt that has thinned to less than ~50 m but still contains remnant salt. In contrast, a *complete weld* contains no remnant salt and is merely a contact surface between rocks that were formerly separated by salt.

Though *salt welds* were first formally named and classified by Jackson and Cramez (1989), the idea of vanished salt had been known for some time (e.g., Trusheim, 1960) and welds themselves had been known by other names, such as “evacuation surface” or “cicatrice salifère” (literally, salt scar) (Burolet, 1975).

Jackson and Cramez (1989) defined a salt weld as a discordant surface resulting from the complete evacuation of salt (here, a complete weld) and they recognized a wide variety of welds based on origin, style, and structural setting. I expand their definition to include both *partial welds*, those that contain less than ~50 m of remnant salt, and *complete welds*, those that contain no salt. Among many geologic examples, Schuster (1995) characterized shallowly detached salt welds in onshore and offshore Louisiana, and Rowan et al. (1999) classified salt welds based on their geometry and regional context. Numerical simulations of salt flow (e.g., Cohen and Hardy, 1996; Schultz-Ela and Jackson, 1996; Ings and Shimeld, 2006; Massimi et al., 2007) have successfully modeled salt-sediment interaction, but focus on the development of structure and stratigraphy in the overburden and not on the evolution of the associated welds. To compound the difficulty of understanding welding, field exposures are typically of mediocre quality because of near-surface dissolution (e.g., Giles and Lawton, 1999; Willis et al., 2001; Dyson and Rowan, 2005). Subsurface welds are imaged by seismic data, but the temporal resolution of many reflection seismic surveys is too coarse (greater than ~30-50 m of halite for peak frequencies of ~10-30 Hz) to display the internal structure of welds. Furthermore, seismic data and well information related to welds are sparse and commonly proprietary.

The geology near salt welds is internally complex and individual welds can be traced for 10 km or more across evaporite basins (Figure 1.1). A large

proportion of a source layer may be removed because of lateral salt expulsion during regional extension, loading by overburden, and downdip flow. Salt structures vary from subhorizontal primary welds formed by lateral salt expulsion (e.g., Buroillet, 1975; Jackson and Cramez, 1989; Duval et al., 1992; Mohriak et al., 1995; Ge et al., 1997; Hall, 2002) to steep secondary welds formed during shortening (e.g., Giles and Lawton, 1999; Rowan et al., 1999; Brun and Fort, 2004; Gottschalk et al., 2004; Dooley et al., 2009). Allochthonous salt sheets and canopies can also be evacuated to form welds, which can be stacked high in the stratigraphic succession (e.g., Diegel et al., 1995; Schuster, 1995). As salt evacuates to form a weld, these movements are recorded in the variable thickness, dispersal patterns, and facies distributions of overlying sediments (e.g., Rowan and Weimer, 1998; Hudec et al., 2009). Furthermore, the formation of a salt weld can affect the growth of associated salt structures as they are cut off from the source layer (e.g., Buroillet, 1975; Vendeville and Jackson, 1992b; Hudec et al., 2009). Salt layers are particularly well-suited as a décollement because of their low strength (Davis and Engelder, 1985), but evacuation may increasingly induce strain into surrounding rocks, as thinned salt forms a less effective detachment than thick salt (Vendeville et al., 1993; Cotton and Koyi, 2000).

Figure 1.1: Examples of salt welds. Cross sections at two different scales reflect the widely variable sizes of salt welds. Time-domain cross sections are converted to depth using an appropriate uniform seismic velocity for each example. All the cross sections have no vertical exaggeration. (a) Primary weld produced by seaward expulsion of Aptian salt, Santos Basin, Cabo Frio, deepwater Brazil (after Mohriak et al., 1995). (b) Primary weld associated with raft tectonics (extreme extension) over Aptian salt, Lower Congo Basin, Cabinda shelf (after Chimney and Kluth, 2002). (c) Secondary weld produced by lateral shortening of a diapir of Aptian salt at the updip end of an ultra-deepwater thrust belt, Lower Congo Basin (after Jackson et al., 2008). (d) Tertiary weld produced by Jurassic salt expulsion in a stepped counterregional allochthonous sheet, deepwater Louisiana, Gulf of Mexico (after Schuster, 1995). (e) Tertiary welds produced by orogenic shortening of Carboniferous diapiric walls rising from a mid-Cretaceous salt canopy, Sverdrup Basin, Axel Heiberg Island, Nunavut, Arctic Canada (after Harrison and Jackson, 2008).



Predicting which welds are prone to leak or seal hydrocarbons is essential in exploration programs in many hydrocarbon-bearing basins affected by salt tectonics. In many cases, hydrocarbons sourced in subsalt source rocks must migrate through salt windows, permeable areas of thin or vanished salt, in order to become entrapped in suprasalt reservoirs (McBride et al., 1998; Guardado et al., 2000; Rowan, 2005). Recent discoveries in the Gulf of Mexico such as Marco Polo, Holstein, and Auger all relied on cross-weld hydrocarbon migration. Alternatively, a potential subsalt reservoir may require an adjacent salt weld to seal. For example, recent exploration targets below allochthonous salt in the Gulf of Mexico (e.g., Kaskida, Keathley Canyon Block 292/291) and below autochthonous salt in the Campos and Santos Basins of offshore Brazil (e.g., Wahoo discovery, Block BM-C-30) have relied on nearby welds to seal. In many cases, seal continuity and integrity depend on remnant salt thickness, so understanding how salt thins during welding is crucial to exploration success.

Two main processes create salt welds: 1) viscous flow and 2) dissolution. The role of dissolution during salt welding is controlled by the permeability of the host rocks and the flux, hydrodynamics, and composition of subsurface waters (Lohmann, 1972; Anderson and Kirkland, 1980; Ge and Jackson, 1998). Salt can be dissolved from the top, base, and sides, or from porous interbeds (Cartwright et al., 2001). Understanding salt dissolution near the surface has been motivated by questions of hydrologic stability of repositories planned for high-level nuclear

waste and mine stability (e.g., Bosworth, 1981; Dix and Jackson, 1982; Chaturvedi, 1986; Alkattan et al., 1997a; 1997b). Modeling the contribution of dissolution to salt welding is addressed in Chapter 3.

Here, I focus on how viscous flow causes salt to thin using analytical and numerical models based on exact steady-state solutions to the Navier-Stokes equations for hydraulic-gradient or displacement boundary conditions (Figure 1.2). Exact solutions are used here because they are uniformly valid (Wang, 1991) and are easily tested for sensitivity to input parameters (e.g., Cohen and Hardy, 1996). The models (1) track the evolution of salt thickness during evacuation, (2) establish limits on the removal of salt for idealized structural geometries, and (3) determine the sensitivities of remnant evaporite thickness to geometry, viscosity, and other variables.

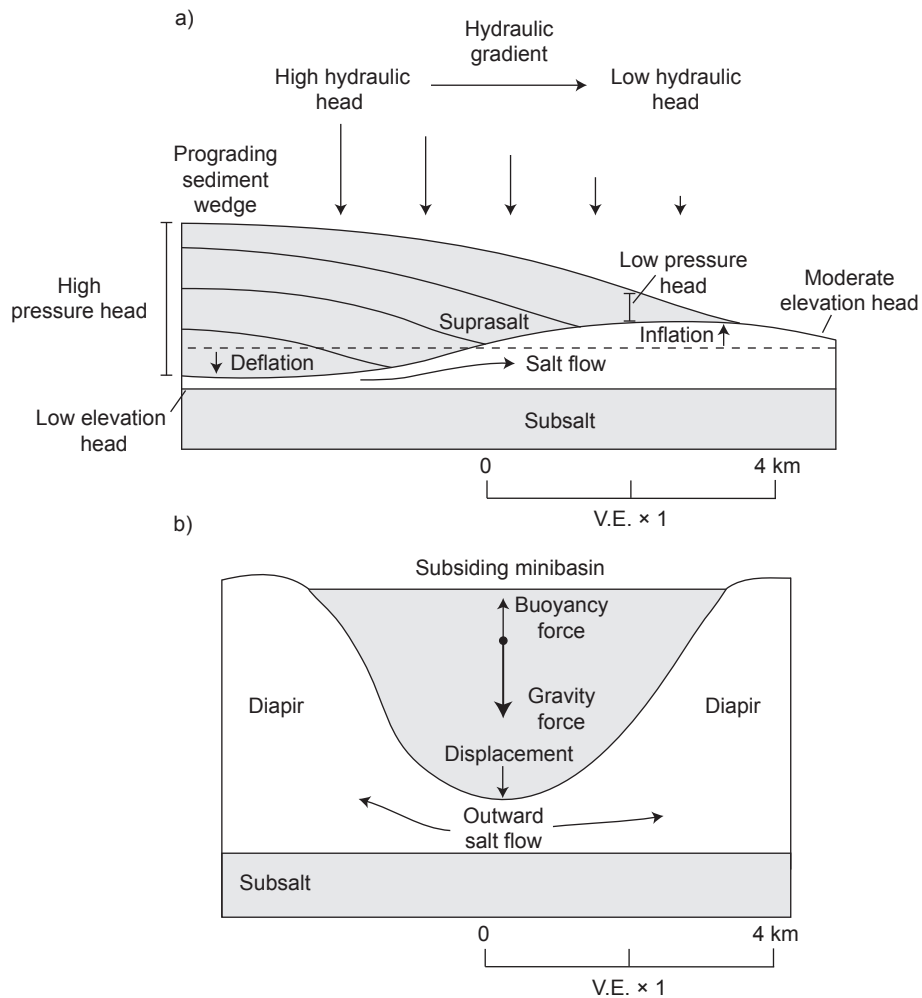


Figure 1.2: Schematic diagram depicting (a) hydraulic-gradient boundary conditions and (b) displacement boundary conditions. In (a), the differential load imposed by a prograding sediment wedges establishes a hydraulic gradient, causing salt to flow from high hydraulic head to low hydraulic head. The suprasalt section subsides to fill space as salt is expelled. The dashed line shows the top of salt prior to sedimentary loading. In (b), a minibasin subsides into salt expelling salt from beneath it into neighboring diapirs.

There are a large number of possible geometries, input parameters, and boundary conditions that might affect salt flow. Here, the effects of three prototypes are investigated: (1) thinning of a single salt layer, (2) thinning of a single salt layer with layer-parallel wall rock translation, and (3) thinning of a multilayered evaporite sequence. To obtain the equations of motion used to model these prototypes, I first review the physical processes involved in salt flow. All models presented here assume salt evacuation into adjacent structures is uninhibited and thus represent best-case scenarios for salt evacuation and weld formation.

## **Viscous Flow**

Salt creep has been intensively studied since it was first observed in mine walls (e.g., Dobrin, 1941). Laboratory experiments on dry halite at elevated temperatures, strain rates and differential stresses indicate that salt behaves as a non-Newtonian fluid and etch pit and X-ray topography analyses indicate solid state flow of dry salt occurs due to dislocation creep (e.g., Carter and Heard, 1970; Carter and Hansen, 1983; Hunsche and Hampel, 1999). The shape and surface slope of emergent salt diapir tops and glaciers in Iran (e.g., Wenkert, 1979; Talbot and Jarvis, 1984; Talbot et al., 2000; Talbot and Aftabi, 2004; Bruthans et al., 2006; Weinberger et al., 2006) have produced estimates of effective salt viscosity. However, the exponent in the flow law for salt creep has

been much harder to determine.

Talbot and Rogers (1980) observed a marked increase in mobility of salt glaciers in Iran after rainfalls, inspiring experiments that quantified the importance of diffusion and solution-precipitation processes in salt. Urai et al., (1986) found that salt with as little as 0.05 weight percent water promotes solution-precipitation creep at low differential stresses. Fluid-assisted dynamic recrystallization in salt by grain boundary migration reduces stored strain energy and allows dislocation mechanisms to proceed unimpeded (Peach et al., 2001; Ter Heege, 2005a), further enhancing creep.

Natural salt deformation is dominated by diffusion processes at low differential stresses, low strain rates, and in fine-grained salt (e.g., in the mylonitized distal parts of salt glaciers, Talbot, 1979). In contrast, dislocation processes dominate creep at high differential stresses, high strain rates, and in coarse-grained salt (van Keken et al., 1993). Salt deformation has been modeled using Newtonian silicone polymers in numerous sandbox experiments (e.g., Vendeville and Jackson, 1992a; b; Dooley et al., 2009) and numerical models have simulated both Newtonian (Ings and Shimeld, 2006) and non-Newtonian (Massimi et al., 2007) flow. Here, salt will be modeled as a Newtonian fluid with stress exponent equal to unity. In non-Newtonian fluids, those with a stress exponent greater than unity, viscosity decreases with increasing strain rate. This behavior is known as shear thinning and may enhance evacuation, but the extent

to which shear thinning occurs during natural salt deformation is unknown.

The dynamic viscosity of natural rock salt can be inferred from laboratory experiments and field observations. Creep laws from rock-mechanics experiments indicate that viscosity depends primarily on 1) crystal grain size, 2) differential stress, and 3) temperature (van Keken et al., 1993). Estimates of viscosity based on flow laws for combined dislocation, diffusion, and solution-precipitation creep generally range from  $10^{12}$  Pa•s (calculated as a minimum from Figure 7 in Ter Heege et al., 2005b) to  $10^{20}$  Pa•s (van Keken et al., 1993). Estimates of viscosity based on field observations vary widely from one salt basin to another (e.g., Odé, 1968; Talbot and Jarvis, 1984) and even between structures in a single basin (Weinberger et al., 2006), but generally range from  $10^{17}$  Pa•s to  $10^{21}$  Pa•s. Experimental and field estimates of viscosity differ because the scales of length and time vary, and because anhydrite or carbonate impurities increase the viscosity of rock salt (Price, 1982; Jordan, 1987).

Numerical and analogue models of salt tectonics have typically used specific values for dynamic viscosity because dynamic similarity is achieved using any viscosity as long as flow is laminar (Weijermars et al., 1993). Here, constant viscosity values are used to investigate viscous behavior (e.g., Cohen and Hardy, 1996).

## HYDRAULIC-GRADIENT BOUNDARY CONDITIONS

Like all fluids, salt can flow in response to a hydraulic-head gradient (hereafter, hydraulic gradient), which is the sum of a pressure-head gradient and an elevation-head gradient (Kehle, 1988; Hudec and Jackson, 2007). As salt flows from points of high head to low head, the salt layer can locally thin to form a partial weld. The evacuated salt flows into salt-cored structures, such as salt diapirs. Hydraulic-gradient boundary conditions are well suited to describe the effects of gravitational loading, which has long been recognized to drive salt flow (e.g., Arrhenius, 1913; Trusheim, 1960; Worrall and Snelson, 1989; Hudec and Jackson, 2007).

Salt evacuation due to gravitational loading was numerically simulated by Cohen and Hardy (1996) using a formula for fluid flow between parallel plates derived by Mandl (1988) as an exact solution of the Navier-Stokes equations by specifying hydraulic-gradient boundary conditions. The following derivation is by no means exhaustive (for a more complete derivation, see Bruus, 2008) but presents the fundamentals and critical assumptions of modeling salt as a Newtonian viscous fluid. The derivation begins with the Navier-Stokes equations for an incompressible Newtonian fluid (Equation 1.1), including pressure gradient ( $P$ ), gravitational acceleration ( $g$ ), constant salt density ( $\rho_s$ ), constant dynamic viscosity ( $\mu$ ), and the velocity field ( $V$ ).

$$\rho_s \frac{DV}{Dt} = -\rho_s g - \nabla P + \mu \nabla^2 V \quad (1.1)$$

A simplified formula describes rectilinear flow between two smooth, parallel plates of infinite extent. One coordinate axis, the  $x$ -axis, is taken parallel to the flow direction and the other axes are orthogonal (Figure 1.3). Flow is defined to be quasi-unidirectional, so the Navier-Stokes equations are one-dimensional (Equation 1.2).

$$\rho_s \frac{Du}{Dt} = -\rho_s g_x - \frac{dP}{dx} + \mu \frac{d^2 u}{dx^2} \quad (1.2)$$

In nature, salt does not flow between smooth, parallel plates of infinite extent. However, as salt thickness becomes much smaller than the lateral extent of the flow, the parallel plate approximation becomes valid. In addition, natural salt contacts are rarely perfectly smooth. On seismic data, welds commonly appear smooth (e.g., Gottschalk et al., 2004; Roberts et al., 2004; Dutton and Trudgill, 2009), but at small scales must have numerous irregularities (e.g., Giles and Lawton, 1999; Willis et al., 2001). Irregularities such as basement steps (e.g., Jackson et al., 1994; Diegel et al., 1995) or inclusions such as igneous sills (e.g., Kent, 1979; Hafid et al., 2006) tend to increase boundary drag and slow overall evacuation. Below a sinking indenter along the top of the salt, evacuation may be locally accelerated. However, these effects are not addressed here.

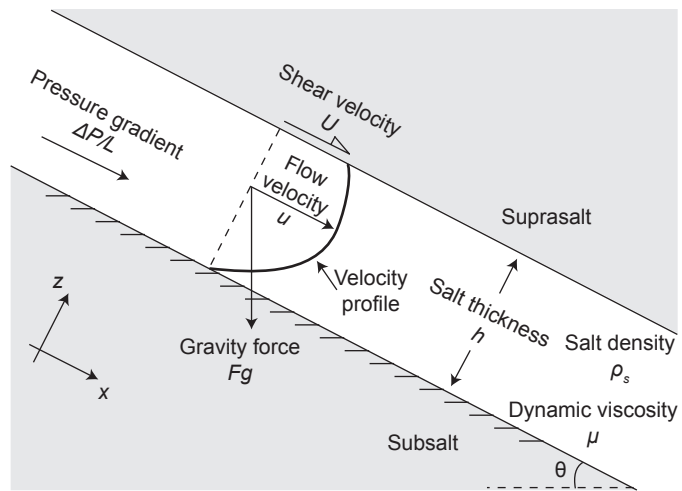


Figure 1.3: Coordinate system and model used to reduce the Navier-Stokes equations to one-dimensional flow between two smooth, parallel plates of infinite extent. The  $x$ -axis is parallel to the salt flow direction.  $U$  is the shear velocity of the upper boundary,  $u$  is the salt flow velocity,  $h$  is the thickness of the salt layer,  $F_g$  is the gravitational body force acting on the salt,  $\Delta P/L$  is the pressure-head gradient driving salt flow,  $\mu$  is the viscosity of the salt, and  $\theta$  is dip of the salt layer.

This analysis is only valid for laminar flow, which is characteristic of rock salt creep (Ramberg, 1993). In turbulent flow, inertial forces create eddies and vortices that cause rapid changes in velocity and pressure terms. Whether flow is laminar or turbulent can be estimated by calculating the dimensionless Reynolds number (Equation 1.3), the ratio of inertial to viscous forces, expressed as the product of fluid density, the characteristic length scale (the distance between the two plates,  $h$ ), fluid velocity ( $u$ ), and the inverse of dynamic viscosity.

$$\text{Re} = \frac{\rho_s u h}{\mu} \quad (1.3)$$

For salt flowing under typical geologic conditions, the Reynolds number is more than twenty orders of magnitude smaller than unity (Figure 1.4), such that inertial forces are negligible compared with the viscous forces. Thus salt flow is fully laminar (Ramberg, 1981) and inertial accelerations can be ignored (Equation 1.4).

$$\mu \frac{d^2 u}{dx^2} = \rho_s g_x + \frac{dP}{dx} \quad (1.4)$$

Laminar flow in deforming salt can produce complex flow folds and shear zones even from small variations in non-uniform (non-parallel streamlines) or unsteady (varying over time) flow (e.g., Talbot and Aftabi, 2004).

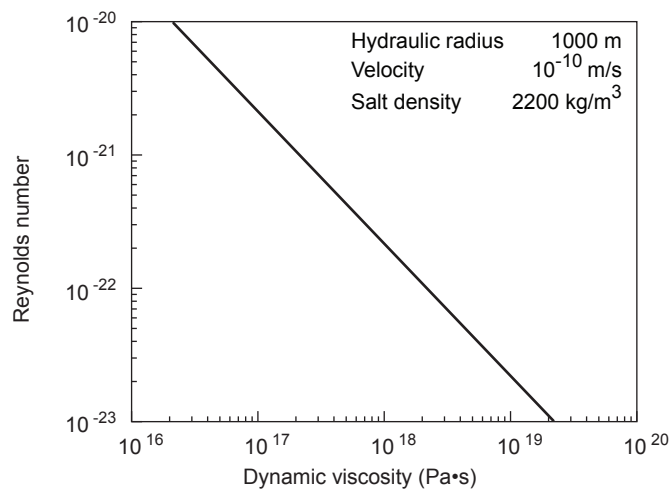


Figure 1.4: Reynolds number during salt flow. Reynolds number was calculated using Equation 1.3 with a salt density of  $2200 \text{ kg/m}^3$ , hydraulic radius of 1000 m, and a generous flow velocity of  $10^{-10} \text{ m/s}$ . Seni and Jackson (1983) estimated a Reynolds number of  $10^{-25}$  for Haynesville Dome, East Texas. The theoretical boundary between laminar and turbulent flow occurs at Reynolds number near unity.

At this point, it is convenient to combine pressure-head gradient (i.e., the right term in Equation 1.4) and elevation-head gradient (the central term in Equation 1.4) into a single hydraulic gradient. Hydraulic gradient can be viewed as the ratio between flow stress and flow length. Paleopiezometry using subgrain sizes (e.g., Guillopé and Poirier, 1979; Carter et al., 1983; 1993; Ter Heege et al., 2005a; Schoenherr et al., 2007) indicates differential stresses in naturally deformed rock salt cores are generally less than 10 MPa (7.3 MPa in Weinberger et al., 2006; 5.6 MPa in Ter Heege et al., 2005b) during flow and may be as low as 1 to 2 MPa (Carter et al., 1993; Schoenherr et al., 2007). For simplicity, a constant hydraulic gradient ( $\Delta P'/L$ ) will be used here.

Integrating twice with respect to flow depth ( $z$ ) results in a general expression for the flow velocity ( $u$ ) (Equation 1.5). The constants of integration depend on boundary conditions. Both no-slip (Poiseuille flow) and layer-parallel translation of the upper plate (Couette flow) boundary conditions are relevant to nature. If weld formation is accompanied by layer-parallel wall rock translation, the resulting weld is referred to as a *fault weld* (Figure 1.5) (Hossack and McGuinness, 1990).

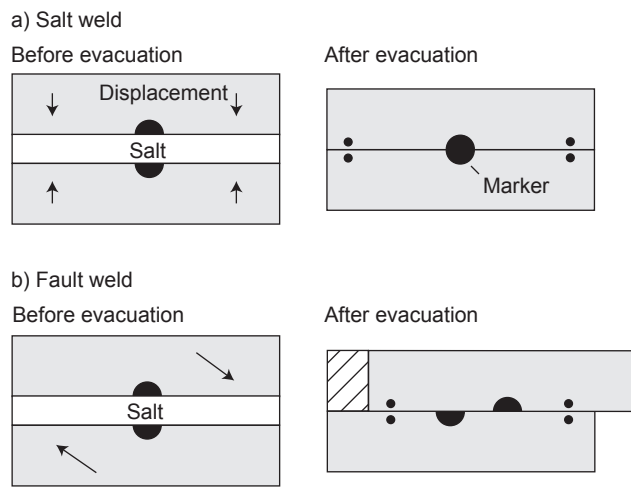


Figure 1.5: Schematic diagrams highlighting the distinction between a complete salt weld (a) and a complete fault weld (b). A salt weld forms if the salt boundaries are not displaced with respect to each other during evacuation. A fault weld forms if shear displacement occurs. Concepts and terminology after Jackson and Cramez (1989) and Hossack and McGuinness (1990).

Solving for the constant term then the linear term, flow velocity between parallel plates can be expressed in terms of flow depth, distance between the plates, shear velocity of the upper salt boundary ( $U$ ), hydraulic gradient, and dynamic viscosity (Equation 1.6). Integrating over the distance between the plates yields a general formula for flux per unit width (Equation 1.7).

$$\mu u = \frac{z^2}{2} \left( \frac{\Delta P'}{L} \right) + Ay + B \quad (1.5)$$

$$u = \frac{Uz}{h} + \frac{z^2 - hz}{2\mu} \left( \frac{\Delta P'}{L} \right) \quad (1.6)$$

$$q = \frac{Uh}{2} - \frac{h^3}{12\mu} \left( \frac{\Delta P'}{L} \right) \quad (1.7)$$

Conserving volume, flux can be rewritten to obtain an equation describing the rate of change of the distance between the plates ( $\dot{h}$ ) and the flux divided by the flow length (Equation 1.8). This introduces a time-dependent acceleration of flow that can be ignored at the very low Reynolds numbers appropriate here.

$$\dot{h} = \left[ \frac{Uh}{2} - \frac{h^3}{12\mu} \left( \frac{\Delta P'}{L} \right) \right] \frac{1}{L} \quad (1.8)$$

If the shear velocity of the upper plate is equal to zero, Equation 1.8 is a separable initial value problem where the thickness at time ( $t = 0$ ) equals the

initial salt thickness ( $h_0$ ). The solution describes the thickness of salt through time due to hydraulic-gradient boundary conditions (Equation 1.9). If the upper plate is translating, Equation 1.8 may be numerically approximated using forward-difference techniques (Equation 1.10).

$$h = \left[ \frac{1}{h_0^2} - \frac{t\Delta P'}{6\mu L^2} \right]^{-1/2} \quad (1.9)$$

$$h_{k+1} = h_k - \left[ \frac{Uh_k}{2} - \frac{h_k^3}{12\mu} \left( \frac{\Delta P'}{L} \right) \right] \frac{t}{L} \quad (1.10)$$

Many minibasins above salt are circular or elliptical in plan view (Diegel et al., 1995; Pratson and Haxby, 1996; Steffen et al., 2003; Hudec et al., 2009). An equivalent differential equation can be obtained for radially outward flow between two parallel circular plates (Equation 1.11) for a flow zone defined by an inner radius ( $r_1$ ) and outer radius ( $r_2$ ); see Jackson and Simmons (1966) for a more complete derivation.

$$h = \left[ \frac{1}{h_0^2} - \frac{t\Delta P'}{6\mu r^2 \ln(r_2/r_1)} \right]^{-1/2} \quad (1.11)$$

The natural logarithm in Equation 1.11 distinguishes radial flow from rectilinear flow. To avoid singularity as the inner radius tends to zero, a finite area near the center of the plates must have a constant, uniform pressure. It is convenient but arbitrary to choose an inner radius such that  $r_2/r_1$  is  $e$ , eliminating the natural logarithm entirely. In nature, the shape of the overburden determines the inner and outer radii, but for  $5 \times 10^{-5} < r_2/r_1 < 0.9$ , eliminating the natural logarithm term will incur no more than one order of magnitude error. For a flat-bottomed overburden subsiding into salt ( $r_2/r_1 \sim 1$ ), flow is more vigorous than for rounded overburden, ( $r_2/r_1 \ll 1$ ).

#### **DISPLACEMENT BOUNDARY CONDITIONS**

Salt flow can also be driven by tectonically induced lateral extension (e.g., Jackson and Talbot, 1986; Duval et al., 1992; Jackson and Vendeville, 1992a, b; Brun and Mauduit, 2008) or shortening (e.g., Cobbold et al., 1995; Sherkati et al., 2006; Jackson et al., 2008). Apart from the spectacular effects of lateral tectonic stresses, there are more subtle types of loading of salt. For example, the body force of gravity can pull a minibasin downward, which displaces salt from beneath it when the average bulk density of the sediments is greater than the density of the fluid salt. In these examples, it is appropriate to specify displacement boundary conditions to determine appropriate solutions to the Navier-Stokes equations.

Consider a hemispherical minibasin subsiding into thick salt above a rigid floor. The motion of an object traveling through a viscous fluid is opposed by a drag force proportional to settling velocity and to the dynamic viscosity of the fluid. Neglecting skin friction, the drag force ( $F_D$ ) acting on a sinking minibasin at some distance far from the base of salt is defined by Stokes' Law (Equation 1.12).

$$F_D = 6\pi\mu r\dot{h} \quad (1.12)$$

As the minibasin sinks nearer the lower boundary, displacement of intervening salt is progressively resisted by boundary drag, which in turn increasingly resists fall of the minibasin. When the salt is sufficiently thin, Stokes' Law can be multiplied by a correction factor (Equation 1.13) to reflect an ever-increasing drag force (Cox and Brenner, 1967). Strictly speaking, these forces were derived for a sinking sphere around which the streamlines eventually reattach at the crest of the sphere. For a sinking minibasin, flow does not reattach, which increases the drag force, but this consideration will not be addressed here.

$$F_D = 6\pi\mu r\dot{h} \times \frac{r}{h} \quad (1.13)$$

Now imagine a flat-bottomed minibasin approaching a rigid flat floor. By specifying the velocity of convergence in the Navier-Stokes equations, Gnoevoi et al. (1996) derived an equivalent expression for the resistive force in a viscous fluid displaced between two approaching parallel, circular plates (Equation 1.14). This drag force is inversely proportional to the cube of salt thickness and again inhibits salt expulsion.

$$F_D = \frac{3\pi\mu r^4 \dot{h}}{2h^3} \quad (1.14)$$

These drag forces are not the only ideal examples, but they provide a range of geometries tractable for modeling. Intermediate and more extreme resistive forces lack such convenient closed forms and are outside the scope of this modeling. Force balance can be used to derive equations of motion due to displacement boundary conditions, for example, a subsiding minibasin. Though several mechanisms may initiate subsidence of a minibasin into salt (Hudec et al., 2009), most minibasins thicker than 2-4 km subside because of negative buoyancy after compaction increases the average bulk density of the sediments they contain above that of salt (Hudec et al., 2009). Sinking by negative buoyancy is the only mechanism considered here. The forces acting on a sinking minibasin are gravity, buoyancy, and drag. If salt flow is relatively unrestricted, as beneath a hemispherical minibasin, the expression of Cox and Brenner (1967)

yields the drag force, and the acceleration of the sinking minibasin can be written as a nonlinear differential equation in terms of the average bulk density of the overburden ( $\rho_o$ ), minibasin radius, initial salt thickness, evolving salt thickness, and salt density (Equation 1.15). Conversely, if salt flow is restricted, as in a flat-bottomed minibasin, the expression of Gnoevoi et al. (1996) can be used and an alternative equation of motion is obtained given some initial overburden thickness ( $s$ ) (Equation 1.16).

$$\ddot{h} = \frac{(\rho_o - \rho_s)g}{\rho_o} - \frac{9\mu\dot{h}}{r^2 h \rho_o} \quad (1.15)$$

$$\ddot{h} = \frac{(\rho_o - \rho_s)g}{\rho_o} - \frac{3\mu r^2 \dot{h}}{2s \rho_o h^3} \quad (1.16)$$

For more rigorous modeling, thickening and compaction of the overburden can be incorporated into the equations of motion (Equation 1.17 for a hemispherical minibasin and Equation 1.18 for a flat-bottomed minibasin) given some compaction function ( $\rho(s)$ ) (e.g., see Equation 18 in Hudec et al., 2009).

$$\ddot{h} = \frac{(\rho(s) - \rho_s)g}{\rho(s)} - \frac{6\pi\mu r \dot{h}}{\left[\frac{2}{3}\pi r^3 + \pi r^2(h_0 - h)\right]\rho(s)} \left(\frac{r}{h}\right) \quad (1.17)$$

$$\ddot{h} = \frac{(\rho(s) - \rho_s)g}{\rho(s)} - \frac{3\pi\mu r^4 \dot{h}}{2(\pi r^2[s + (h_0 - h)])\rho(s)h^3} \quad (1.18)$$

These equations may be solved numerically to model thinning of salt by specifying initial salt thickness and initial boundary velocity. Velocity and acceleration terms change continuously but are insignificant compared with the long geologic time for salt evacuation. This makes the differential equations stiff, so a solver must be chosen carefully. The built-in MATLAB solver, ode15s, a variable-order method based on numerical differentiation formulas, was effective.

### **THINNING OF A SINGLE SALT LAYER**

Viscous evacuation of a single salt layer was modeled using the derived equations of motion. Schematic diagrams illustrating the model setups are included in Figure 1.6. The results of this modeling show that where salt flow is restricted between parallel plates, salt thickness tends asymptotically toward zero as time tends to infinity (Figure 1.7a). At time scales appropriate to salt tectonics, say up to several tens of millions of years, remnant salt thickness will be finite and evacuation incomplete, forming a *partial weld* containing up to ~50 m of salt (Figure 1.7b). When salt has thinned to less than ~50 m, viscous flow may be strongly resisted by boundary drag and other processes such as dissolution or shear displacement of wall rocks must act to create a complete weld (Cohen and Hardy, 1996; Davison et al., 1996a; Hudec and Jackson, 2007). This upper limit of remnant salt thickness in a partial weld is approximate and depends largely on the boundary conditions of the flow. Cohen and Hardy (1996) first suggested the

difficulty of complete salt evacuation by flow alone, but the concept that a vanishingly thin fluid provides an infinite resistance to evacuation has been known for some time as the lubrication paradox (Lipscomb and Denn, 1984).

Conversely, where salt flow is laterally unrestricted, such as beneath a subsiding hemispherical minibasin, evacuation is rapid and only a vanishingly thin ( $\ll 1$  m) layer of salt remains (Figure 1.7c). Other indenting geometries, such as angular anhydrite blocks, are also conducive to forming welds that are all but complete by viscous evacuation alone (e.g., Koyi, 2001). Where the weight of the overburden is concentrated at a point (as in the perfectly hemispherical minibasin) or along an edge (as below an angular roof block) above ever-thinning salt, locally elevated differential stresses can also cause grain size reduction or shear thinning, decreasing the effective viscosity of the salt layer and enhancing evacuation.

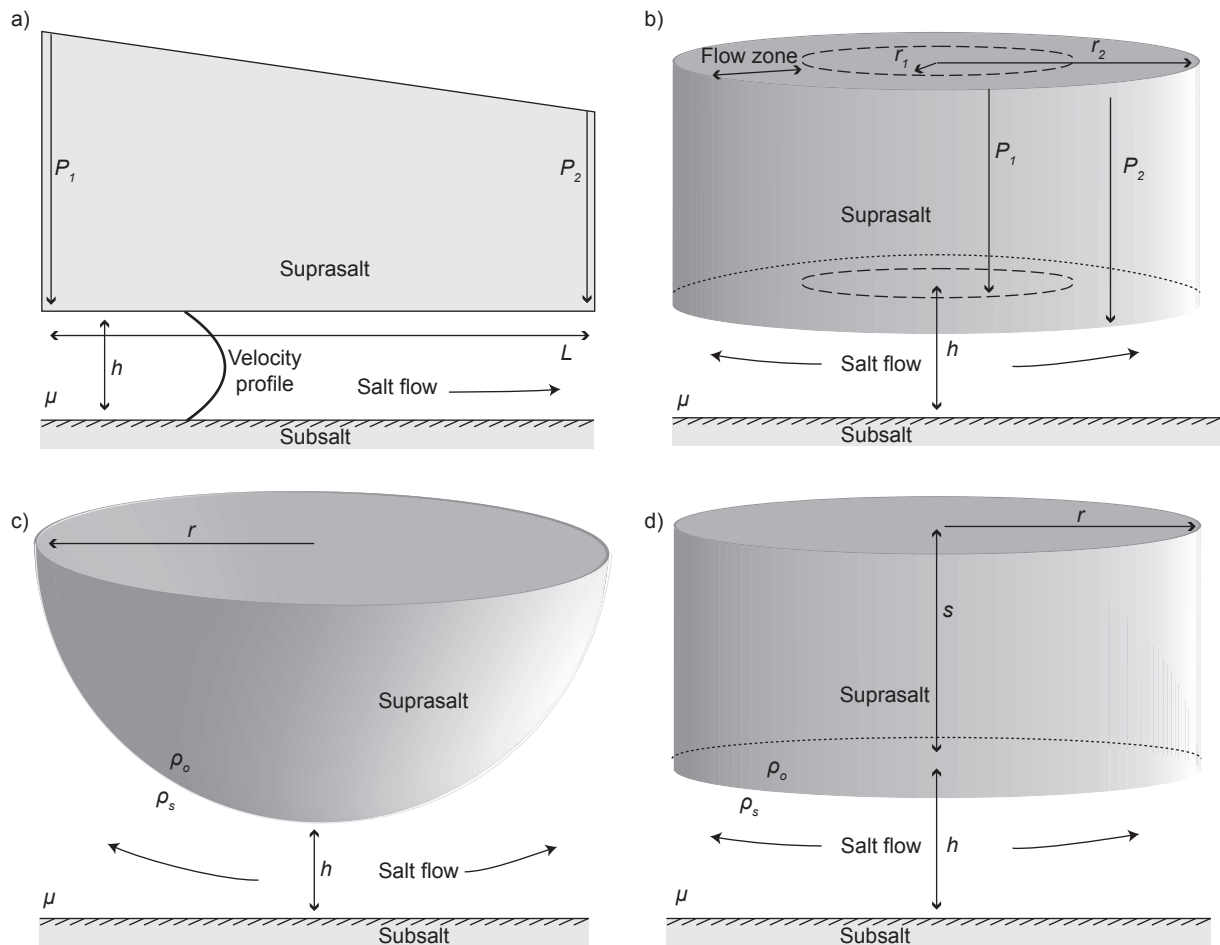
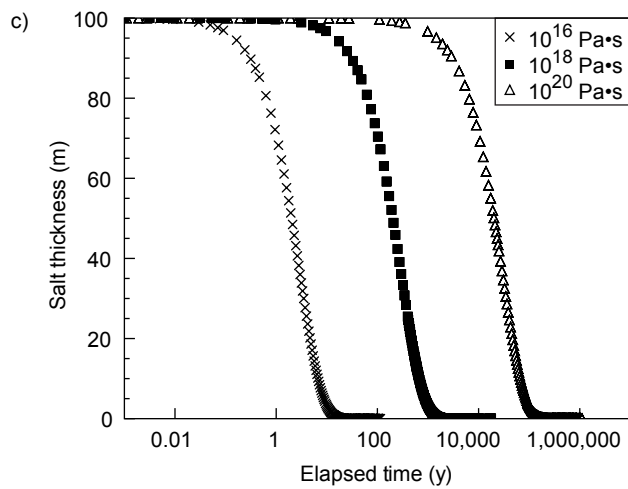
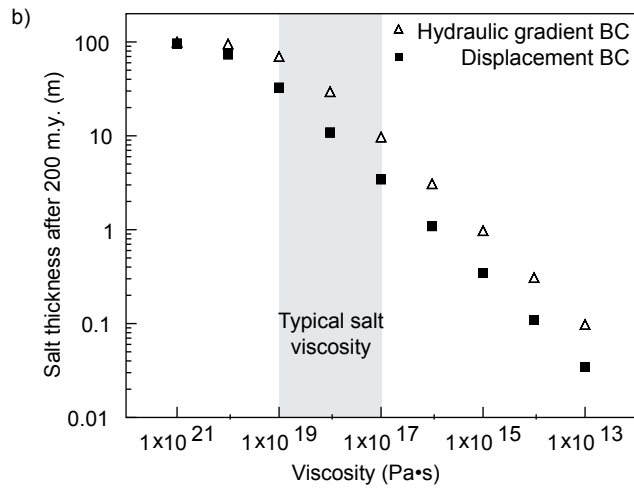
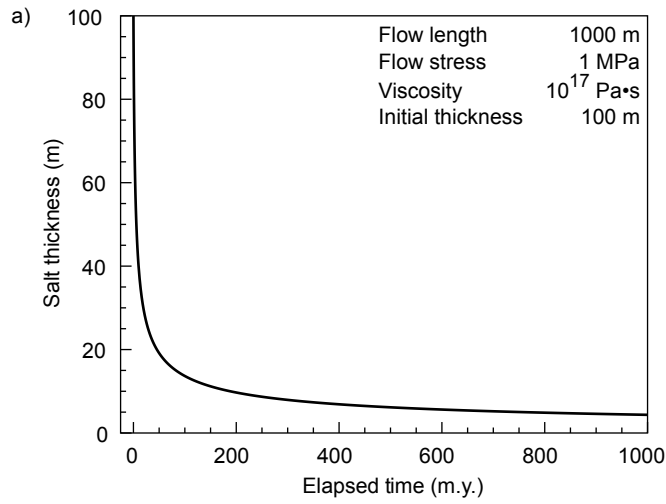


Figure 1.6: Schematic diagram illustrating analytical modeling geometry. For hydraulic-gradient boundary conditions, salt is evacuated in a two-dimensional cross section (a) or from between parallel circular plates (b). In (a), salt flows from a point of high hydraulic head ( $P_1$ ) to a point of low hydraulic head ( $P_2$ ) over a length ( $L$ ). The predicted parabolic velocity profile is indicated. In (b), flow length is the width of the flow zone, the region between some inner radius ( $r_1$ ) and outer radius ( $r_2$ ). For displacement boundary conditions, salt is evacuated from beneath a hemispherical (c) or flat-bottomed (d) minibasin sinking by gravity.

Figure 1.7: a) Evolution of salt thickness calculated using Equation 1.9 and the indicated flow parameters. Evacuation is initially rapid and then slows. The partial weld contains 9.7 meters of salt after 200 m.y. b) Salt thickness after 200 m.y. calculated using Equation 9 and 16 for the flow parameters in (a) and varying viscosity. Parameters used for displacement boundary conditions and restricted salt flow approximate a flow stress of 1 MPa. An increase in viscosity increases residual salt thickness at any given time. Displacement boundary conditions predict a thinner weld than hydraulic-gradient boundary conditions. c) Evolution of salt thickness with displacement boundary conditions and unrestricted salt flow calculated with Equation 1.15 and the flow parameters in (a) and (b). Increasing viscosity delays welding.

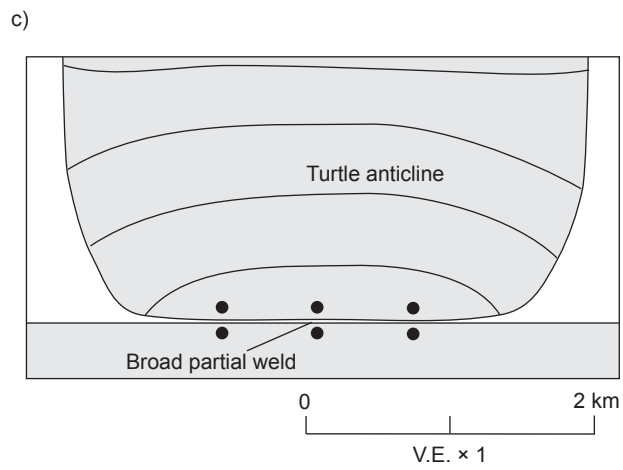
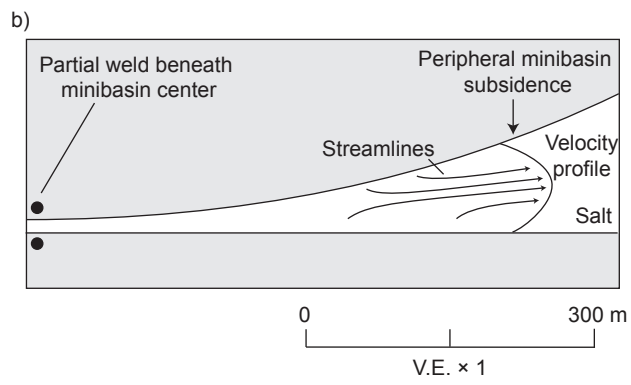
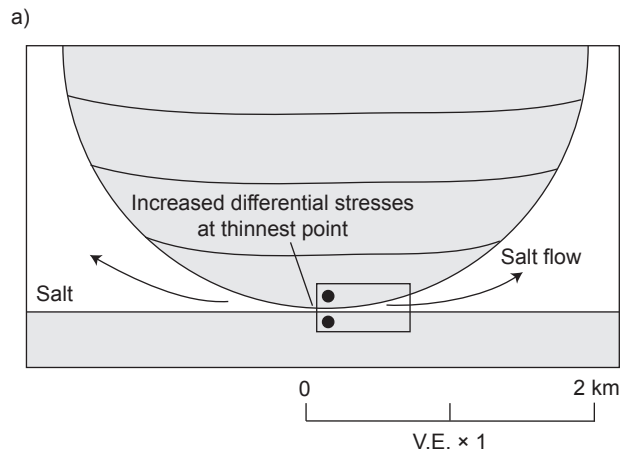


That this numerical modeling predicts partial welds containing up to ~50 m of salt conflicts with human intuition. Consider dropping a marble into a glass of water. It is certainly counter-intuitive to conclude the marble will never contact the bottom of the glass, especially when the marble-on-glass collision is audible. Water beneath the sinking marble increasingly resists its fall as it nears the base of the glass. In so doing, stress is increasingly concentrated into the water until it yields, allowing the marble to come to rest on the glass itself. Why should a subsiding minibasin be any different? Because of the low viscosity of water and the small size of the marble, it takes only a fraction of a second for the marble to decelerate and strike the glass. In contrast, the high viscosity of salt and the large size of minibasins cause minibasin subsidence to occur over several thousands or even millions of years. Elevated differential stresses in the salt caused by stress concentration at the base of the minibasin quicken salt evacuation, but also ultimately lead to deformation within the minibasin.

As salt thins beneath an indenting minibasin, the sediments above the thinnest salt increasingly support the weight of the entire minibasin (Figure 1.8a) until they yield and begin to deform. The flanks of the minibasin continue to subside even as the middle welds out, producing an inversion structure known as a turtle anticline (e.g., Trusheim, 1960; Vendeville and Jackson, 1992b). At this point, salt flow becomes considerably more complex, but can be approximated by flow in a sharp corner between a rotating plane and a horizontal surface

(Figure 1.8b). In this geometry, minibasin flank subsidence is strongly resisted by the presence of salt, and as the corner angle decreases the flow resembles that between parallel plates (Moffatt, 1964). Thus, minibasin deformation during welding does not necessarily produce a thinner weld than for a rigid minibasin, but does provide a mechanism to produce a broader one (Figure 1.8c).

Figure 1.8: a) When salt beneath a non-rigid minibasin thins, the minibasin may deform. b) Salt beneath the center of the minibasin is too thin to continue flowing, but salt beneath the edge of the minibasin will continue to evacuate, allowing the overlying sediments to subside. The wedge of evacuating salt resembles squeezing flow in a corner (Moffatt, 1964), which can be approximated as flow between parallel plates some distance away from the corner. c) The evacuating wedge of salt migrates toward the edge of the diapir, forming a broad partial weld. As the subsidence migrates outward to each edge of the minibasin, sediments in the minibasin are inverted to form a turtle anticline (Trusheim, 1960).



These conclusions also conflict with the many physical models that produce complete welds (e.g., Ge et al., 1997; Brun and Fort, 2004; Dooley et al., 2009). Again, the contradiction results from scaling issues. Physical models of salt tectonics typically have a length scale of about  $10^{-5}$  so even a smear of remnant silicone (the material commonly used to simulate salt) 0.5 mm thick is equivalent to 50 m thickness of salt in nature. Furthermore, remnant silicone in a model weld is absorbed by capillary attraction into the dry sand simulating country rock, as evidenced by a mm-thick rind of silicone-impregnated sand along the silicone contacts. Indeed this mm-scale pushes the limits of scaling. The most common silicone in tectonic modeling is polydimethylsiloxane (PDMS), which has long-chain molecules (Weijermars, 1986). A polymer of ten thousand PDMS monomers is about  $10^{-3}$  mm long (Sok, 1994), equivalent to 0.1 m in nature. Thus at the experimental scales most relevant to the welding process, molecular forces in analogue models violate dynamic similarity to nature. For this reason, the analogy between the smallest structures in physical models, such as welds, and those in nature should not be pushed too far.

For hydraulic-gradient boundary conditions, a decrease in flow length and viscosity or an increase in hydraulic gradient both accelerate evacuation. Thus the thickness of the resulting partial weld can be generalized as the ratio between flow stress and the product of viscosity and flow length squared (Equation 1.19). As this ratio increases, evacuation is faster and the resulting

weld is thinner (Figure 1.9a). The relationship between these parameters is not as obvious when displacement boundary conditions are specified, because the equations of motion are nonlinear. However, increased driving force or decreased viscosity and flow length again promote more vigorous evacuation and a thinner partial weld. Salt evacuation is more vigorous and more salt is removed when thickening and compaction of the overburden are considered (Figure 1.9b).

$$h(t) \propto \frac{\Delta P'}{\mu L^2} \quad (1.19)$$

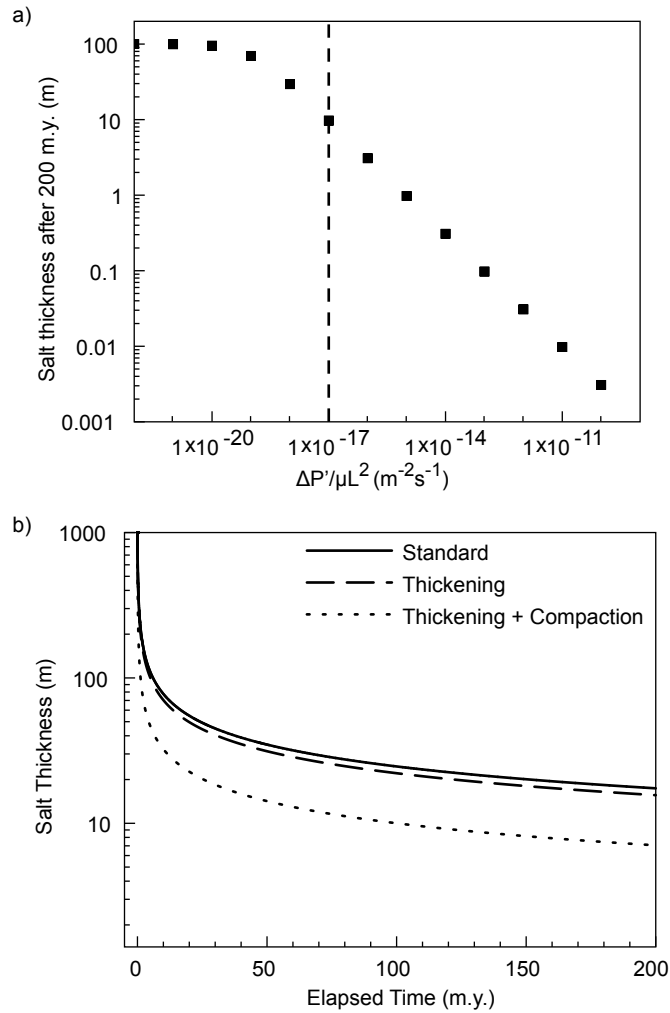


Figure 1.9: a) Salt thickness after 200 m.y. calculated using Equation 1.11 with an initial thickness of 100 m and varying flow parameters. The dashed line is typical for salt flow and was calculated using a flow length of 1000 m, viscosity of 1017 Pa•s, and flow stress of 1 MPa. Increasing viscosity and flow length inhibit flow. Increasing flow stress enhances evacuation. b) Evolution of salt thickness calculated using Equation 1.16 and Equation 1.18 to compare standard displacement loading beneath a subsiding cylindrical minibasin (solid line) with the effects of aggradation (dashed line) and both aggradation and compaction (dotted line). More salt is evacuated if the overburden aggrades and compacts. Calculated with an initial overburden thickness of 1000 m and an initial overburden density of 2210 kg/m<sup>3</sup>.

For similar viscosity, hydraulic gradient, and flow geometries, initial salt thickness has little effect on the thickness of salt remaining in a partial weld. Holding other parameters constant, salt thickness becomes less variable during evacuation (Figure 1.10) because flow rate is proportional to salt thickness; thick salt thins rapidly while thin salt thins slowly. Thus, there is no way to calculate original salt thickness from the thickness remaining in a partial weld. Instead, initial salt thickness is typically estimated using the geometry of synkinematic growth packages in the overburden (e.g., Seni and Jackson, 1983) or structural restorations (e.g., Rowan, 1992; Hossack, 1995).

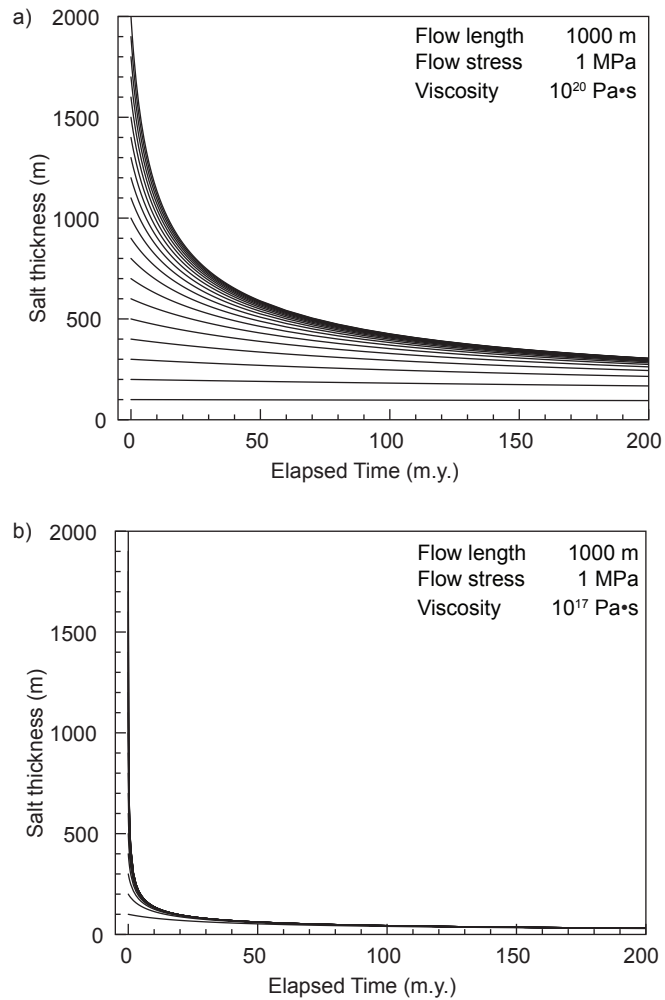


Figure 1.10: a) Evolution of salt thickness calculated using Equation 1.9 for a) high-viscosity salt and b) low-viscosity salt with the indicated flow parameters and a range of initial thicknesses from 100 to 2000 m. After evacuation, it is difficult to determine initial salt thickness from weld thickness, especially if evacuation is vigorous owing to decreased viscosity or increased driving forces.

## **THINNING AND LAYER-PARALLEL WALL ROCK TRANSLATION**

Consider the effects of thinning a horizontal salt layer of uniform thickness whose upper contact is moving. Assuming conservation of salt area in cross section, thinning requires the contacts between salt and its roof or floor to lengthen, as in a stretching fault (Means, 1989). Roof contacts may lengthen by extending or by accreting sediment, perhaps supplied by progradation. If strain in the overburden is homogeneous, thinning salt to the point of welding is problematic (Figure 1.11).

Deformation above salt is typically heterogeneous and overburden extension is commonly accommodated by one or more discrete growth faults that detach into salt (e.g., Buroillet, 1975; Duval et al., 1992; Rouby et al., 2002; Brun and Mauduit, 2008). Growth faults that detach into a mobile substratum comprise two segments 1) an active segment that separates the blocks of sedimentary overburden from one another and 2) an inactive segment that is viscously coupled to the mobile substratum below (Figure 1.12a) (Mauduit and Brun, 1998). As the overburden extends, the inactive segment lengthens and stretches locally and the underlying salt can be intensely thinned (Figure 1.12b). The sense of layer-parallel shear beneath the overburden is typically directed top to downslope, which may be opposite the sense of shear recorded in synkinematic overburden sediments (e.g., Brun and Mauduit, 2008). Furthermore, salt thinning

beneath an extending overburden can be enhanced by increased aggradation in the subsiding hanging wall. Thus, layer-parallel wall rock translation can promote or oppose evacuation caused by a hydraulic gradient depending on the geometry and kinematics of the translating overburden (Figure 1.12c).

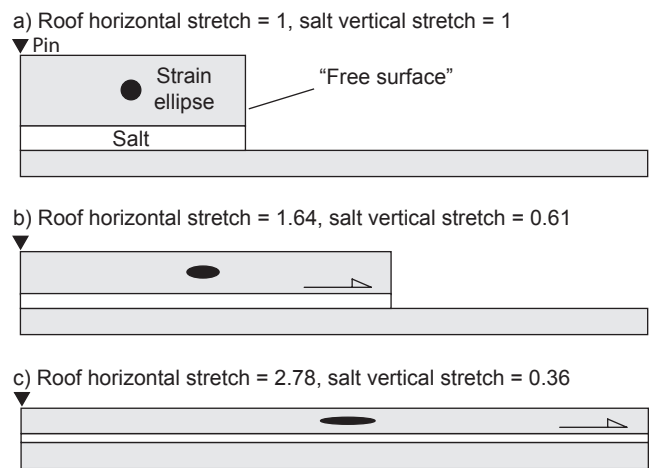
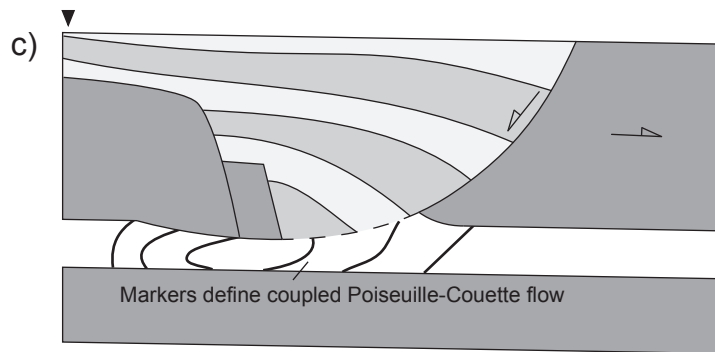
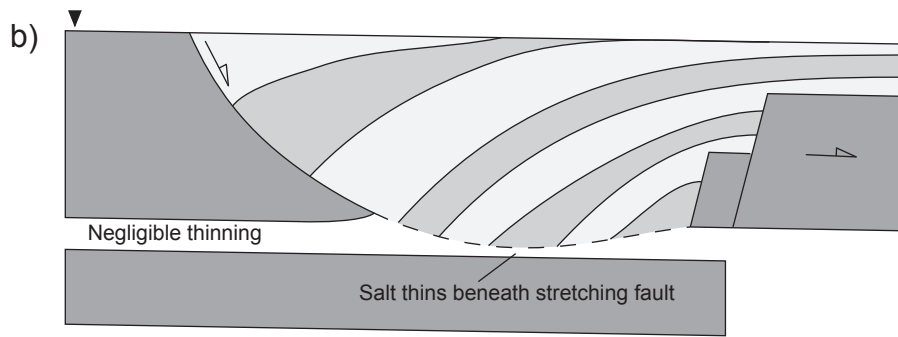
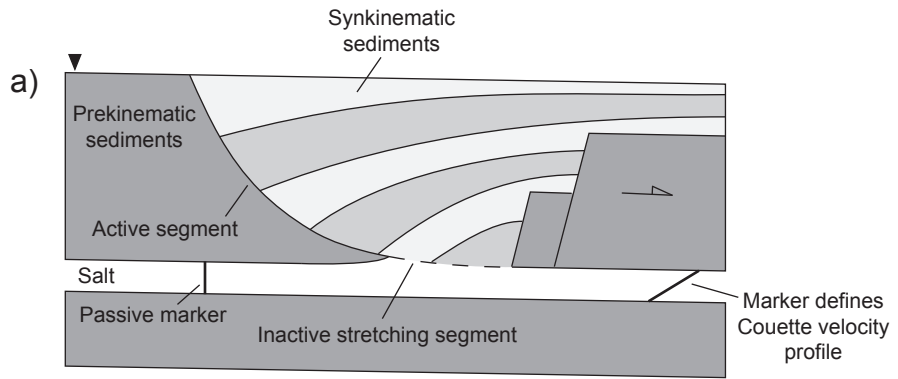


Figure 1.11: Schematic diagrams illustrating the difficulty in forming a salt weld by homogenous extension of the overburden. a) Two slabs of country rock are separated by a thin layer of salt and pinned at the left end of the diagram. b) The upper plate extends to the right, causing the salt contact along its base to lengthen. If salt area is conserved, the salt will thin proportional to the magnitude of extension. c) Even after extension of the upper plate to three times its original length, one third of the original salt thickness remains as a partial weld.

Figure 1.12: a) Schematic cross section illustrating overburden extension accommodated by a landward-dipping normal fault that soles into salt. Each fault is comprised of 1) an active segment that separates the sediments in the hanging wall from the sediments in the footwall and 2) an inactive segment that separates the brittle overburden sediments from the underlying ductile salt. b) As the overburden continues to extend, the inactive segment lengthens, causing the underlying salt to stretch and thin. Thinning in the salt accommodates the overburden, inducing a hydraulic gradient and enhancing evacuation. c) Salt evacuation beneath a translating and extending overburden is the result of the complex interaction between lengthening of the upper salt contact and evacuation caused by a hydraulic gradient. Velocity profiles schematically illustrate the complexity of this coupled Poiseuille-Couette flow. Cross sections after Brun and Mauduit, 2008.



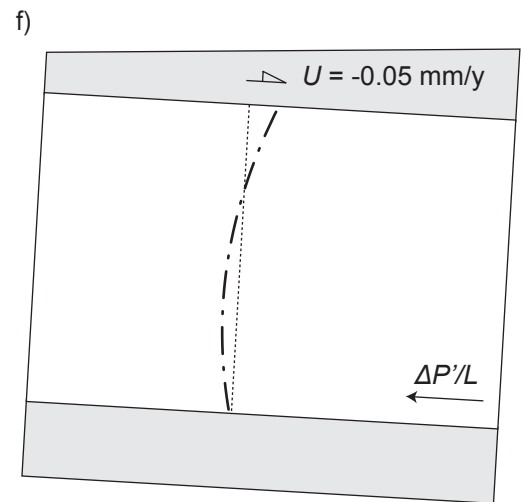
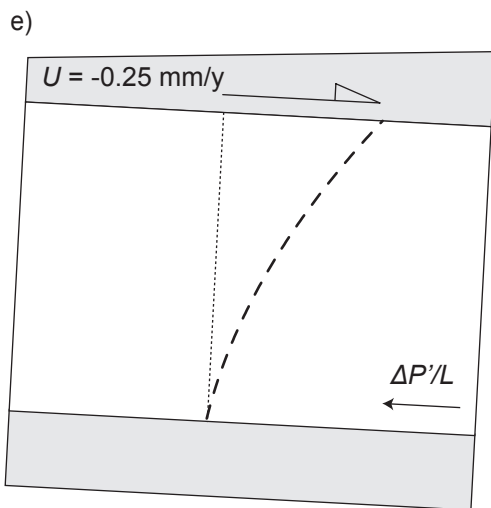
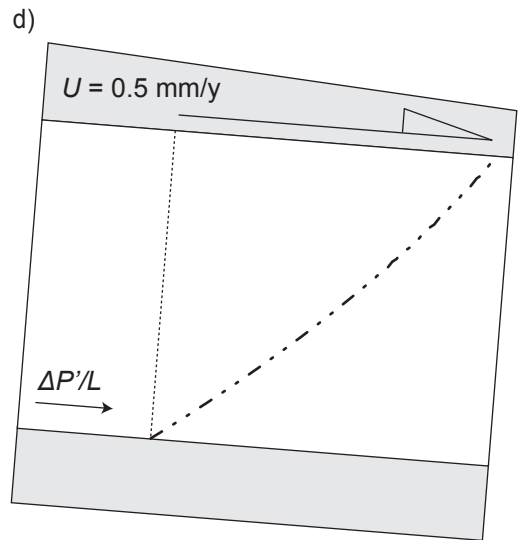
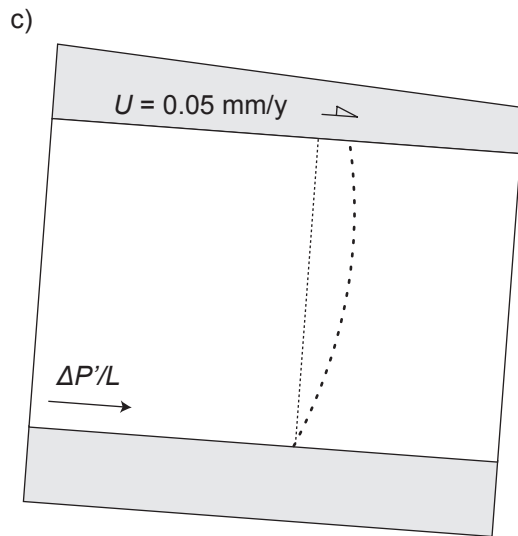
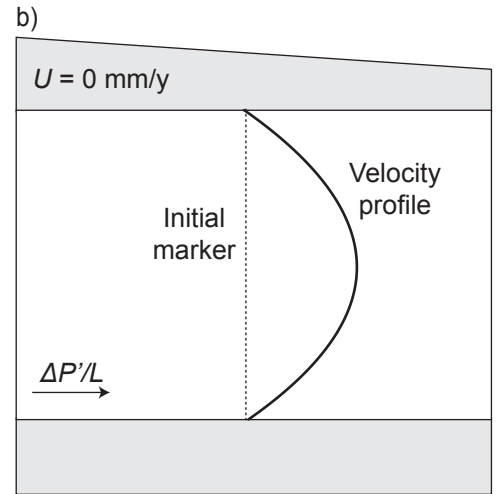
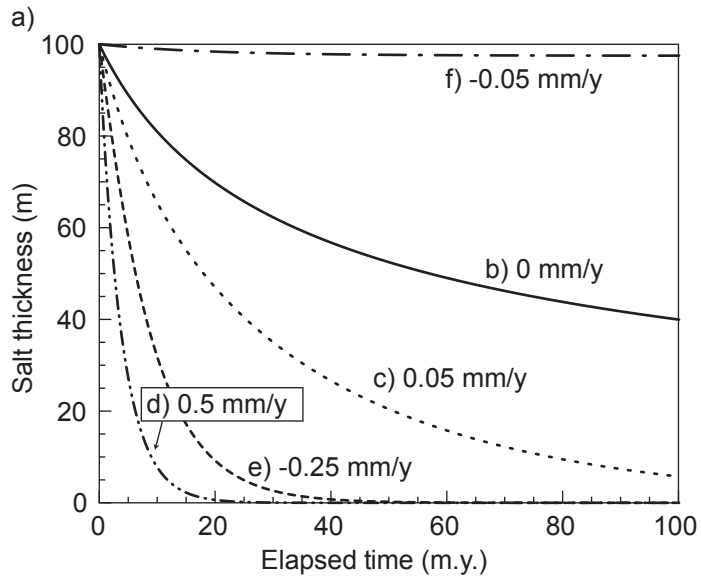
0 1 km  
V.E. × 1

Where a hydraulic gradient and layer-parallel wall rock translation act together to form a fault weld beneath a heterogeneously extending roof, salt evacuation is highly variable (Figure 1.13a) and described by the bracketed term in Equation 1.10. Positive shear velocity is parallel to the flow induced by a hydraulic gradient; negative shear velocity acts against this flow. When shear velocity is positive, layer-parallel wall rock translation and hydraulic gradient combine to enhance evacuation, and a complete weld may form (Figure 1.13b-c). Increasing the shear velocity of the roof accelerates welding (Figure 1.13d). A negative shear velocity counters hydraulic flow. If the flow contribution from shear velocity dominates, a complete weld may form (Figure 1.13e). If the contribution from hydraulic gradient dominates, salt thins until the two processes counteract each other and salt thickness does not appreciably change (Figure 1.13f). These effects are summarized in Table 1.1.

Table 1.1 Effect of shear displacement on welding

	$U > 0$	$U < 0$
$U < \frac{h^2}{6\mu} \left( \frac{\Delta P'}{L} \right)$	Fault weld Figure 1.11c	Equilibrium Hydraulic gradient dominates Figure 1.11f
$U > \frac{h^2}{6\mu} \left( \frac{\Delta P'}{L} \right)$	Fault weld w/ enhanced evacuation Figure 1.11d	Fault weld Shear displacement dominates Figure 1.11e

Figure 1.13: a) Evolution of salt thickness for fault welds calculated using Equation 1.10 with indicated shear velocities. A positive shear velocity acts parallel to flow caused by the hydraulic gradient. Flow length is 1000 m, viscosity is  $10^{19}$  Pa•s, flow stress is 1 MPa, and initial salt thickness is 100 m. Velocity profiles at the onset of flow are shown in (b), (c), (d), (e), and (f). The solid curve represents zero shear displacement (b). Shear displacement acting parallel to hydraulic gradient flow may form a nearly complete weld (c) & (d). If large enough, shear displacement acting against hydraulic gradient flow may form a nearly complete weld (e) or not appreciably change salt thickness (f).



In a fault weld, contact roughness can enhance evacuation by dragging salt away from the weld, much like grooves gouged on a fault surface. Discontinuous wedges of gypsum are exposed along a secondary salt weld in the La Popa Basin, northeastern Mexico, which is inferred to have undergone reverse displacement along the weld surface (Giles and Lawton, 1999). Asperities along the La Popa weld surface may have segmented an originally continuous gypsum body into the wedges exposed today. Taken to the extreme, a sufficiently thin partial weld may be faulted out, completely removing the salt, but the relative contributions of dissolution and slip have not been established. Furthermore, faults through thinned or absent salt can create high-permeability damage zones that can act as pathways for cross-weld migration of subsurface fluids.

#### **THINNING OF A MULTILAYERED EVAPORITE SEQUENCE**

So far I have examined only a single layer of pure salt. Salt is commonly interbedded with other evaporites, or with carbonate, siliciclastic, exhalative, or igneous rocks. Examples of interbedded evaporite formations are numerous and include the Messinian in the Mediterranean (Hsü et al., 1973), the Hormoz and Kavir in Iran (Kent, 1979; Jackson et al., 1990), the Zechstein evaporites in Northern Germany and surroundings (Tucker, 1991; Strohmenger et al., 1996), and evaporites in the Santos Basin, offshore Brazil (Cobbold et al., 1995;

Gamboa et al., 2008). Even the Louann salt in the Gulf of Mexico, which is uncharacteristically pure for a giant evaporite formation, contains up to about 5% anhydrite and some bittern salts. Repeated cycles of carbonate, halite, anhydrite/gypsum, and bittern salts are common results of the classic evaporation sequence first recognized by Usiglio (1849). The presence of multiple lithologies can retard mobility, but the incredible variety of salt structures in basins containing interbedded and impure evaporites indicates they are more than capable of considerable flow.

Dynamic viscosity, and in particular its distribution within the layered sequence, is a critical control on flow. Estimates of dynamic viscosity for common evaporites are included in Table 1.2. In evaporites, viscosity generally decreases with increasing solubility such that the last evaporites to precipitate from seawater are the most mobile. Stiff non-evaporite lithologies may undergo brittle deformation as they are dismembered by flow, but for modeling purposes it is appropriate to use viscosities a few orders of magnitude larger than salt.

Table 1.2 Dynamic viscosities of common evaporites

Evaporite	Chemical formula	Viscosity (Pa•s)	Source
Halite	NaCl	$\sim 1 \times 10^{18}$	van Keken et al. (1993)
Anhydrite	CaSO <sub>4</sub>	$*2.7 \times 10^{19}$	Zulauf et al. (2009)
Carnallite (Wet)	KMgCl <sub>3</sub> •6H <sub>2</sub> O	$\sim 1 \times 10^9$	Warren (2006)
Gypsum (Wet)	CaSO <sub>4</sub> •2H <sub>2</sub> O	$\sim 1 \times 10^{16}$	Griggs (1940)
Sylvite	KCl	$\sim 1 \times 10^{11}$	Höfer (1958)

\*Calculated as 27 times more viscous than halite with viscosity  $1 \times 10^{18}$  Pa•s.

To investigate how multilayered evaporites flow in response to a hydraulic gradient, the constants of integration in Equation 1.5 are determined by solving a system of equations with special boundary conditions at layer interfaces. Instabilities along layer contacts are ignored because of the immiscibility of individual layers and the extremely low Reynolds number of the flow (Yiantsios and Higgins, 1988). Rigid interlayers, such as non-evaporite lithologies, are treated as no-slip surfaces at the onset of flow. Determining the constants of integration for rigid layers is trivial; the total discharge is the sum of the discharges for each viscous layer (Equation 1.20). As the viscosity contrast between neighboring layers tends to zero, Equation 1.20 reduces to that for a single viscous layer.

$$q_{total} = -\frac{1}{12} \left( \frac{\Delta P'}{L} \right) \sum_{i=1}^n \frac{h_n^3}{\mu_n} \quad (1.20)$$

At the onset of flow, velocity and shear stress are continuous between interlayers (Equation 1.21). As the flow matures, boudinage will dismember stiff, high-viscosity interlayers, decreasing the effective dynamic viscosity of the whole sequence (Davison et al., 1996a) and modifies the boundary conditions between layers.

$$\begin{aligned} u_i(h_i) &= u_{i+1}(h_i) \\ \mu_i \partial_z u_i(h_i) &= \mu_{i+1} \partial_z u_{i+1}(h_i) \end{aligned} \quad (1.21)$$

Determining the constants of integration is less straightforward than for the single salt layer; continuity of shear stress requires constant  $A$  for all layers, but continuity of velocity requires  $B$  to change as a function of viscosity contrast and flow thickness. A flow having  $n$  layers yields a nonlinear system of  $n$  equations (Equation 1.22), from which interlayer flow velocities, discharges, and thicknesses through time can be numerically approximated by forward-difference techniques.

$$\begin{aligned} u_{i=1 \rightarrow n} &= \frac{z^2}{2\mu_i} \left( \frac{\Delta P'}{L} \right) + Az + B_i \\ B_1 &= 0 \\ B_{i=2 \rightarrow n-1} &= \frac{z_{i-1}^2 \mu_i}{2\mu_{i-1}} \left( \frac{\Delta P'}{L} \right) + \frac{Ah_{i-1} \mu_i}{\mu_{i-1}} + \frac{B_{i-1} \mu_i}{\mu_{i-1}} - \frac{z_{i-1}^2}{2} \left( \frac{\Delta P'}{L} \right) - Ah_{i-1} \\ B_n &= U - \frac{z_n^2}{2} \left( \frac{\Delta P'}{L} \right) - Az_n \\ A &= \frac{\left( \frac{z_{n-1}^2}{\mu_n} - \frac{z_{n-1}^2}{\mu_{n-1}} - \frac{z_n^2}{\mu_n} \right) \left( \frac{\Delta P'}{2L} \right) - \frac{B_{n-1}}{\mu_{n-1}} + U}{\left( \frac{z_{n-1}}{\mu_n} - \frac{z_{n-1}}{\mu_n} + \frac{z_n}{\mu_n} \right)} \end{aligned} \quad (1.22)$$

Equations 1.20 and 1.22 completely bracket the range of behavior of a multilayered sequence of evaporite and non-evaporite lithologies flowing viscously for hydraulic-gradient boundary conditions (Figure 1.14). Shear strain is

preferentially partitioned into low-viscosity layers and can lead to the formation of shear fabrics including S-C mylonites (e.g., Lister and Snoke, 1984; Ross and Bauer, 1992), particularly near the edges of the evaporite sequence. High-viscosity layers near the center of the evaporite sequence tend to extend under pure shear and may boudinage (e.g., Davison et al., 1996b). These differing behaviors become more obvious as the viscosity contrast between layers increases.

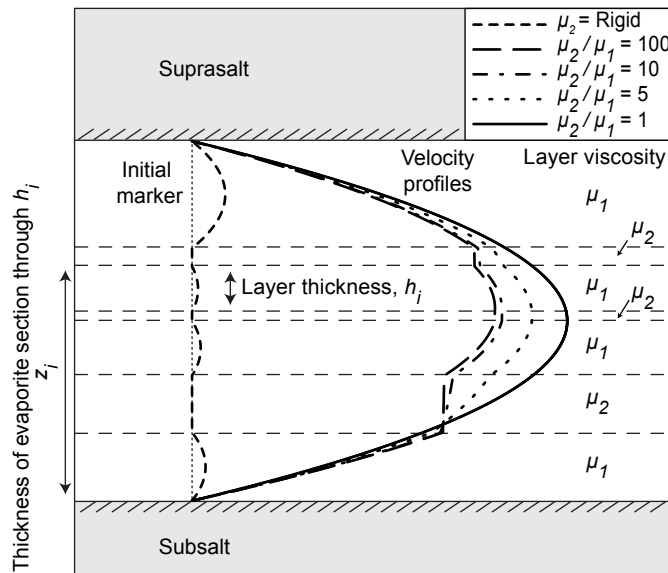


Figure 1.14: Velocity profiles in a layered sequence of low viscosity ( $\mu_1$ ) and high viscosity ( $\mu_2$ ) layers. As the viscosity contrast between layers increases, flow becomes increasingly plug-like. Rigid layers greatly retard the flow velocity.

Multilayered evaporites have endless permutations of layer thickness and viscosity. The distribution of thickness and viscosity within a multilayered evaporite sequence controls the velocity profile (Figure 1.15a) as well as the evacuation rate and the thickness of the resulting weld (Figure 1.15b). Rigid and high-viscosity interlayers inhibit evacuation, and increasing their number or thickness increases the thickness of the resulting weld. High-viscosity layers near the contact of an evaporite sequence will greatly inhibit flow and result in a thicker partial weld. Conversely, low-viscosity layers near the contact of a multilayered sequence allow faster flowing layers to envelop high-viscosity layers in the center of the channel, resulting in plug-like flow and a thinner partial weld.

Although this discussion has focused on the mechanical response of competent layers alternating with less-competent halite, the equations and diagrams also apply to extremely mobile layers, such as potash evaporites, alternating with more-competent halite. Beyond the scope of this study are the effects of vertical loading of inclined sequences of layered evaporites. The gravitational component of shear parallel to inclined evaporite layers is likely to lead to more complex strain patterns than modeled here, especially where there are large viscosity contrasts between the layers.

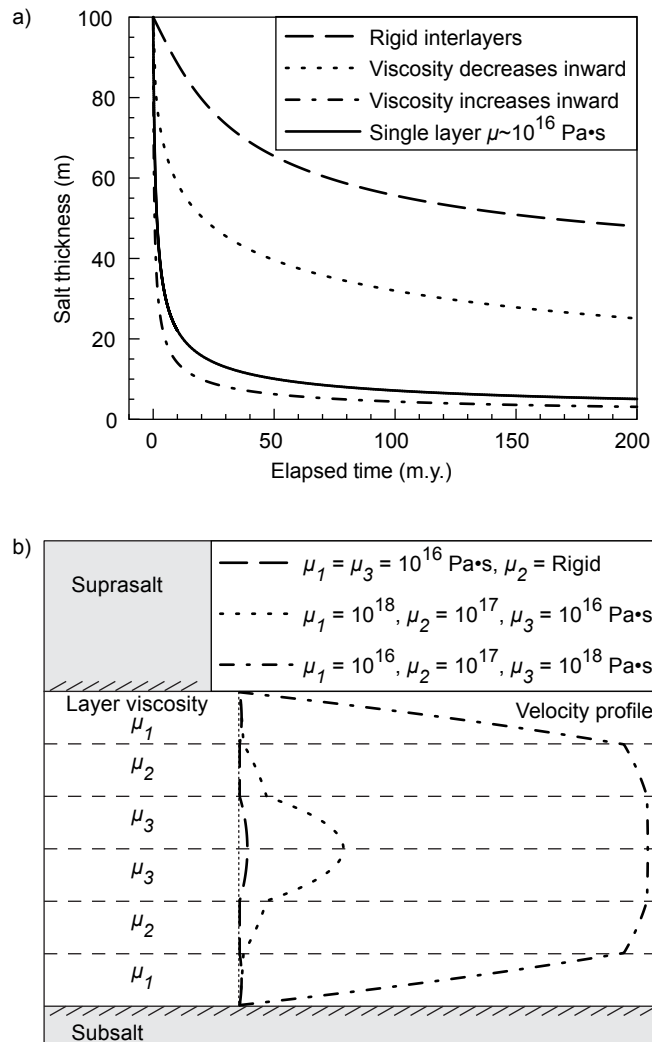


Figure 1.15: a) Evolution of thickness using Equation 1.20 and 1.22 for a multilayered sequence. For the dotted line, a viscosity of  $10^{18}$  Pa·s was used for layers at the edge of the flow, and  $10^{16}$  Pa·s was used for layers within the flow. This distribution was reversed to obtain the dashed-dotted line. Rigid interlayers resist evacuation the most, followed by flows in which viscosity decreases inward, and finally flows in which viscosity increases inward. The solid curve represents a single pure layer for comparison. b) Velocity profiles at the onset of evacuation for the examples in (a).

Different lithologies may be preferentially expelled from a multilayered evaporite sequence and into near salt structures. Kupfer (1968) called this phenomenon *differential purification by movement* and used it to explain the unusual purity of diapirs in the Gulf Coast. He based this conclusion on the pioneering physical models of Escher and Kuenen (1929) and further reasoned that the degree of chemical homogeneity could be used to estimate the distance of diapir rise. Talbot and Jackson (1989) rejected the concept, citing the extremely heterogeneous nature of the Hormoz diapirs exposed in southern Iran, and contended the composition of diapirs could only reflect the composition of the source layer.

Both arguments have merit. Any differential purification is controlled by the mechanical behavior and viscosity distribution of the multilayered sequence (Figure 1.16). This mathematical modeling suggests that for rigid interlayers, evacuation preferentially expels more mobile layers, as advocated by Kupfer (1968). If interlayer viscosities decrease toward the center of the flow, less viscous lithologies are preferentially expelled. However, if interlayer viscosities increase inwards, *more* viscous lithologies are preferentially expelled, which is consistent with the abundance of impurities exposed in emergent Hormoz diapirs noted by Talbot and Jackson (1989). In this respect the intricate models of Escher and Kuenen (1929) were misleading in having slip between diapiric multilayers of different viscosities (Figure 5 in Kupfer, 1968). This slip violates the

assumption of continuity of shear stress between layers, and Escher and Kuenen (1928) noted that layer cohesion in their physical experiments was imperfect. Interlayered halite and anhydrite do not undergo differential purification during experimental shear (Ross et al., 1987; Ross and Bauer, 1992) or constriction (Zulauf et al., 2009). Outcrops of extrusive salt show that strain can localize in shear zones within or at the boundaries of a ductile salt layer (Talbot, 1979; Miralles et al., 2001), yet many observations indicate strain continuity across different lithologies (e.g., Talbot, 1979; Jackson and Talbot, 1989; Burliga, 1996; Davison et al., 1996b; Miralles, 2001). During progressive flow, boudinage will dismember stiff interlayers (Zak and Freund, 1980; Burliga, 1996; Davison et al., 1996b; Zulauf et al., 2009). Without knowing the composition of the original evaporite and the viscosity of each layer, the effect of any hypothetical differential purification cannot be determined.

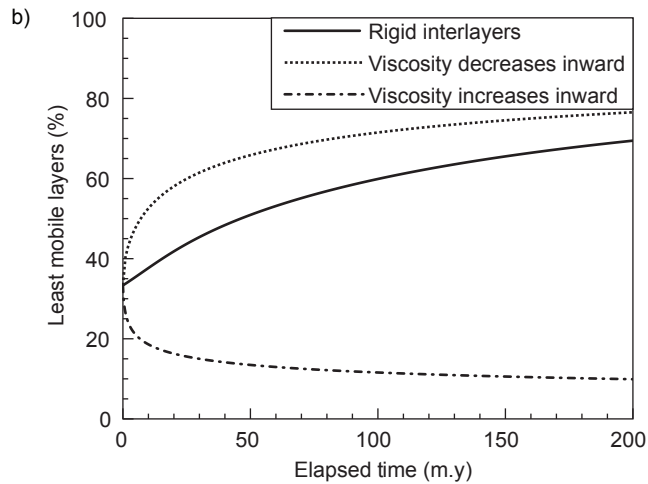
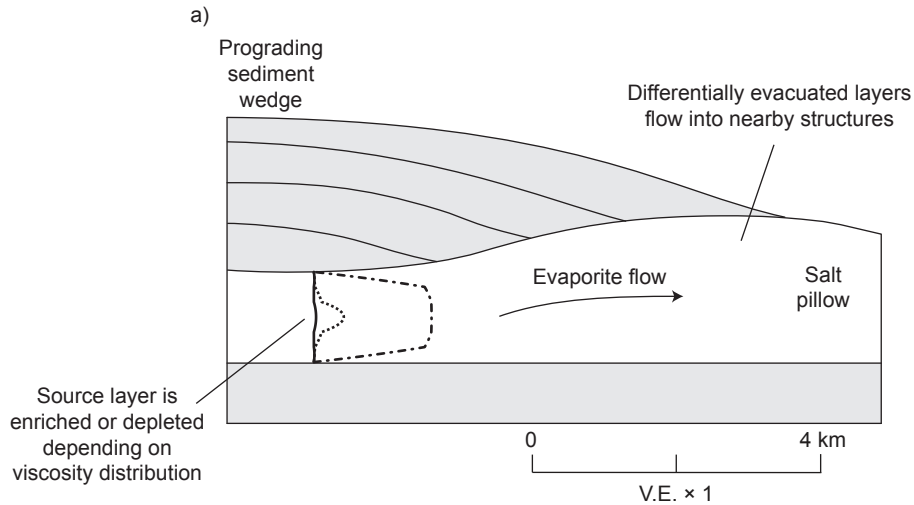


Figure 1.16: a) Schematic cross section illustrating the differential evacuation of a multilayered evaporite (see Figure 1.15b) into a nearby salt structure. b) Evolution of source layer composition for layered evaporites in (a). Low-viscosity layers are preferentially evacuated when they are located in the interior of the sequence or are sandwiched between rigid layers. High-viscosity layers are preferentially evacuated when they are located in the interior of the sequence.

Compositional variations in evaporites in 41 proprietary wells in the Campos Basin are consistent with differential evacuation of more mobile halite with respect to less mobile anhydrite. Thick evaporite sections contain abundant halite and minor anhydrite, but thin sections contain mostly anhydrite (Figure 1.17). Halite is only present in one of the 21 wells containing less than 50 m of evaporites. In nine wells, halite is sandwiched between anhydrite layers at the top and base of the section. The preponderance of anhydrite in thin evaporites could suggest that low-viscosity halite layers were expelled into growing salt structures more rapidly than high-viscosity anhydrite layers. However, other processes, such as facies variations and preferential dissolution of halite and potash evaporites are less speculative because they have been directly observed in geologic sequences, commercial salt ponds, and the laboratory.

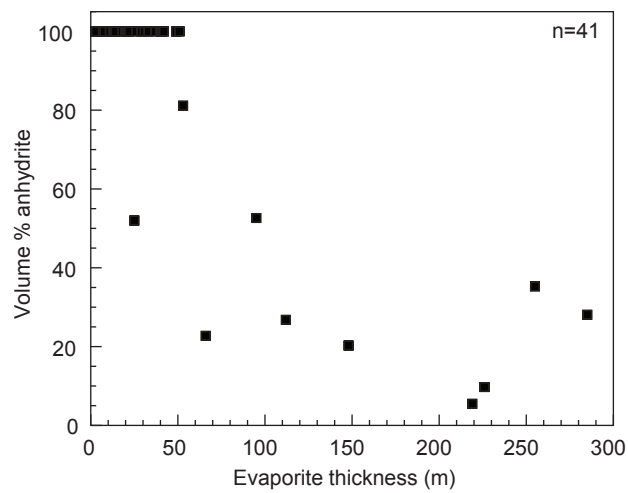


Figure 1.17: Anhydrite proportion versus evaporite thickness for 41 wells in the Campos Basin, offshore Brazil. Wells drilled through thin evaporites typically encountered more anhydrite than wells drilled through thick evaporites. This phenomenon may be explained by differential purification, but it may also be the result of facies variation or preferential dissolution of halite and other highly soluble evaporites.

When drilling through evaporites, creep can cause a number of expensive drilling problems ranging from stuck tools to collapsed wellbores. Problems typically arise when drilling thin low-viscosity bittern salts, such as sylvite or carnallite, which may be only a few meters thick. Thin, low-viscosity evaporites are problematic because they are poorly imaged on subsurface data and flow rapidly compared with more common evaporites, such as halite (Figure 1.16). Fortunately, if low-viscosity layers are anticipated based on prior drilling experience or superior subsurface data, analytical techniques (e.g., Carcione et al., 2006) can be used to predict creep and properly engineer the drilling program to mitigate creep.

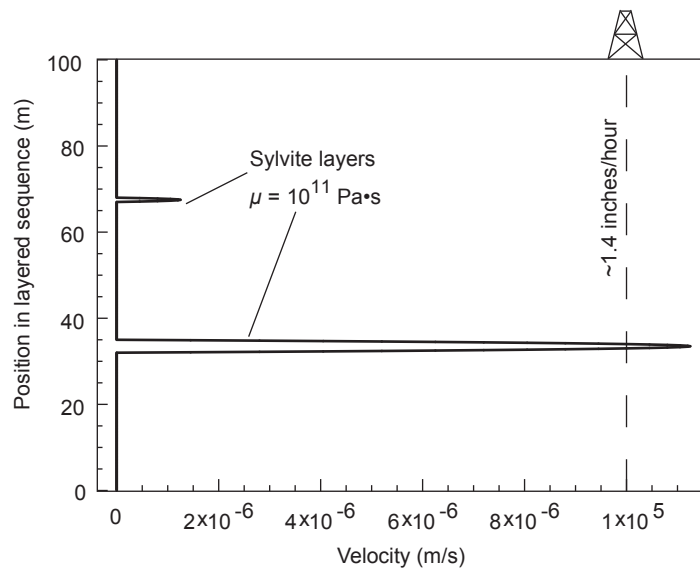


Figure 1.18: Velocity profile illustrating the extreme mobility of thin, low-viscosity bittern salts. The spikes in the solid curve correspond to a 1 m thick layer of sylvite (upper spike) and a 3 m thick layer of sylvite (lower spike) having a viscosity of  $10^{11}$  Pa·s flowing in response to a 1 MPa hydraulic gradient. Rapidly flowing evaporite layers can damage drilling equipment and jeopardize well control. For example, a 9-inch hole drilled through the lower sylvite layer will completely close in just over six hours.

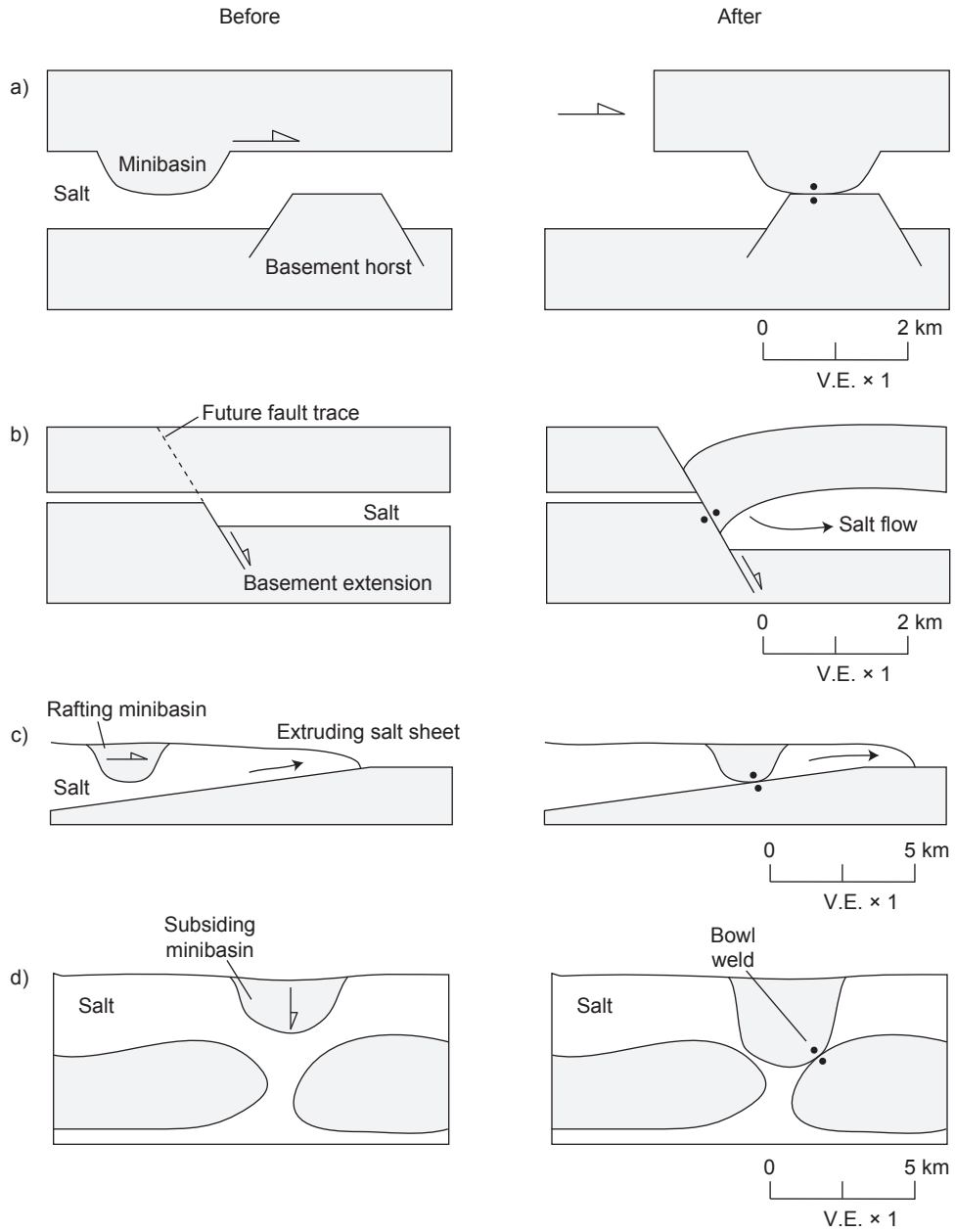
## DISCUSSION

The preceding models approximate salt evacuation for ideal geometries. Salt evacuation in nature is obviously more complex, but what is the effect of these complexities on welding? To generalize, the tendency of boundary drag to resist evacuation depends on flow restriction, which can be viewed as the ratio of salt thickness to flow length. When flow length is much larger than salt thickness ( $L/h \gg 1$ ), viscous flow is severely limited by boundary drag, and evacuation is slow and incomplete. For example, the preceding models suggest salt is difficult to evacuate from beneath a prograding sediment wedge (Figure 1.7a) or beneath a flat-bottomed minibasin (Figure 1.9b). Taken to the extreme, thin salt whose escape would require long-distance flow is effectively trapped by boundary drag and indefinitely resists evacuation. When flow length is much smaller than salt thickness ( $L/h \ll 1$ ), evacuation occurs readily. For example, virtually all salt can be evacuated from beneath a hemispherical minibasin (Figure 1.7c) or other indenting or angular salt boundaries. In all cases, salt evacuation can be enhanced by layer-parallel translation of wall rock and stretching of the salt contacts (Figure 1.13) to produce welds that are all but complete. Furthermore, substantial thinning is not necessary for layer-parallel wall-rock translation to produce a nearly complete weld. Instead, wall-rock translation can juxtapose salt contacts without having to overcome some of the limiting effects of boundary drag (1.19). Welds formed in this manner result largely from serendipitous

combinations of geometry and displacement conditions such that the associated flow lengths are small and evacuation is vigorous.

Well penetrations through welds are somewhat scarce and rarely published, so model predictions of remnant evaporite thickness in real welds are difficult to validate. About 75 wells in the greater Campos Basin, offshore Brazil, have drilled through interlayered evaporites in the Retiro member of the Aptian Lagoa Feia Formation (or the non-evaporite equivalent). Forty-one wells encountered evaporites thinner than 100 m. Only 10 wells encountered halite and anhydrite, but the remaining 31 wells contained only anhydrite. Some of these may have contained halite in the geologic past. I argue these wells contain examples of complete welds, at least in the sense that halite has been completely removed by viscous flow and probable dissolution. However, remnant anhydrite and the few examples with remnant halite attest to the exponentially increasing resistance of boundary drag to viscous flow. Based on these wells and the model predictions, a typical weld formed by viscous flow alone can be expected to contain anywhere from a vanishingly thin ( $\ll 1$  m) veneer to up to  $\sim 50$  m of salt. If the boundary conditions of the flow change, some additional salt can be removed by viscous flow, but ultimately that remnant salt can only be completely removed by dissolution or faulting or by serendipitous combinations of geometry and displacement (Figure 1.19).

Figure 1.19: Schematic cross sections illustrating natural geometries that minimize boundary drag and promote nearly-complete welds by viscous flow alone. a) Irregularities along the base or top of salt can be juxtaposed by layer-parallel translation of wall rocks. A complete weld can only form where the irregularities are perfectly aligned, but no salt thinning is required. b) Basement-involved extension (or evacuation from a lower salt level) can cause overburden subsidence and rotation, welding the overburden against a basement high. Again, the subsiding overburden must be perfectly aligned to form a complete weld, but evacuation beneath the subsiding overburden is not limited by boundary drag. c) A minibasin is carried along the top of an extruding salt sheet. As the minibasin translates, its base grounds on a subsalt ramp, forming a weld. d) A minibasin may initiate above a relict salt feeder beneath a salt canopy. If the minibasin subsides, it can settle in the throat of the feeder to form a *bowl weld*.



## CONCLUSIONS

The models discussed here elucidate how viscous flow contributes to salt welding and the sensitivity of salt evacuation to important physical variables and boundary conditions.

1) Viscous flow will result in a partial weld containing up to ~50 m of salt depending on the boundary conditions and geometry of salt flow. Evacuation rate increases with increasing driving forces or decreasing viscosity and flow restriction. Partial welds may contain a few tens of meters thickness of salt where flow is restricted or sluggish, and partial weld thickness decreases with lower viscosity, shorter flow length, and greater driving forces. Layer-parallel wall rock translation or dissolution are needed to remove any remaining salt to produce a complete weld. Based on these conclusions and natural examples, many welds can be expected to contain some remnant salt.

2) Layer-parallel wall rock translation affects evacuation history and remnant evaporite thickness in a fault weld. Thinning occurs when the salt contacts lengthen during shear displacement and can be enhanced by local thickening in the overburden. In the absence of a hydraulic gradient, layer-parallel translation of wall rock will form welds where the overburden extends heterogeneously or where serendipitous geometry and displacement conditions

minimize boundary drag. The evolution of a fault weld depends on the orientation and magnitude of layer-parallel translation of wall rocks with respect to the hydraulic gradient. In many scenarios, layer-parallel wall rock translation enhances salt evacuation.

3) Evacuation of multilayered evaporites is promoted by low-viscosity layers near the edges of the sequence and inhibited by high-viscosity layers near the edges of the sequence. More mobile or less mobile interlayers may be differentially evacuated depending on the viscosity distribution in the multilayered sequence. Low-viscosity layers at the interior of the sequence can be preferentially evacuated into nearby salt structures, leaving high-viscosity layers near the edges of sequence.

#### **ACKNOWLEDGEMENTS**

I thank Martin Jackson, Mike Hudec, Mark Cloos, Ron Steel, and Mrinal Sen at the Jackson School of Geosciences and Frank Peel of BHP Billiton for comments and reviews, Devon Energy for facilitating the senior author's research and access to well data. This research was funded by the Jackson School of Geosciences and the Applied Geodynamics Laboratory, a salt tectonics research consortium at the University of Texas at Austin.

## CHAPTER 2: SEISMIC CHARACTERIZATION OF SALT WELDS IN SALT TECTONICS REGIMES

### ABSTRACT

On reflection-seismic sections, salt welds, areas of thinned or completely removed salt, often appear as a single reflection displaying variable seismic character and are commonly associated with degraded seismic image quality, especially beneath the weld. Where rock salt is thicker than the temporal resolution of the seismic data, typically ~25 - 50 m of halite for many modern surveys, separate reflections corresponding to the base and top of the salt are produced. Analysis of synthetic seismograms and real-world examples indicate two-way travel time can be used to estimate evaporite thickness above the temporal resolution of seismic data. Below this limit, the top and bottom reflections converge and interfere, creating a single composite reflection. The term *seismic weld* refers to this composite reflection, which displays highly variable seismic character depending on the seismic properties and morphology of the rocks above, below, and inside the weld. Remnant evaporite thickness in a seismic weld can be estimated using amplitude information to provide guidelines for first-pass interpretations. More sophisticated methods, such as spectral inversion, are required to produce more accurate estimates of evaporite thickness.

## INTRODUCTION

Though the concept of vanished evaporites had been known for decades (e.g., Trusheim, 1960), *salt welds* were first named and classified based on seismic data by Jackson and Cramez (1989), who provided guidelines for interpreting the origin of welds based on the stratigraphic and structural architecture of the overburden. At the most basic level, a *complete weld* is the structure that forms when salt is completely removed from between wall rocks by viscous flow and dissolution. Viscous evacuation is limited by boundary drag along salt contacts (e.g., Cohen and Hardy, 1996; Chapter 1) and dissolution is limited by the availability of dissolving fluids (e.g., Anderson and Kirkland, 1980; Ge and Jackson, 1998), such that many welds contain remnant salt. Thus, a weld that contains up to ~50 m of remnant salt is called a *partial weld* (Chapter 1). Here, the term *salt weld* refers to both complete welds and partial welds.

Reflection seismology is the principal tool used to identify salt-related structures and map salt welds in the subsurface. Welds have been identified in evaporite basins around the world including the Gulf of Mexico (e.g., Jackson and Cramez, 1989; Schuster, 1995; Rowan et al., 1999), the salt basins in offshore Brazil (e.g., Mohriak et al., 1995; Roberts et al., 2004) and West Africa (e.g., Buroillet, 1975; Duval et al., 1992; Gottschalk et al., 2004), the North Sea (Buchanan et al., 1996) the Paradox Basin (Trudgill et al., 2004) and the Scotian margin (Ings and Shimeld, 2006). Where evaporites are thick, a typical reflection-

seismic profile displays separate reflections that correspond to the top and base of the evaporites (Figure 2.1). These upper and lower reflections converge at the limit of vertical seismic resolution, which for a peak frequency of 10-30 Hz (common in modern surveys) represents ~25-50 m of halite. Below this limit, partial welds and complete welds are indistinguishable based on travel time differences alone. For this reason, many salt welds are seismically complete and produce only a single reflection on seismic data. Of course, the tendency for reflections to be produced at the evaporite contacts depends on the sharpness of the transition from evaporite to non-evaporite lithologies.

Thick beds of halite and other evaporites make excellent seals for hydrocarbon accumulations because of their microcrystalline structure and ductile rheology (e.g., Downey, 1984; Warren, 2006). Approximately 30% of the world's conventional hydrocarbon reserves are sealed by thick evaporites (Weber and Sarg, 2005) including recent multi-million barrel discoveries such as Tupi beneath thick (> 1km) Aptian salt in the Santos Basin. In contrast, other discoveries, such as Auger, Holstein, and Marco Polo in the Gulf of Mexico, have required cross-weld hydrocarbon migration. The capacity of a given weld to seal depends on a number of factors, including the permeability of the sediments surrounding the weld (Rowan, 2004) as well as the continuity of any remnant evaporites (Warren, 2006).

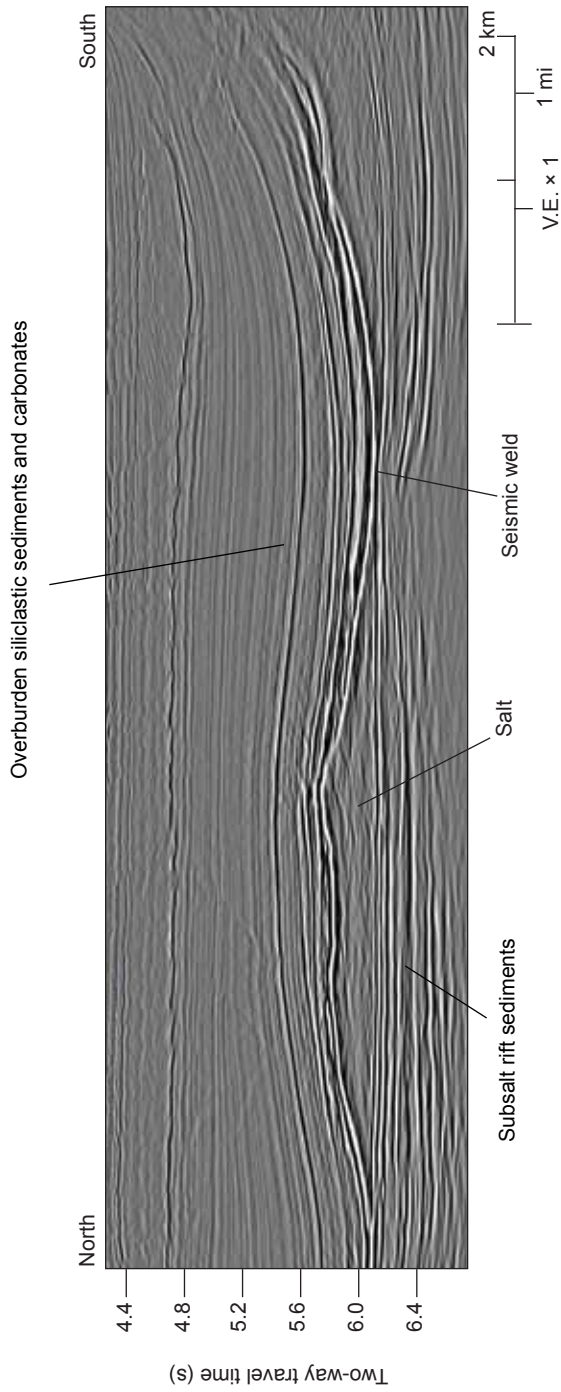


Figure 2.1: Prestack time-migrated seismic section illustrating a seismic weld located in the Campos Basin, offshore Brazil. Autochthonous salt, which lacks internal reflectors, thins into a salt weld near the middle of the section. Separate reflections corresponding to the top and base of salt are apparent where the salt is thick, but are impossible to interpret through the weld itself. Seismic data provided courtesy of Petroleum Geo-Services (PGS).

Warren (2006) suggested evaporites thicker than 30 m make excellent seals, but thinner evaporites may be prone to leaking. Thin evaporites in a partial weld can be disrupted by faults or fractures to allow focused migration of hydrocarbons and other subsurface fluids (e.g., Davison et al., 1996; Davison, 2009). Many evaporites contain sedimentary inclusions, such as sandstone, which are more permeable than halite. In thick evaporites, the chance that these inclusions can form a through-going permeability pathway is less than for a thin evaporites. If a sedimentary inclusion is as thick as its encasing evaporite, cross-weld migration is likely. Evaporites may also become slightly permeable after dilatant microcracking (e.g., Peach and Spiers, 1996; Popp et al., 2001; Schulze et al., 2001) or deep burial (e.g., Lewis and Holness, 1996), and thin evaporites provide a shorter migration pathway than thick evaporites. Furthermore, seismic-wave propagation is affected by remnant evaporites and the complex internal structure of evaporite welds, complicating seismic imaging efforts and degrading image quality. In spite of this significance, no published work has investigated how salt welds affect the propagation of seismic energy.

Vertical welds are much more difficult to clearly image than their horizontal counterparts. First, like all steeply dipping interfaces, the evaporite contacts in a vertical weld are poorly illuminated. Second, salt in a diapir may rise to feed a shallower salt sheet or salt-stock canopy before welding (e.g., Jackson et al., 2008), complicating imaging efforts by adding a layer of salt and concealing the

weld below. Finally, the sediments near a vertical weld are often deformed during episodic diapir rise and roof breakup (e.g., Giles and Lawton, 1999; Rowan et al., 2003; Schultz-Ela, 2003) or lateral shortening (e.g., Jackson et al., 1998; Dooley et al., 2009), further complicating wave propagation and processing efforts. For these reasons, this paper focuses on subhorizontal welds.

Detecting the presence and characterizing the thickness of remnant evaporites in a subhorizontal partial weld on reflection-seismic data is closely related to the classic problem of imaging a thin bed. This subject has been intensely researched in the exploration seismology community given its relevance to thin hydrocarbon reservoirs.

Ricker (1953) analytically examined the wavelet complex reflected from a thin bed in a homogeneous medium. He derived an expression for detectable layer thickness in terms of P-wave velocity ( $V_p$ ) and wavelet breadth ( $b$ ) provided the upper and lower reflections had identical polarity and amplitude. Widess (1973) concluded that thin beds are theoretically detectable (though not necessarily distinguishable from noise) down to one-eighth of the wavelength ( $\lambda_d$ ) of the predominant wavelet frequency. Below this limit, some information as to the true thickness of a thin bed is stored in amplitude variations of the reflected wavelet complex (e.g., Meckel and Nath, 1977; Neidell and Poggiagliolmi, 1977), but the results must be calibrated with a known bed thickness and seismic-wavelet (see discussion in Neidell and Poggiagliolmi, 1977). Koefoed and de

Voogd (1980) addressed the effects of transmission loss and internal multiples to consider large acoustic impedance contrasts for studying coal seams. However, their conclusions are equally valid for evaporite welds with high acoustic impedance ratios, such as a partial weld containing remnant anhydrite encased in undercompacted shale. Kallweit and Wood (1982) unified these notions of resolution and derived an expression for temporal resolution (the thickness of a bed resolvable by travel-time differences as opposed to one that is merely detectable) for both zero-phase Ricker and sinc (Shannon) wavelets (Figure 2.2). Temporal resolution ( $T_R$ ) is calculated using the peak frequency ( $f_p$ ) of the seismic data (Equation 2.1) and resolvable thickness ( $Z$ ) is calculated using the peak wavelength ( $\lambda_p$ ) of the imaged bed (Equation 2.2) (Kallweit and Wood, 1982).

$$T_R = \frac{1}{3.0f_p} \quad (2.1)$$

$$Z = \frac{\lambda_p}{6} \quad (2.2)$$

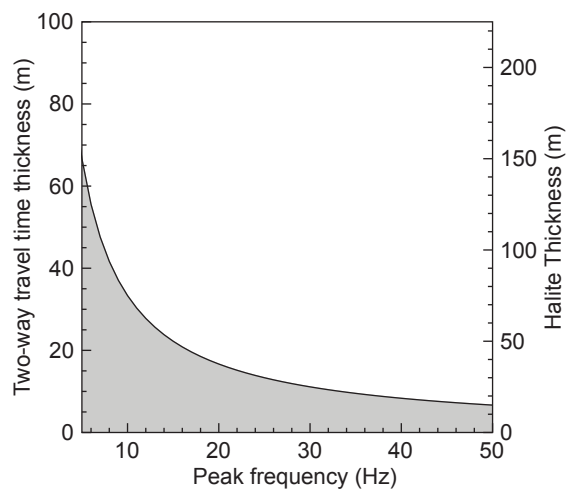


Figure 2.2: Plot of bed/halite thickness versus peak frequency demonstrating the concept of temporal resolution of Kallweit and Wood (1982). The gray area represents beds that cannot be accurately resolved using traditional methods (i.e., travel-time differences). Following the definition of Kallweit and Wood (1982), peak frequency is the frequency component corresponding to the largest value in the Fourier amplitude spectrum. An increase in peak frequency increases the resolving power of the reflection-seismic method. The frequency content of modern marine seismic surveys depends on several variables, but peak frequencies of 10 – 30 Hz are typical. Accordingly, halite beds less than ~25 – 50 meters thick cannot be resolved using travel-time difference alone.

Modern attempts to estimate bed thickness rely on seismic attribute analysis, such as spectral decomposition (e.g., Partyka et al., 1999; Marfurt and Kirlin, 2001). These methods require extensive post-processing and rely on calibrating information, such as well data. Here, the seismic properties of evaporites welds and their surroundings are summarized and basic interpretation techniques are applied to provide first-order estimates of the thickness of welded evaporites on reflection-seismic data. Where more accuracy is required, these results can be used to launch more sophisticated techniques, such as a spectral inversion (e.g., Puryear and Castagna, 2006, Rubino and Velis, 2009).

#### **SEISMIC PROPERTIES OF EVAPORITES, WELDS AND THEIR SURROUNDINGS**

Though the term *salt weld* overtly refers to a structure formed by the removal of rock salt composed primarily of halite, welds can form in any mobile layer susceptible to viscous flow or dissolution, including other evaporites and even undercompacted and overpressured shale (e.g., McDonnell et al., 2009). The term *evaporite weld* is used here to describe any structure resulting from the evacuation or dissolution of evaporites. Here, I focus on the most common evaporite minerals, halite and anhydrite.

Halite (NaCl) is one of the last minerals to precipitate from evaporating seawater according to the classic sequence discovered by Usiglio (1849). Halite is the most common evaporite mineral in mobilized giant evaporite deposits and

forms many of the structure commonly associated with salt tectonics. Halite has a face-centered cubic crystal structure with a crystal density of  $2163 \text{ kg/m}^3$  (Carmichael, 1984) and a primary acoustic wave (P-wave) velocity of approximately  $4544 \text{ m/s}$  as calculated from elastic moduli. Halite is commonly interbedded or mixed with other evaporite and non-evaporite lithologies such that  $2200 \text{ kg/m}^3$  and  $4500 \text{ m/s}$  are common approximations for the bulk density and P-wave velocity of rock salt, respectively (Hudec et al., 2009; Bourbie et al., 1987).

Unlike halite, anhydrite ( $\text{CaSO}_4$ ) is not thermodynamically stable at surface temperatures and pressures (Hardie, 1967). Though it is unlikely to precipitate in large quantities directly from seawater, anhydrite is nonetheless a common mineral in giant evaporite deposits. Gypsum ( $\text{CaSO}_4 \cdot 2\text{H}_2\text{O}$ ) precipitates from seawater during normal evaporation and then dehydrates to anhydrite in the shallow subsurface (typically 2 - 3 km depth) between  $50 - 100^\circ\text{C}$  depending on the chemical activity and fluid pressure of the pore fluid (Jowett et al., 1993). Anhydrite has an orthorhombic crystal structure and a crystal density of approximately  $2963 \text{ kg/m}^3$  (Carmichael, 1984) and a P-wave velocity of  $5662 \text{ m/s}$  as calculated from elastic moduli. Like halite, gypsum is typically deposited with other evaporites before dehydrating to anhydrite, so  $2900 \text{ kg/m}^3$  and  $5500 \text{ m/s}$  are common approximations for rock anhydrite (Bourbie et al., 1987). Halite and anhydrite are relatively incompressible (e.g., Voronov and Grigor'ev, 1976) but

undergo slight thermal expansion (Rubin et al., 1961; Evans, 1979), resulting in a decrease in density and P-wave velocity where deeply buried. In spite of this, the seismic properties of halite and anhydrite are not expected to vary widely at depths of practical interest in reflection seismology.

Seismic anisotropy in evaporites has received limited attention in the literature in spite of its effect on seismic imaging. Individual halite crystals are slightly anisotropic and P-waves traveling in the (110) crystallographic direction are approximately 5% slower than those in the (100) direction (Sun, 1994). Thus, bulk anisotropy can develop if halite crystals align during strain. The crystal anisotropy of anhydrite has not been quantified. Seismic anisotropy in rock salt is enhanced by lattice reorientation and alignment during dislocation glide (Raymer et al., 2000) but the effect is limited by fluid-assisted dynamic recrystallization, which limits the development of lattice-preferred orientations (e.g., Urai et al., 1987; Peach et al., 2001; Ter Heege et al., 2005). In multilayered evaporites, anisotropy can also result from original compositional layering, higher strains in less viscous layers during viscous flow (Ross et al., 1987; Zulauf et al., 2009; Chapter 1) or more dissolution in soluble layers. Seismic anisotropy in evaporite welds is beyond the scope of this study, and the effects of any anisotropy in this study are assumed to be negligible.

Thick sequences of halite and anhydrite typically include a wide variety of non-evaporite inclusions. Inclusions come from a variety of sources including

carbonates and siliciclastics deposited within evaporites (e.g., Tucker, 1991), weak country rock incorporated as xenoliths during diapir rise (e.g., Jackson et al., 1990), sutures between salt sheets (e.g., Rowan, 1995), founder minibasin or roof blocks (e.g., Kent, 1979; Ge et al., 1997), and even igneous intrusions (e.g., Gansser, 1960; Schwerdtner and Clark, 1967; Balkwill, 1978). Subsequent viscous flow can dismember these inclusions (Davison et al., 1996; Chapter 1), further complicating evaporite stratigraphy. Subsurface dissolution removes evaporites, starting with highly soluble minerals, such as halite, and leaving less soluble lithologies in its wake. Any combination of evaporites, inclusions, and insoluble residue can be left behind in a weld and affect its seismic character, particularly frequency content.

The frequency response of a seismic weld is controlled by interference between the upper and lower evaporite reflections (e.g., Sun, 2009) and by the degree to which the frequency content of the source wavelet is modified when it encounters salt. Salt contacts can be faulted or folded and thinned salt commonly contains complicated internal structures, such as flow folds and boudinaged inclusions produced during viscous flow (Figure 2.3). These structures scatter seismic energy and filter high frequencies, degrading seismic image quality within and below partial welds (Figure 2.4). The greater the complexity of structures in a partial weld, the more severe the reduction in frequency content and seismic image quality, especially below the evaporites.

Figure 2.3: Though evaporites often appear homogenous on migrated seismic sections, evaporites and evaporite welds are internally complex structures that affect the propagation of seismic energy. a) Folded top of salt reflection in the Campos Basin, offshore Brazil. Thin-skinned shortening of suprasalt Albian carbonates occurred immediately after deposition. b) Flow folds defined by carbonaceous layers and nodules in gypsum along the La Popa salt weld, northern Mexico. Flow folds are produced by viscous flow during diapir rise and weld formation and modified by near-surface dissolution. Width of view is ~ 1 m. Photograph by Martin Jackson. c) Carbonate boudin in black Hormoz salt in a Zagros salt glacier, Iran. Viscous flow in multilayered evaporites is controlled by the distribution of viscosity (Chapter 1). Carbonates are less mobile than evaporites and may boudinage during viscous flow. Photograph by Hemin Koyi.

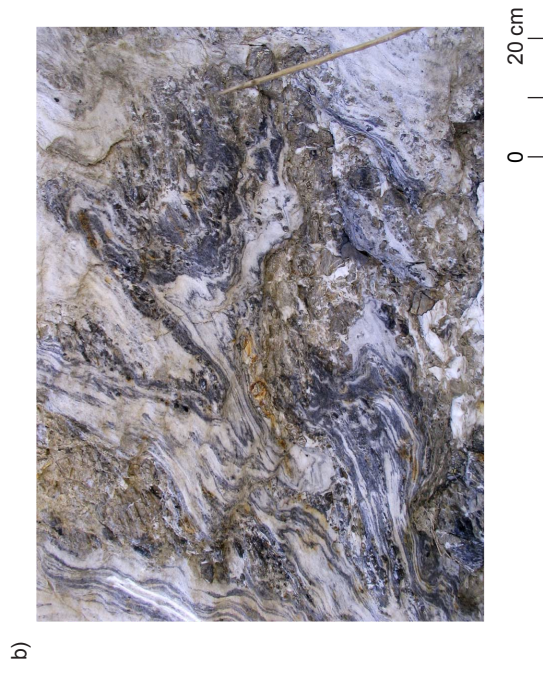
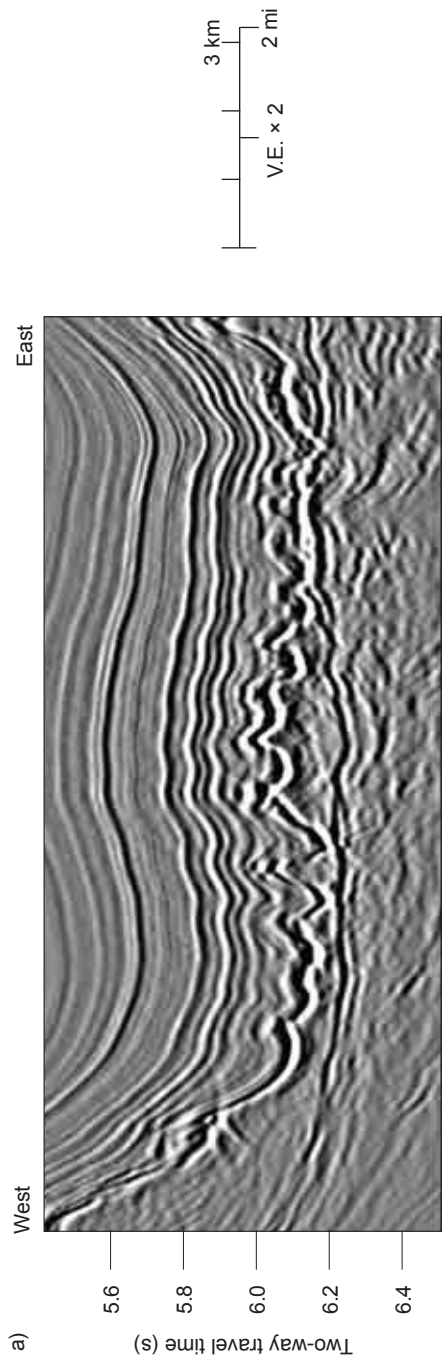
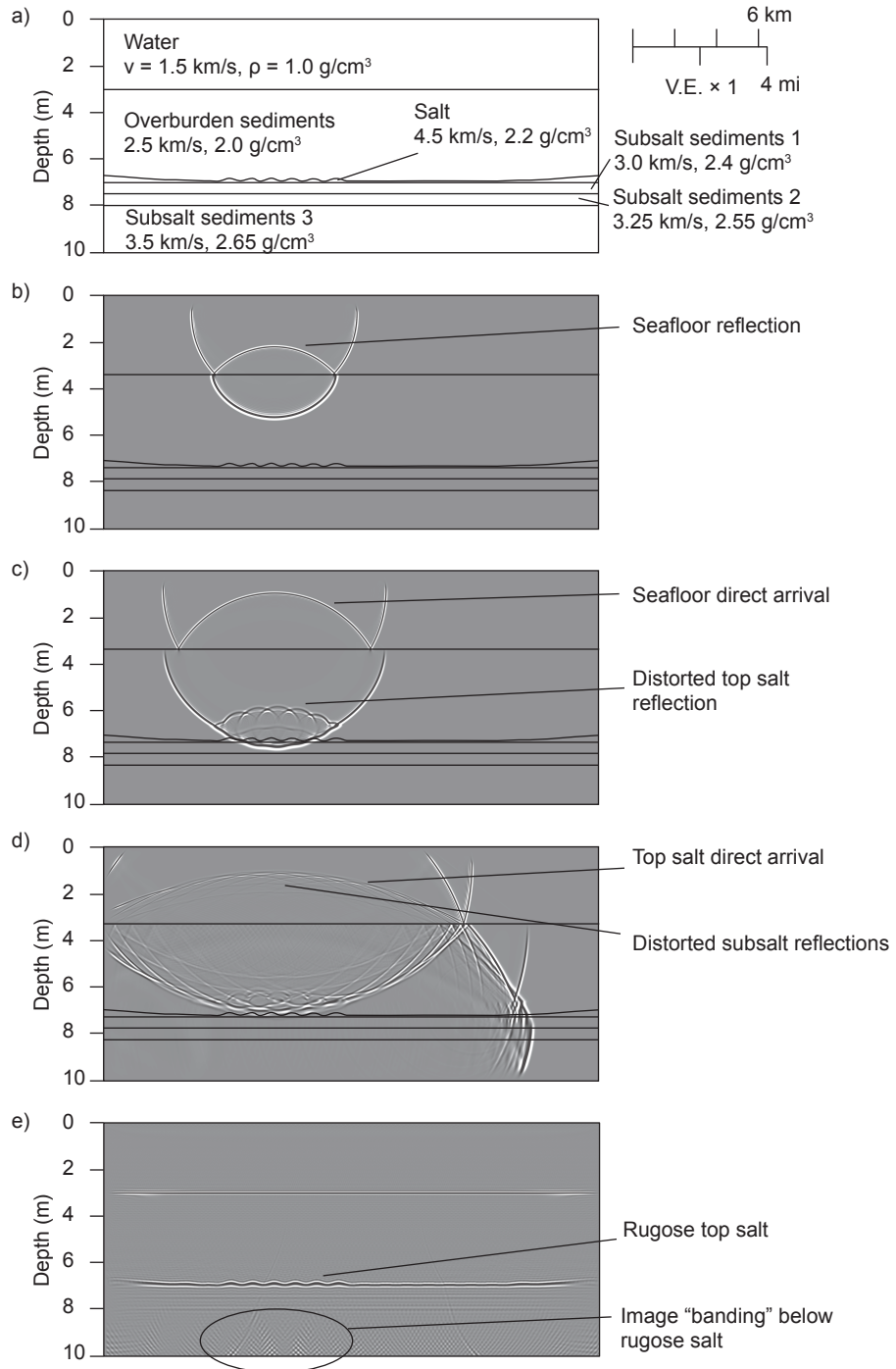


Figure 2.4: Synthetic seismograms illustrating the filtering and scattering effects of evaporite welds. a) Geometry and parameters used to create synthetic seismogram. Salt having a folded upper contact (see Figure 2.3a) is sandwiched between sediments. Survey acquisition parameters approximate modern marine seismic surveys, and all densities and P-wave velocities are typical of the Campos Basin, offshore Brazil. b) Snapshot of wavefield at time  $t = 3.5$  s illustrating reflection from the seafloor. c) Wavefield at  $t = 5.5$  s. The source wave is reflected from and distorted by tightly spaced folds on the top of salt. d) Wavefield at  $t = 7.5$  s. The distorted reflection from the top of salt arrives at receivers at the sea surface, followed closely by distorted subsalt reflectors. e) Final migrated image. Image quality is degraded below folded salt due to scattering caused by the folds. This image was migrated using source-receiver functions and represents the optimum migrated image. Real seismic images are increasingly degraded below welds and structurally complex salt. Synthetic seismograms were produced using Madagascar, an open source mathematics package designed for massively parallel multidimensional data analysis and reproducible computational experiments. For more information, visit [www.ahay.org](http://www.ahay.org).



Giant evaporite deposits are formed by evaporating enormous volumes of seawater in a restricted environment, such as a barred rift basin (Walker, 1984) and evaporite deposition ends by the time rifting evolves into passive margin conditions (Warren 2010). *Autochthonous* evaporites are in stratigraphic continuity with their surroundings (Jackson and Talbot, 1991). As a result, the rocks below autochthonous salt were likely deposited in a syn-rift, marginal marine depositional setting or may even be deposited directly on crystalline basement. For example, evaporites in the Lagoa Feia Formation, Campos Basin, offshore Brazil, are underlain in places by lacustrine shales, coquina carbonate banks, rift-basin alluvial fans, and bald igneous basement highs (e.g., Mohriak et al., 1995; Guardado et al., 1999; Meisling et al., 2001). Autochthonous evaporites can be overlain by a variety of lithologies, including marginal marine carbonates, such as the Albian Macae in offshore Brazil (Carozzi et al., 1979), or even by continental deposits, such the Norphlet dune field in the eastern Gulf of Mexico (McBride et al., 1987).

When subjected to a differential load, evaporites creep over geologic time. Rock salt is approximately two orders of magnitude less viscous than anhydrite under similar deformation conditions (Zulauf et al., 2009) and can flow hundreds of kilometers laterally and tens of kilometers vertically to form the wide variety of structures associated with salt tectonics (e.g., Trusheim, 1960; Worrall and Snelson, 1989; Hudec and Jackson, 2004). *Allochthonous* evaporites, which are

emplaced above stratigraphically younger rocks, can be juxtaposed against other lithologies with varying seismic properties (expanded definition by Hudec and Jackson, 2006). Elevated pore fluid pressures (e.g., House and Pritchett, 1995) and weak formation integrity (e.g., Niemann, 1997) have been described in rocks immediately below salt in wells in the Gulf of Mexico, suggesting sheet advance may inhibit subsalt lithification.

Once salt is deposited or emplaced, the lithology of the encasing sediments and the extent to which they have been buried or lithified control the acoustic impedance contrast between evaporites and the surrounding rocks. As the acoustic impedance of the surrounding rocks rise, evaporites that are normally easy to identify can be notoriously difficult to interpret. Igneous rocks, which can intrude or erupt before, during, or after evaporite deposition or allochthonous sheet emplacement, are notable exceptions to these generalizations, but are typically easy to identify based on their high amplitude, discordant morphology, and proximity to documented magmatism (e.g., Pequeno, 2009).

Although the lithologies above and below evaporites can vary, many laboratory and field observations have identified ranges of seismic properties for common lithologies (e.g., Birch, 1966; Gardner et al., 1974). To study the reflective character of evaporite welds, it is instructive to convert these results to reflection coefficients for the upper and lower contacts of an evaporite bed (Figure 2.5).

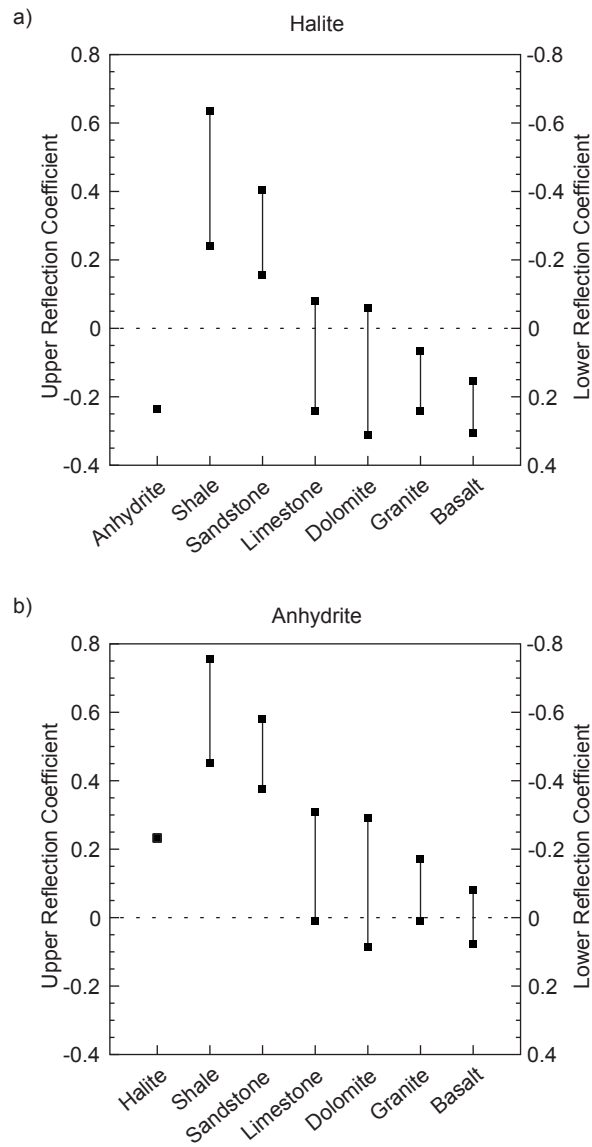


Figure 2.5: Reflection coefficients between common lithologies and a) halite and b) anhydrite beds. The upper halite reflection may vary from positive, in contact with shallowly buried siliclastics, to strongly negative, in contact with carbonates or igneous rocks. In contrast, the upper reflection of an anhydrite bed is positive for most lithologies encountered in the shallow subsurface. Data from Bourbié et al. (1987).

## EVAPORITE WELDS AS THIN BEDS

Seismic-wavelet propagation through a three layer inverted wedge model of the subsurface was used to resolve thin evaporites in a subhorizontal evaporite weld (Figure 2.6). This model has three primary variables: 1) the reflection coefficient of the upper evaporite contact ( $R_1$ ), 2) the reflection coefficient at the lower evaporite contact ( $R_2$ ), and 3) the thickness of the evaporites ( $h$ ). These variables lend themselves to four types of thin beds (in this case, types of welds), which were classified by Sun et al. (2009) as follows:

Type I: Equal Reflection Magnitude, Opposite Polarity

(e.g., anhydrite between identical mudstones)

Type II: Equal Reflection Magnitude, Identical Polarity

(e.g., halite between sandstone and dolomite)

Type III: Unequal Reflection Magnitude, Identical Polarity

(e.g., halite between overpressured shale and limestone)

Type IV: Unequal Reflection Magnitude, Opposite Polarity

(e.g., anhydrite between shale and limestone)

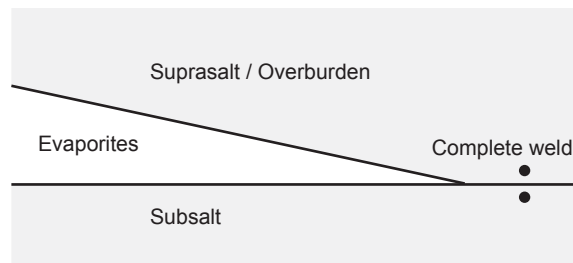


Figure 2.6: Wedge model used to approximate evaporite welds and produce synthetic seismograms.

To investigate these four weld types, inverted wedge models composed of synthetic traces were based on ideal prototypes and natural welds. In each example, a zero-phase Ricker wavelet is convolved with a reflection series corresponding to the top and base of an evaporite wedge then interpreted like a seismogram to illustrate concepts of vertical seismic resolution as they relate to thin evaporites. Reflection magnitude and polarity are calculated by determining the reflection coefficient, which in turn is controlled by the acoustic impedance contrast of the evaporites and the surrounding rocks. A positive reflection coefficient corresponds to a positive polarity reflection. To begin, consider the two ideal cases of a Type I and a Type II weld, which were first examined in detail by Kallweit and Wood (1982).

### **Type I Welds (Equal Magnitude, Opposite Polarity)**

Consider an ideal Type I weld composed of a thin evaporite encased in an otherwise homogeneous medium with these reflection coefficients:  $R_1 = 0.5$  and  $R_2 = -0.5$  (Figure 2.7a). Where evaporites are thicker than the breadth of the synthetic wavelet, separate positive and negative polarity reflections correspond to their top and base. As the evaporite thins, the upper and lower reflections constructively interfere. The peak amplitude of the reflected wavelet complex increases to a maximum at the tuning thickness, which is defined as one-half the wavelet breadth. As the evaporite thins further, the reflections destructively

interfere, and the amplitude approaches zero for a complete weld. Amplitude variation with evaporite thickness is plotted for various wavelet peak frequencies in Figure 2.7b.

To the interpreter, apparent thickness ( $a$ ), that is the time difference between the positive upper reflection and the negative lower reflection, is identical to true thickness ( $t$ ) as long as the evaporite is slightly thicker than the wavelet breadth (Figure 2.7c). Below this thickness, the ratio of apparent thickness to true thickness first decreases ( $h > a$ ), then increases to unity at the tuning thickness ( $h = a$ ), and continues to increase ( $h < a$ ) as it approaches the temporal resolution ( $T_R$ ) of the data. If the remnant evaporites are thinner than this temporal resolution, the weld will appear thicker than it really is.

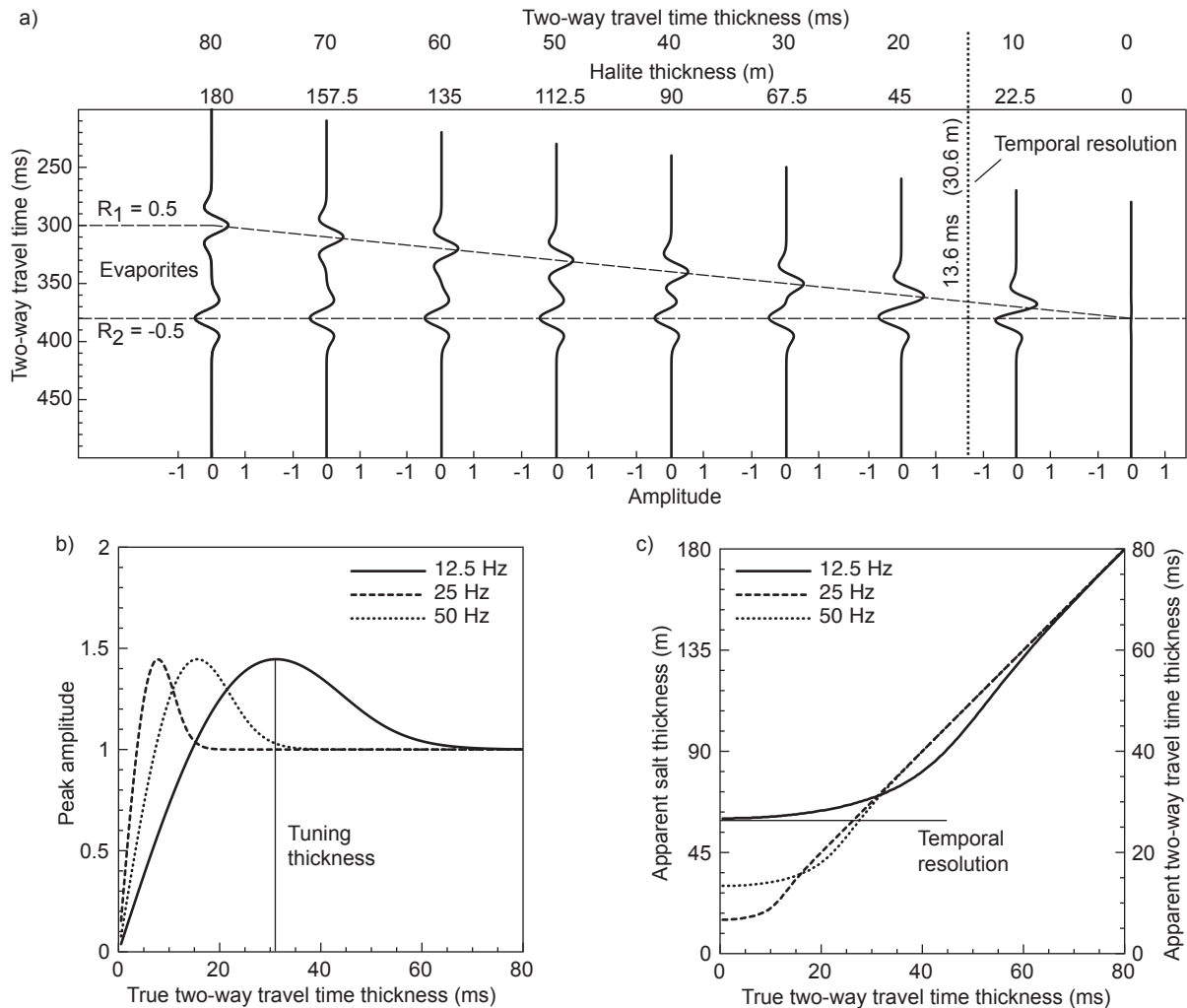


Figure 2.7: a) Synthetic seismic traces generated using a zero-phase Ricker waver with peak frequency 25 Hz. In a Type I weld, the upper and lower evaporite reflections have equal magnitude and opposite polarity. As the evaporite wedge thins into a weld, the upper and lower reflections interfere to produce a complex wavelet. Below the temporal resolution of the wavelet (13.6 ms or 30.6 m of salt), it is impossible to determine bed thickness using travel-time differences alone. For a complete weld, no reflection is produced. b) Peak amplitude versus true two-way travel-time (twtt) thickness in ms for a wavelet of variable peak frequency. Peak amplitude increases to a maximum at the tuning thickness, one half the breadth of the wavelet, and then decreases to zero for a complete weld. c) True twtt versus apparent twtt thickness, the time difference between the peak of the upper reflection and the peak of the lower reflection, for a wavelet of variable peak frequency. Apparent twtt thickness tends to the temporal resolution as true thickness tends to zero. Evaporites thinner than temporal resolution will produce a peak-trough doublet that is impossible to interpret accurately. As previously noted, an increase in frequency increases the resolving power of a seismic-wavelet.

## Type II Welds (Equal Magnitude, Equal Polarity)

Now consider an ideal Type II weld with  $R_1 = 0.5$  and  $R_2 = 0.5$  (Figure 2.8a). Again, separate reflections are observed when  $h > b$ . As the evaporite thins, the upper and lower reflections destructively interfere and the peak amplitude of the reflected wavelet complex decreases to a minimum at the tuning thickness. Below this thickness, the reflections begin to constructively interfere and the peak amplitude of the wavelet complex approaches the sum of the individual reflection amplitudes for a complete weld. Amplitude variation with evaporite thickness is plotted for various wavelet peak frequencies in Figure 2.8b.

In this example, apparent thickness is the time difference between the converging peaks of the composite wavelet and is again equal to true thickness for a weld somewhat thicker than wavelet breadth (Figure 2.8c). Below this thickness, the ratio of apparent thickness to true thickness increases ( $h < a$ ), then decreases to unity at the tuning thickness ( $h = a = b/2$ ), and continues to decrease ( $h > a$ ) as it approaches the temporal resolution of the data. If the evaporite weld is thinner than this temporal resolution, only one reflection appears on the seismic data.

For both Type I and Type II welds and a zero-phase Ricker wavelet having a peak frequency of 25 Hz, the temporal resolution calculated using the equation of Kallweit and Wood (1982) is approximately 13.3 ms. Thus, it is impossible to resolve a halite-rich weld less than about 30 m thick or an anhydrite-rich weld less than about 36 m thick using travel-time differences alone.

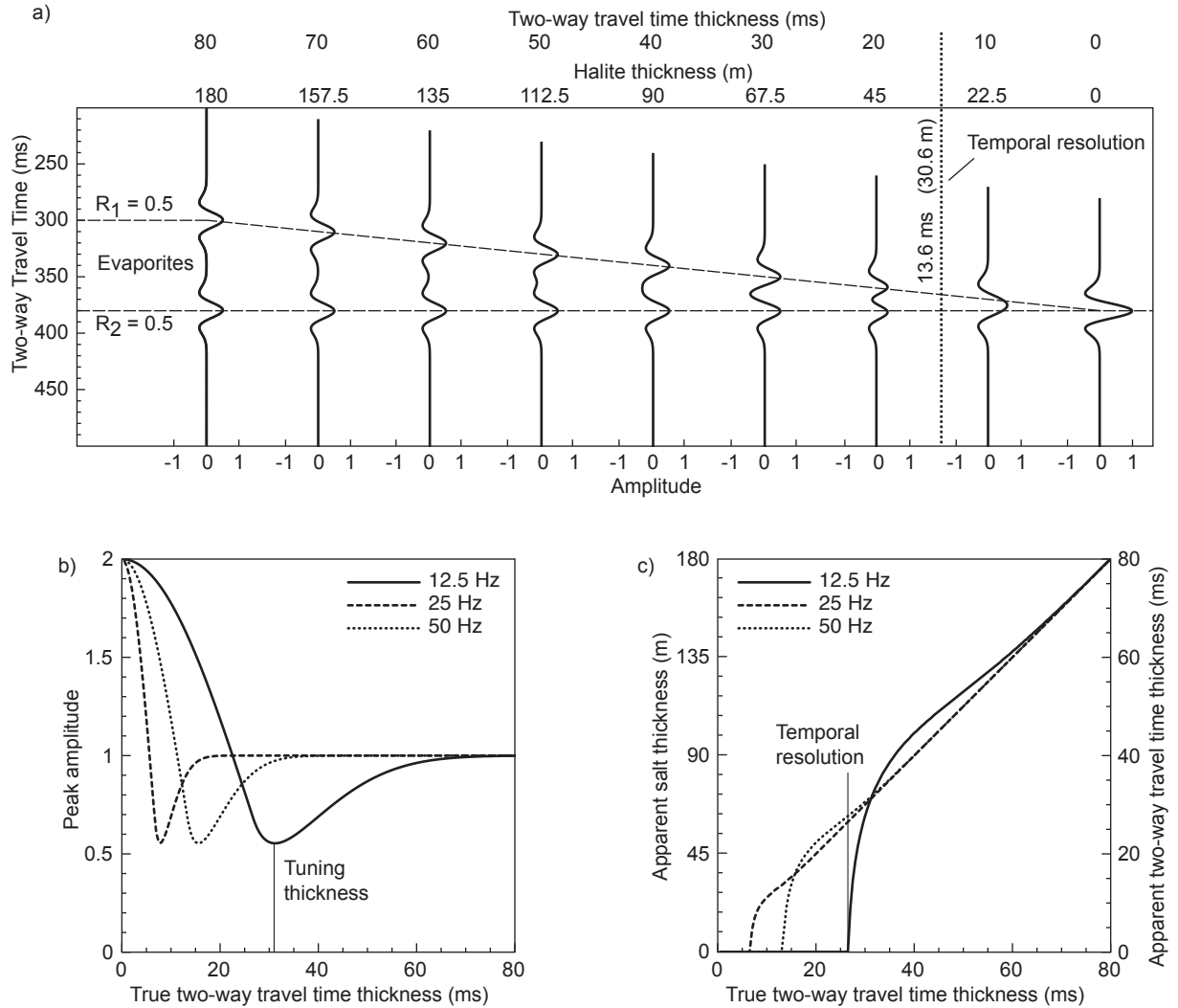


Figure 2.8: a) Synthetic seismic traces for a Type II weld in which the upper and lower reflections are of identical magnitude and polarity. As evaporites thin into the weld, the upper and lower reflections interfere to produce a single peak corresponding to a complete weld. b) Peak amplitude versus true twtt for various peak frequencies. Peak amplitude decreases to a minimum at the tuning thickness and then increases to the sum of the upper and lower reflection coefficients for a complete weld. c) True twtt versus apparent twtt, the peak to peak travel-time for various peak frequencies. Apparent twtt tends to zero even as the true twtt approaches temporal resolution.

### **Type III Welds (Unequal Magnitude, Equal Polarity)**

The model Type III weld has  $R_1 = 0.5$  and  $R_2 = 0.25$  (Figure 2.9a). As the evaporite wedge thins, the peak amplitude behaves like the Type II weld (Figure 2.9b). However, interpreting the true thickness of the weld is more complicated (Figure 2.9c). In this example, the primary peak of the lower reflection destructively interferes with the lower side lobe of the upper reflection and is only detectable down to near the tuning frequency. Below this thickness, the reflected wavelet complex consists of a single upper peak with a widened trailing side lobe. As the reflection coefficient ratio ( $R_1/R_2$ ) increases, the thickness at which only one peak is detected also increases, which in turn reduces temporal resolution (Figure 2.9d). When  $R_1/R_2 = 4$ , temporal resolution is reduced by 15%. When  $R_1/R_2 = 8$ , temporal resolution is reduced by nearly 40%. However, because wavelet interference is complex, the effect is nonlinear. For a peak seismic frequency of 12.5 Hz and  $R_1/R_2 = 4$ , an additional 9 m of halite or 11 m of anhydrite is unresolvable over a standard Type II weld.

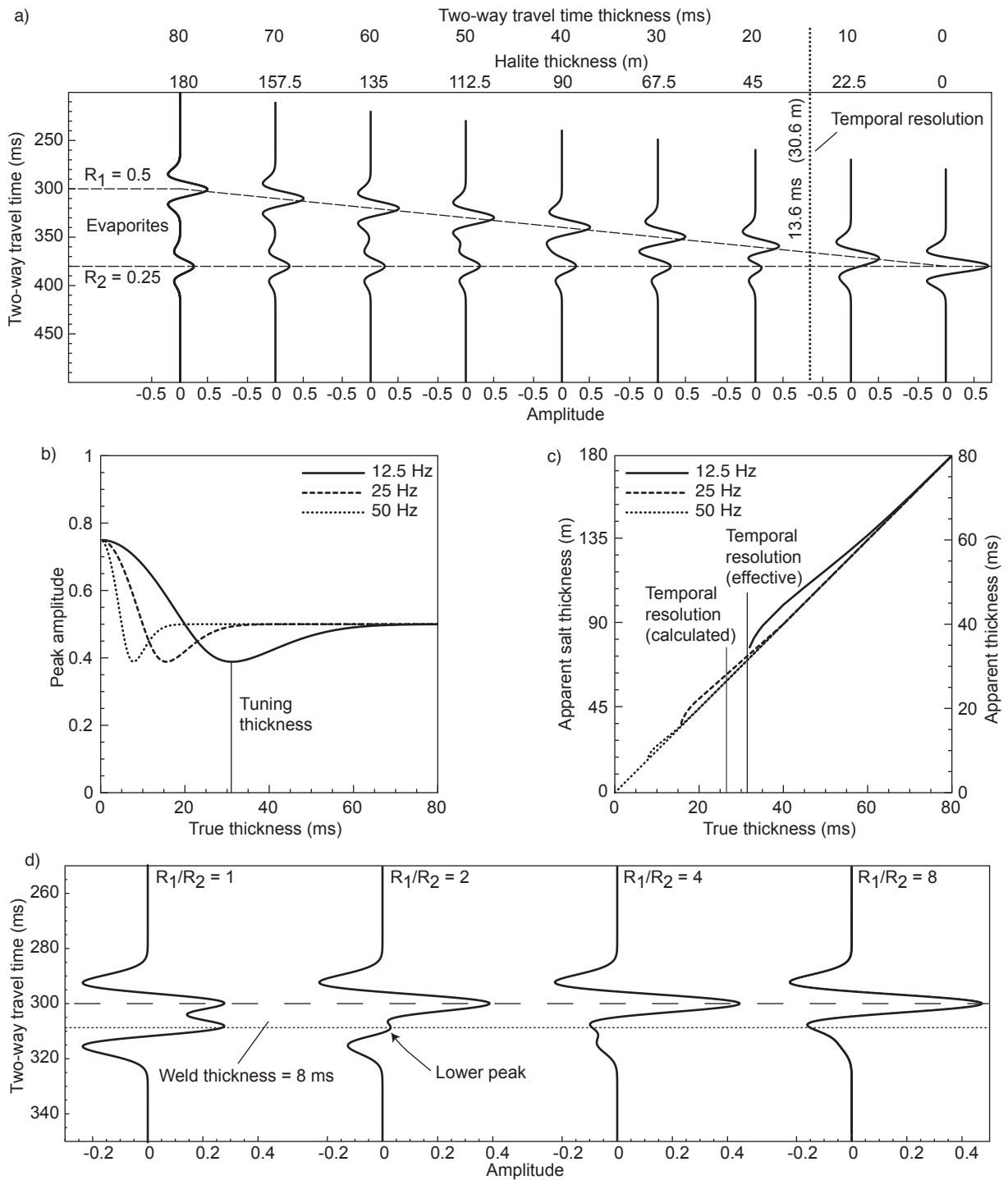


Figure 2.9: a) Synthetic seismic traces for a Type III weld in which the upper and lower reflections have different magnitude but identical polarity. The composite reflection is similar to a Type II weld. Peak amplitude (b) and apparent twtt (c) versus true twtt are also similar to Type II welds where the reflection coefficient ratio is small. d) As the reflection coefficient ratio increases, sidelobe interference masks the smaller reflection, decreasing temporal resolution.

### **Type IV Welds (Unequal Magnitude, Opposite Polarity)**

The model Type IV weld has  $R_1 = 0.5$  and  $R_2 = -0.25$  (Figure 2.10a) and the amplitude behaves like the Type I weld (Figure 2.10b), with one exception; below tuning thickness the peak amplitude approaches the sum of the individual reflection amplitudes. Apparent thickness behaves similarly to the Type I weld as well, except that it decreases rapidly ( $h \gg a$ ) very near zero true thickness as the wavelet complex evolves into a single reflection where evaporite thickness is zero. For Type IV welds, picking the smaller reflection becomes increasingly difficult with increasing reflection coefficient ratio (Figure 2.10c) because it is obscured by the trailing side lobe of the larger reflection.

With few exceptions, reflections on the top and base of evaporites are of different magnitude and opposite polarity, making Type III and Type IV beds better analogs to many real welds. Furthermore, given the high acoustic impedance of evaporites with respect to other lithologies, it is not surprising Type II and Type III welds are rare in the shallow subsurface, especially in partial welds containing anhydrite. Armed with this information, three examples typical of evaporite welds on reflection-seismic data in the Gulf of Mexico and the Campos Basin, offshore Brazil were examined.

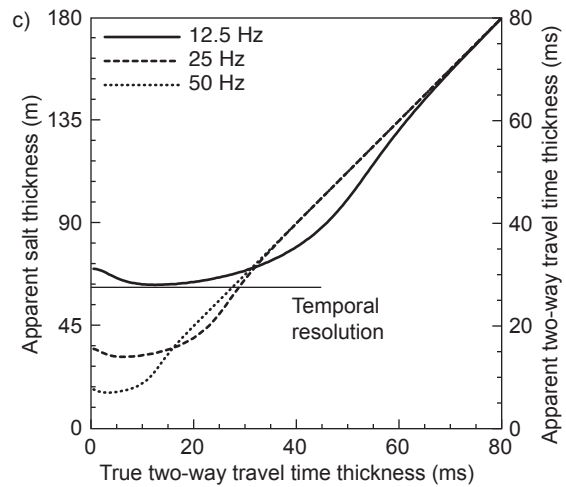
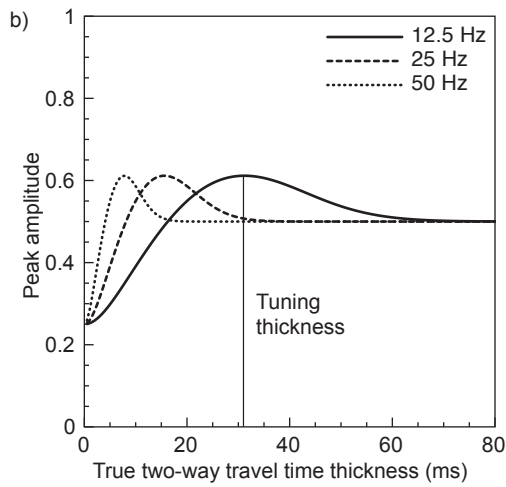
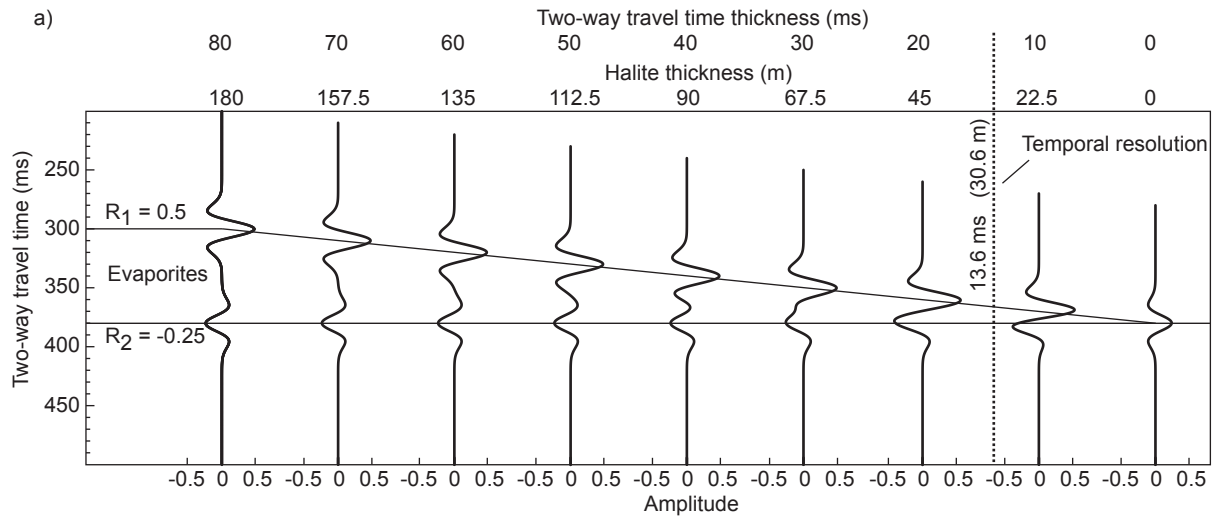


Figure 2.10: a) Synthetic seismic traces for a Type IV weld in which the upper and lower reflections have different magnitude and opposite polarity. The composite reflection is similar to a Type I weld. Peak amplitude (b) and apparent twtt (c) are also similar to Type I welds.

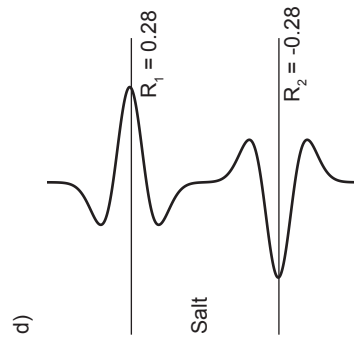
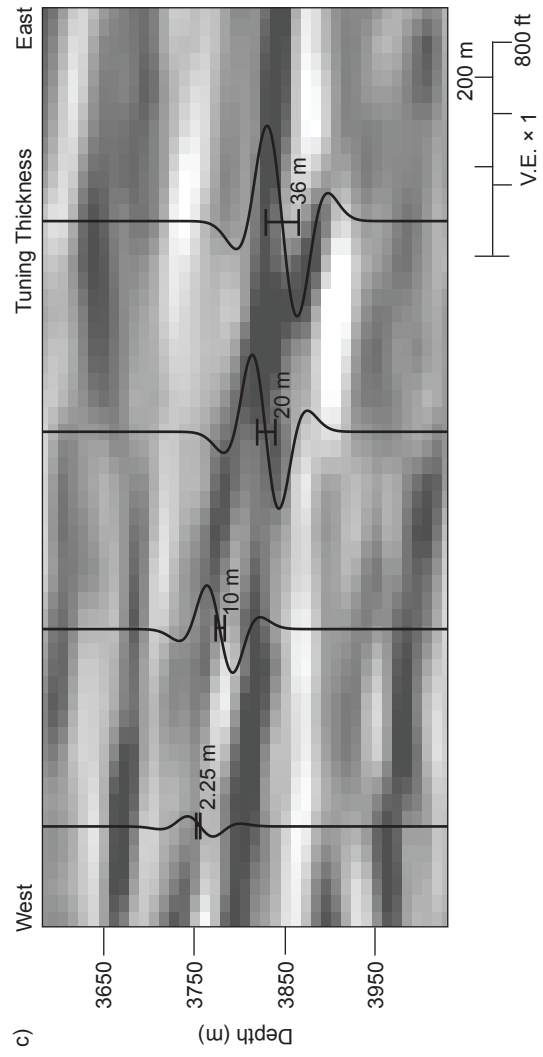
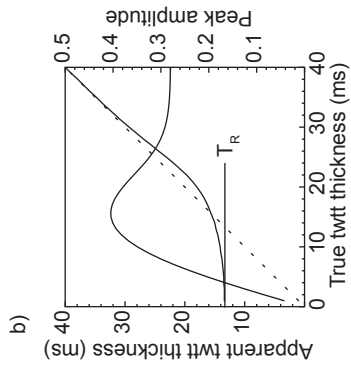
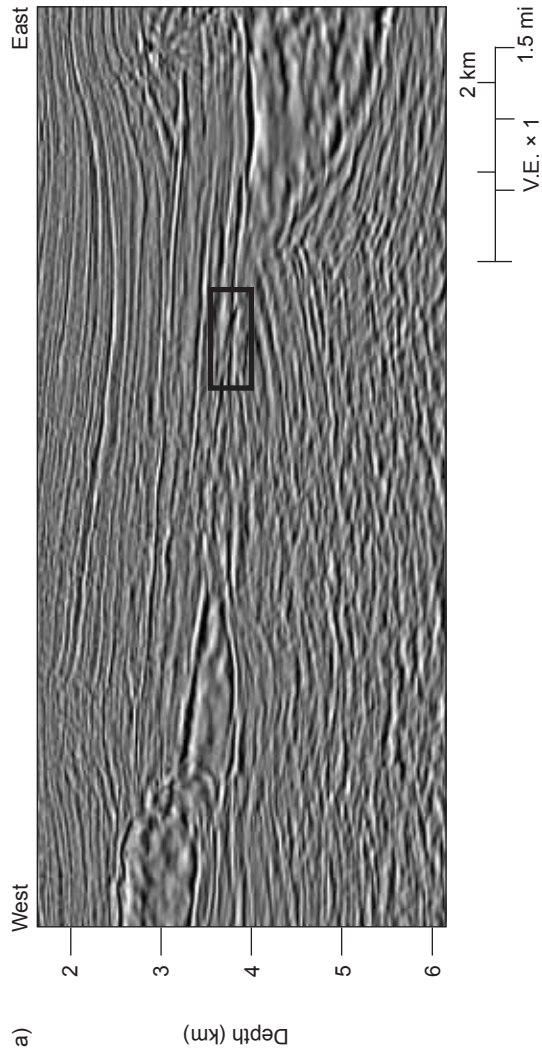
## ESTIMATING EVAPORITE THICKNESS

First, consider a Type I weld containing remnant halite on pre-stack depth-migrated (PSDM) data from the Gulf of Mexico shelf (Figure 2.11). In depth-converted seismic data, weld thicknesses can be explicitly decided prior to depth migration by building a velocity model. Any errors or biases fed into the migration workflow (or in a velocity model for traditional depth-converted data) persist in the final migrated product. Furthermore, automatic gain control (AGC) is commonly used to aid interpretation by normalizing reflection amplitudes throughout a given seismic trace. AGC can obscure the real amplitude information needed to estimate remnant evaporite thickness. Where available, data that has not been processed with AGC should be used. Alternatively, an impedance section generated through seismic inversion can be used to characterize the upper and lower reflections of evaporites just outside of the weld. Here, the data have been properly processed and analyzed such that the following analysis is valid.

In this first example, the reflection from the top of allochthonous salt is strongly positive, which is typical of shallowly buried allochthonous salt in the Gulf of Mexico. Just outside the weld, the base of salt has a strongly negative reflection, suggesting the suprasalt and subsalt rocks have similar seismic properties. No one reflection can be easily mapped across the weld, so travel-time interpretation is unable to estimate of salt thickness. Peak frequency in this example is approximately 25 Hz, and the amplitude of the top and base salt

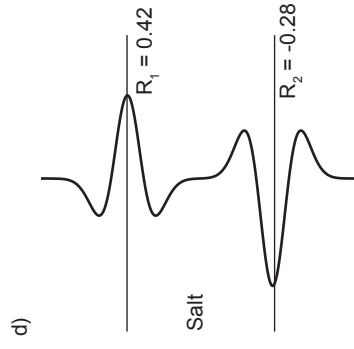
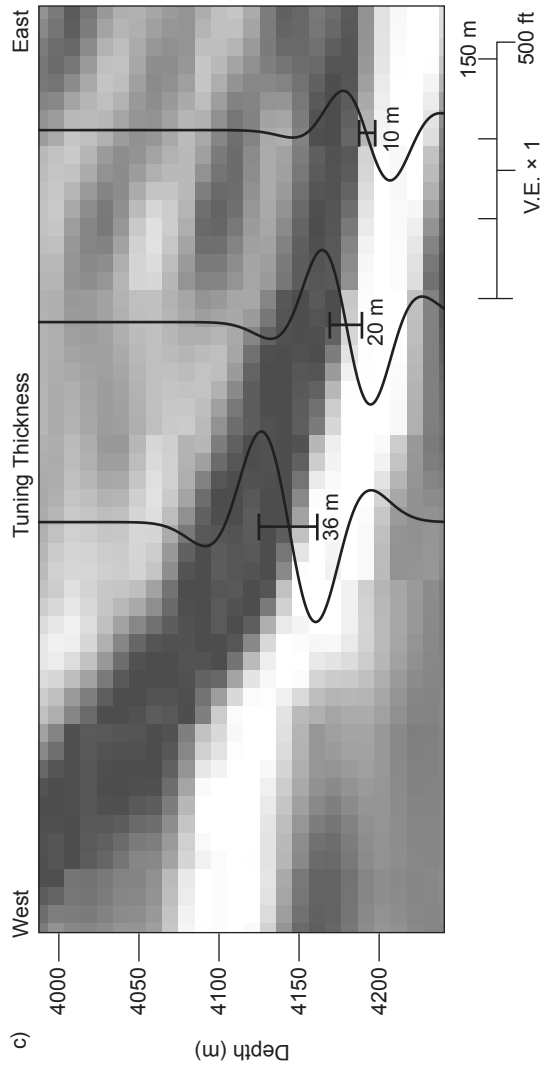
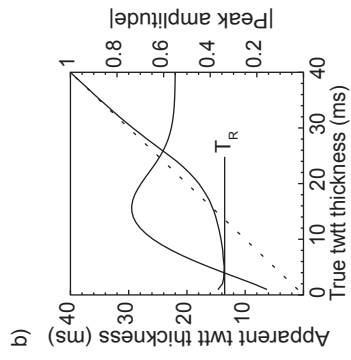
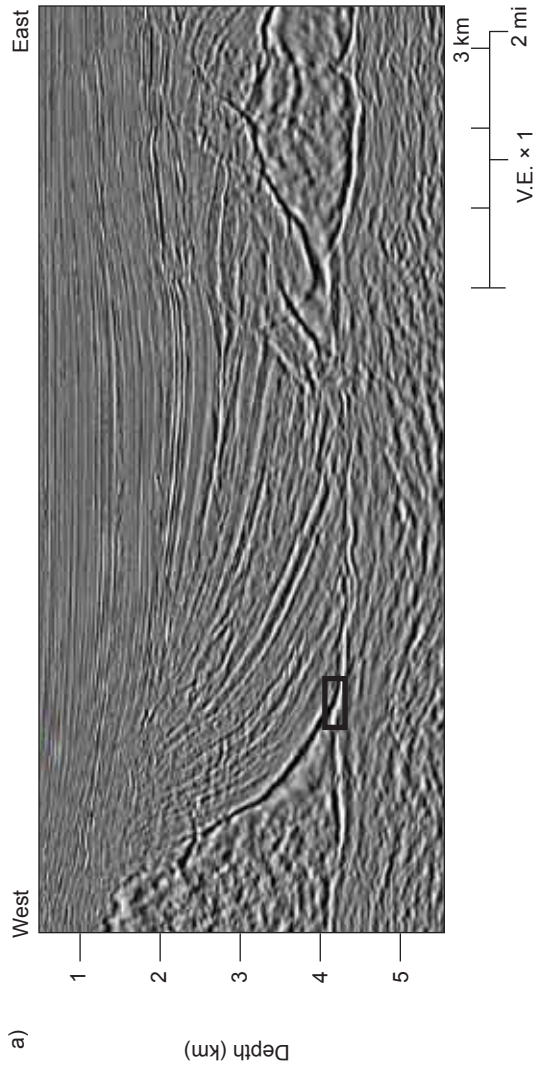
reflections near the weld is substantially smaller than those outside the weld. Thus, any remnant salt is also thinner than the tuning thickness. Salt in this weld is certainly thinner than 20 m, is probably thinner than 10 m thick, and may even be completely absent in places. Alternatively, variations in evaporite lithology due to the presence of inclusions or dissolution-derived residue may cause the observed amplitude variations. For example, halite may have been preferentially removed by viscous flow and dissolution during welding, leaving behind slow, low-density lithologies, such as gypsum, to produce a low-amplitude weld reflection.

Figure 2.11: a) Prestack depth-migrated seismic section illustrating a Type I halite weld in the Gulf of Mexico. The weld itself is not clearly imaged. b) For this Type I weld, peak amplitude is expected to increase to a maximum at the tuning thickness and then decrease as evaporite thickness tends to zero (Figure 2.8). Given a peak frequency of 25 Hz, the temporal resolution of the data is approximately 13.6 ms (30.6 m of halite). c) Detailed view of the area outlined by the box in (a). Comparing amplitudes in the seismic section with synthetic seismic traces indicates that any residual halite must be thin and perhaps absent. d) Reflection coefficients used to produce the synthetic traces.



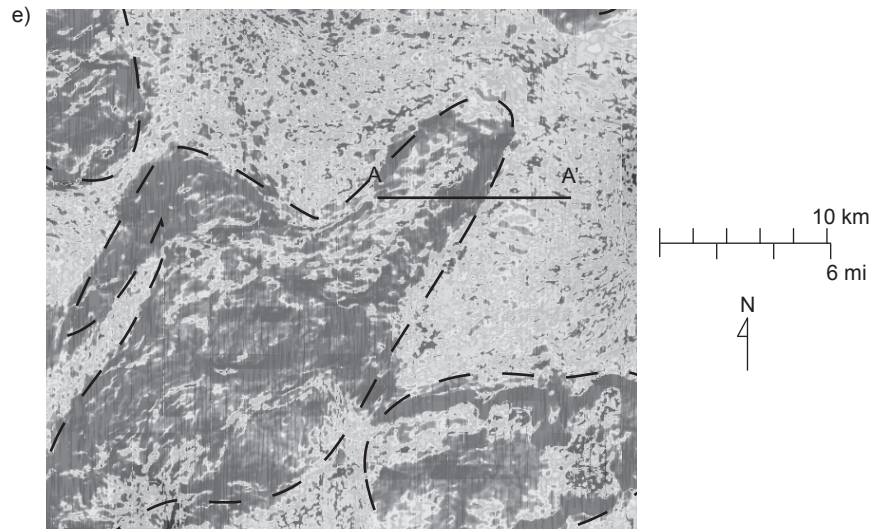
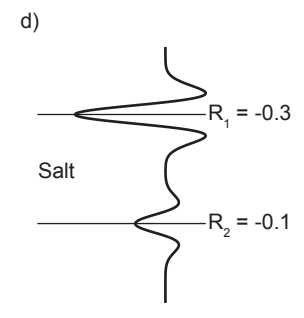
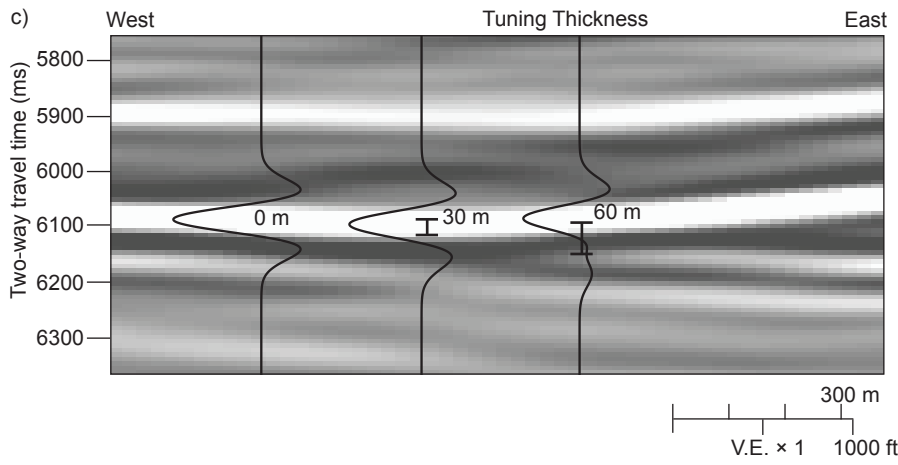
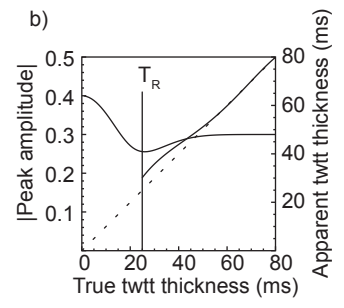
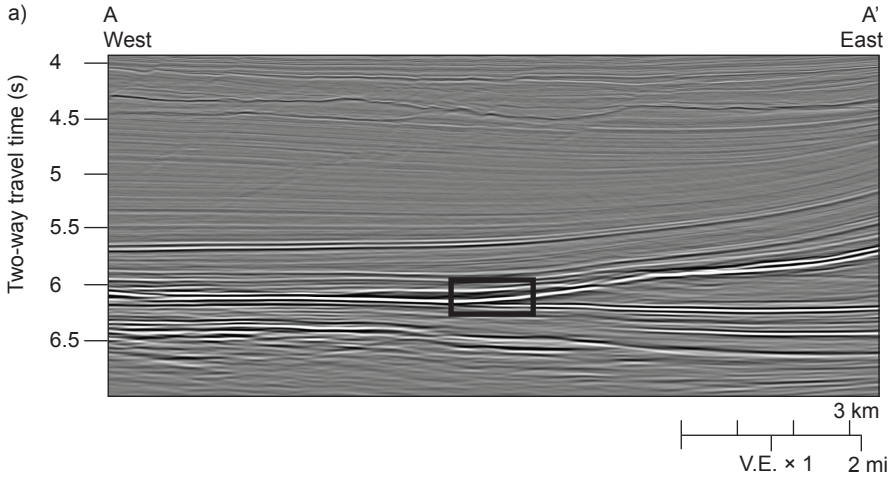
Next, consider a Type IV weld containing remnant halite on PSDM data from the Gulf of Mexico shelf (Figure 2.12). As in the previous example, the reflection on the top of salt is strongly positive. However, the base salt reflection is more strongly negative, as evidenced by a strong sinuous trough along the weld surface that is continuous across the section. Near the center of the weld, the apparent thickness of the weld is 30 ms, which corresponds to an apparent thickness of approximately 13 ms. The amplitude of the through-going trough is more subdued than the base salt reflection away from the weld, suggesting any remnant salt must be somewhat thinner than the tuning thickness and possibly even the temporal resolution of the data. Using a peak frequency of 25 Hz, salt in this weld may be as thick as approximately 25 m or completely absent, if the trough is simply the reflection between the suprasalt and subsalt. Again, slow, low-density lithologies, such as overpressured shale, left behind during welding can explain the decrease in reflection amplitude along the weld.

Figure 2.12: a) Prestack depth-migrated seismic section illustrating a Type IV halite weld in the Gulf of Mexico. The weld is characterized by a through-going trough that appears to correspond to the base of salt outside the weld. b) For this Type IV weld, peak amplitude is expected to increase to a maximum at the tuning thickness and then decrease as evaporite thickness tends to zero. Given a peak frequency of 25 Hz, the temporal resolution of the data is approximately 13.6 ms (30.6 m of halite). c) Detailed view of the area outlined by the box in (a). The through-going trough helps constrain our interpretation; most of the weld appears brighter than the reflection that would be produced if salt were absent, though some parts of the weld may be complete. d) Reflection coefficients used to produce the synthetic traces.



Finally, consider a Type III weld containing remnant halite on pre-stack time-migrated (PSTM) data in the central Campos Basin, offshore Brazil (Figure 2.13). Here, salt is overlain by dense, high-velocity carbonates in the Albian Macae Formation, so the resulting top salt reflection is strongly negative. In contrast, the reflection on the base of salt is only weakly negative. As salt thins into the weld, the amplitude of the upper reflection first decreases as it truncates the lower reflection. Nearer the center of the weld, the amplitude of the upper reflection increases by constructive interference with the obscured lower reflection. At the center of the weld, the composite reflection consists of a single strong trough with small positive sidelobes, so it is impossible to estimate salt thickness using travel-time. The lower reflection must be truncated near the temporal resolution, which for a peak frequency of 15 Hz is about 22 ms. However, the lower reflection is prematurely masked by the trailing sidelobe of the upper reflection compared with the ideal case, and the effective temporal resolution is actually about 26.67 ms. Therefore, salt in this example must be less than 60 m thick. Given the increase in amplitude into the center of the weld, salt may also be completely absent. However, the increase in reflection amplitude into the weld can also be explained by the presence of fast, high-density minerals, such as anhydrite, left behind during welding. Once a range is established for possible thickness, amplitude extraction can be used to quickly map the weld in three dimensions (Figure 2.13e).

Figure 2.13: a) Prestack time-migrated seismic section illustrating a Type III halite weld in the Campos Basin, offshore Brazil. The weld has a strong trough that appears to truncate the lower salt reflection. b) Given a peak frequency of 15 Hz, peak amplitude is expected to decrease slightly to a minimum at the tuning thickness and then increase as evaporite thickness tends to zero (Figure 2.10). The temporal resolution of the data is approximately 26 ms (~60 m of halite). c) Detailed view of the area outlined by the box in (a). The point where the lower salt reflection is truncated closely corresponds to the temporal resolution of the data. The amplitude of the strong trough increases into the center of the weld, indicating salt is significantly thinner than the temporal resolution of the data. In some areas, salt may be completely absent. d) Reflection coefficients used to produce the synthetic traces. e) Maximum negative amplitude extraction 6 samples (24 ms) above the base of salt. Dark colors are areas of strongly negative amplitude that correspond to salt less than 60 m thick. Dashed lines represent the 60 m isochore calculated between the top and base of salt.



## CONCLUSIONS AND RECOMMENDATIONS

Evaporite welds produce composite reflections that can be classified as one of four types of thin beds based on the reflection coefficients of the evaporite contacts. Below the temporal resolution of the seismic data, typically ~25-50 m for modern surveys with peak frequencies of ~10-30 Hz, partial welds (those containing remnant salt) and complete welds (those devoid of salt) are indistinguishable based on travel time differences alone. Instead, synthetic seismograms can be used to track variations in apparent thickness and amplitude of seismic welds to estimate true evaporite thickness. Natural examples further constrain the variable seismic character of welds and their surroundings. These first-order estimates of evaporite thickness can be used to guide interpretation efforts and can be improved using modern seismic attribute analyses. Accordingly, the following guidelines for interpreting salt welds are proposed:

- 1) Classify the evaporite weld by determining the reflection coefficients of the upper and lower evaporite contacts adjacent to the welded area. Based on typical seismic properties of evaporites and their surroundings, Type IV and Type I welds are more common than Type II and Type III welds, especially for welds containing anhydrite. Resolving power can be reduced by ~40% for Type III welds with reflection coefficient ratios greater than 4.

2) Identify the peak frequency of the seismic data and use synthetic seismograms to determine the possible variations in amplitude and apparent thickness with true thickness (as in Figure 2.7b-c). These variations are straightforward for Type I and Type II welds and more complicated for Type III and Type IV welds.

3) Compare variations in apparent thickness and amplitude on the seismic data with the results from synthetics to estimate weld thickness case-by-case. Ensure migration and AGC biases have been eliminated or minimized when performing this analysis. In general, if amplitude varies only slightly across the weld, evaporite thickness is likely greater than the temporal resolution of the data; thus apparent thickness can be used to estimate true thickness. If the amplitude varies greatly across the weld or the weld reflection is difficult to distinguish, evaporite thickness may be below the temporal resolution of the data. Estimate evaporite thickness using a combination of amplitude and apparent thickness. Where possible, calibrate estimates using well data and synthetic seismograms.

## **ACKNOWLEDGEMENTS**

I thank Martin Jackson, Mike Hudec, Mark Cloos, Mrinal Sen, and Ron Steel at the Jackson School of Geosciences and Frank Peel at BHP Billiton for comments and reviews. Seismic data provided courtesy of Petroleum Geo-Services. Technical support was provided by Reuben Reyes and Dallas Dunlap, and Madagascar support was provided by Will Burnet. This research was funded by the Jackson School of Geosciences and the Applied Geodynamics Laboratory, a salt tectonics research consortium at the school's Bureau of Economic Geology.

## CHAPTER 3: SALT WELDS, DISSOLUTION, AND HYDROCARBON MIGRATION

### ABSTRACT

Because salt welds can act as pathways or barriers to subsurface fluid flow, predicting which welds seal and which ones leak is crucially important to understanding cross-weld migration of hydrocarbons and mineralizing waters. Fluid flow through and near salt welds is enhanced by dissolution and the development of microstructural permeability in salt. Within a few kilometers of the surface, infiltration of meteoric waters can rapidly dissolve salt. Hydrodynamic considerations suggest the migration of large volumes of dissolving fluids undersaturated with salt is less likely at depths  $> 1$  km and dissolution is slow, dissolving up to a few meters of salt per million years based on analytical models. Intact salt can seal hydrocarbon columns taller than  $\sim 500$  m so the tendency of partial welds to leak is controlled by the continuity of any remnant evaporites. The tendency of thin ( $< 100$  m) evaporites to seal or leak is further influenced by mesoscale structures such as faults with or without gouge, extension fractures, and lithology within and surrounding the evaporites that can be difficult to predict on geophysical data. Empirical evidence from well and seismic data indicates the tendency of a salt welds to seal can be predicted by examining weld area and remnant evaporite thickness: partial welds in the

Campos Basin, offshore Brazil, that are greater than  $\sim 25 \text{ km}^2$  in area and contain remnant evaporites thinner than  $\sim 50 \text{ m}$  have served as pathways for migrating hydrocarbons.

## INTRODUCTION

A salt weld forms where salt and other evaporites are removed by viscous flow and dissolution. Following common usage, the term *salt* is used to refer to any rock composed primarily of halite and capable of ductile flow at low temperatures and strain rates. Salt welds were first named and classified by Jackson and Cramez (1989) based on seismic data in the Gulf of Mexico, but the concept of vanished salt was already known by other names, such as “evacuation surface,” or “cicatrice salifère” (literally, salt scar) (e.g., Burolet, 1975). Welds can form wherever salt deforms and have been identified or described in most major evaporite basins. Salt welds are commonly described in the literature, but in many ways the process of welding and the physical properties of welds remain a mystery.

Two main processes are known to remove salt to form welds: 1) viscous flow and 2) dissolution. In Chapter 1, I concluded viscous evacuation alone can never remove all salt because of boundary drag along the edges of the mobile layer. This is especially true where salt flow is restricted by geometry, such as salt evacuation beneath a prograding sediment wedge, where up to  $\sim 50 \text{ m}$  of salt

can remain even on geologic time scales. Where salt flow is unrestricted, such as beneath a subsiding minibasin, or where layer-parallel wall rock translation occurs, all but a vanishingly thin ( $\ll 1$  m) veneer of salt can remain. Accordingly, a weld that contains up to ~50 m of remnant salt is called a *partial weld*. A weld that contains no remnant salt is called a *complete weld*. Salt remaining in a partial weld after viscous evacuation and layer-parallel wall rock displacement can be removed by dissolution to form a complete weld. However, the contribution of dissolution to welding has not been quantified.

Salt welds can act as either barriers or pathways for subsurface fluid flow (e.g., Guardado et al., 2000; Rowan, 2004) and are especially important to petroleum exploration (Figure 3.1). Hydrocarbons generated in subsalt or presalt source rocks flow through permeable salt welds (known colloquially as "salt windows") to charge suprasalt reservoirs on the Gulf of Mexico shelf and slope (e.g., McBride et al., 1998) and in the Campos Basin, offshore Brazil (e.g., Guardado et al., 2000). In contrast, recent subsalt exploration targets in the Gulf of Mexico (e.g., Kaskida, Keathley Canyon Block 292/291) and in the Campos Basin (e.g., Wahoo, BMC-30) rely on partial welds to seal large volumes of hydrocarbons (> 400 mmboe recoverable reserves). In light of this contrasting behavior of salt welds, predicting which welds seal or leak in the subsurface is critical to exploration efforts. Rowan (2004) suggested weld permeability is controlled in part by remnant evaporites or shale gouge produced by shear

displacement along the weld, by the permeability of the wall rocks, and by the availability of migration pathways within and surrounding the weld. For example, fluids are unlikely to migrate across a weld encased in unfractured shale, even if the weld itself is permeable. Furthermore, these features may be below seismic resolution and thus difficult to predict using reflection seismic profiles prior to drilling.

To improve our understanding of fluid flow through welds, concepts of fluid flow near and through salt in the subsurface are reviewed to quantify the effects of dissolution. Next, the relationship between the tendency for welds to seal or leak and the physical properties and structure of salt welds is discussed. Finally, an integrated dataset comprised of three-dimensional seismic and well data was used to examine the effect of weld geometry on hydrocarbon migration through partial welds in the Campos Basin.

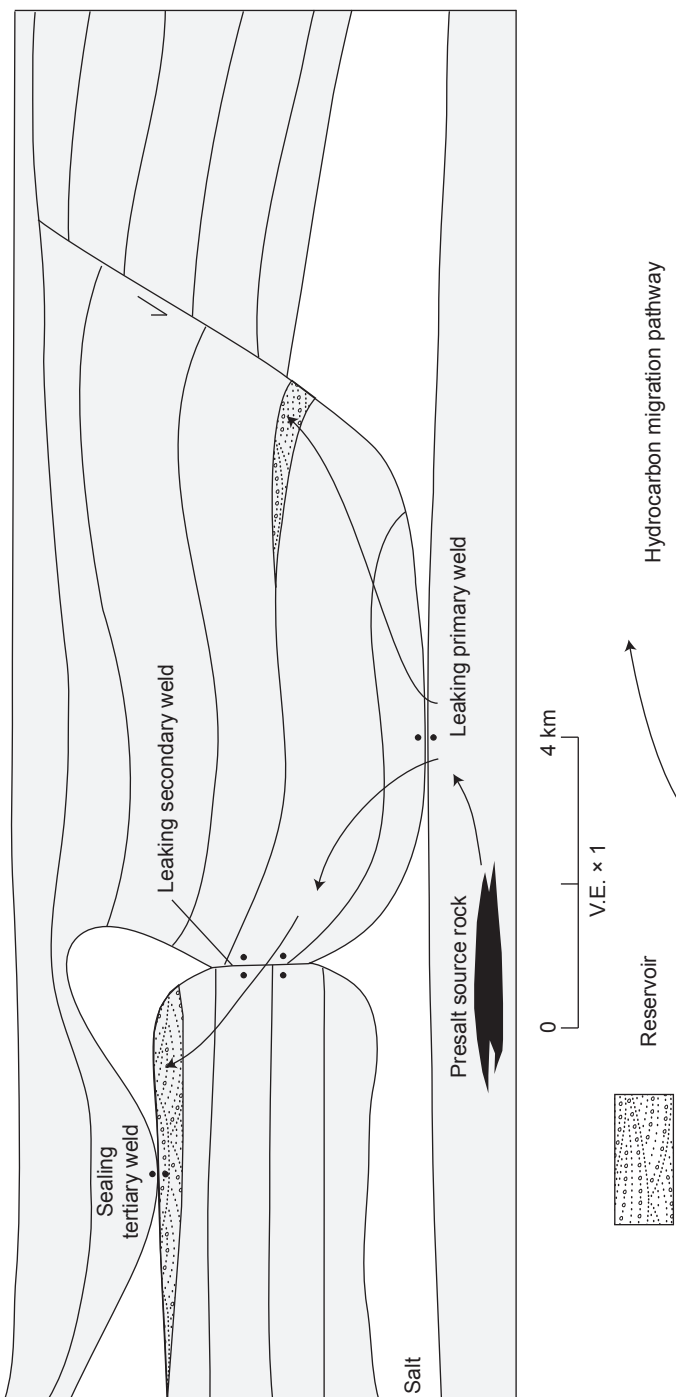


Figure 3.1: Salt welds can act as barriers or pathways for migrating hydrocarbons or mineralizing fluids. In this schematic hypothetical cross section, hydrocarbons generated in a presalt source migrate through a leaking primary weld into the overburden. Hydrocarbons continue to flow upward, through a leaking secondary weld and then become sealed in a reservoir beneath a sealing tertiary weld. Thus, predicting which welds seal and which leak is critical to exploration success.

## FLUID FLOW AND SALT

Subsurface fluid flow near a salt layer can be broadly classified as either boundary flow along the contacts of the salt layer (Figure 3.2) or crossflow through the salt layer. Crossflow can be subdivided into diffuse flow that permeates through salt along grain boundaries or focused flow through porous intra-salt inclusions and high permeability damage zones associated with intra-salt faults. Sediments above and sometimes below salt are commonly disturbed following salt deformation (e.g., Davison et al., 1996; Rowan et al., 2003; Schultz-Ela, 2003; Davison, 2009), providing pathways for boundary flow. Formation waters or hydrocarbons are commonly encountered when drilling on the flanks of salt diapirs and through salt pillows and sheets (e.g., House and Pritchett, 1995; Sarkar et al., 1995), which further suggests accumulations of fluid near salt boundaries are common. However, the importance of diffuse and focused crossflow through salt is less widely appreciated.

Casas and Lowenstein (1989) observed depositional porosity up to ~50% in modern salt pans but noted that expansive halite cementation decreases porosity dramatically as salt is buried. Below 45 m depth, halite typically has porosity in the range of 0.1% to 1.4% and in situ permeability around  $10^{-21} \text{ m}^2$  ( $10^{-9} \text{ D}$ ) (Yaramanci, 1994; Bredehoeft, 1988), which is reflected in its capacity to seal tall hydrocarbon columns. At temperature and pressure conditions corresponding to

depths greater than ~3 km for normal geothermal gradients, the dihedral angle between water and halite decreases below 60°, causing pore fluid along halite grain boundaries to form an interconnected porosity network filled with brine (Lewis and Holness, 1996). This process markedly increases permeability, which can exceed  $10^{-16} \text{ m}^2$  ( $10^{-4} \text{ D}$ ) in coarse-grained salt (Schoenherr et al, 2007) or  $10^{-13} \text{ m}^2$  ( $10^{-1} \text{ D}$ ) in fine-grained salt (Lewis and Holness, 1996), providing tubular pathways for the migration of subsurface waters and brine through deep salt. However, the extent to which oil-filled grain-boundary tubes form, and thus the effect on hydrocarbon migration through salt, has not been determined.

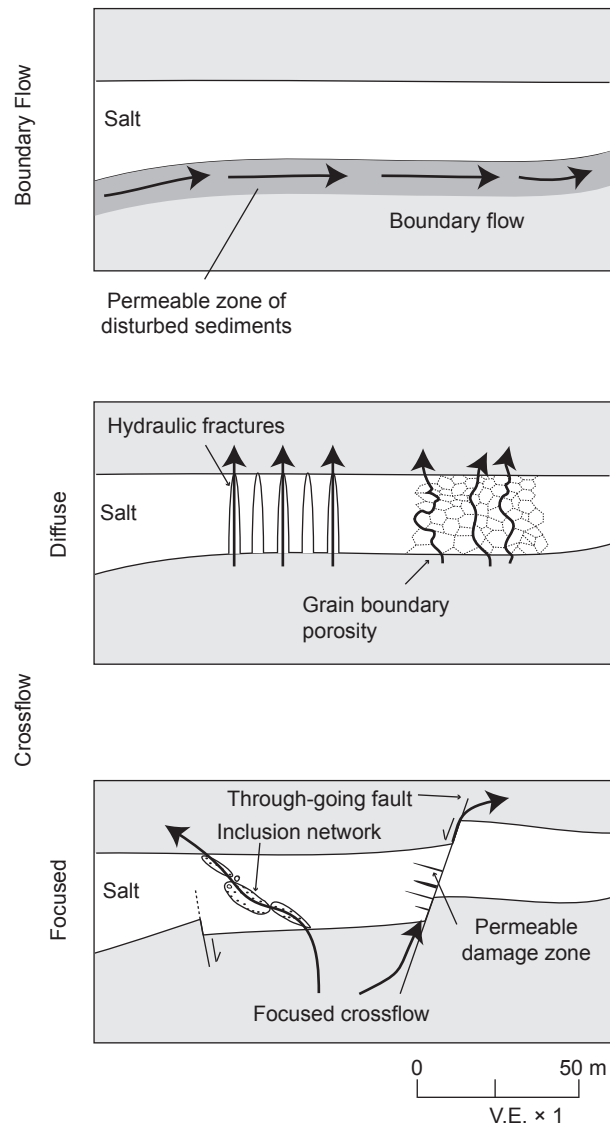


Figure 3.2: Schematic cross sections illustrating fluid flow near a salt body. Flow can be classified into two end-members. Boundary flow (top diagram) occurs when fluids flow along the boundary of the salt, for example along the base of a salt sheet or along the flank of a salt diapir. Crossflow occurs when fluid migrates through salt and can be diffuse (middle diagram) or focused (bottom diagram). In diffuse crossflow, fluids flow through dilatant microcracks (Peach and Spiers, 1996; Popp et al., 2001), hydraulic fractures (Lux, 2005), or interconnected grain-boundary tubes (Lewis and Holness, 1996). In focused crossflow, fluids flow through interconnected intra-salt inclusions or damage zones associated with faults formed during rapid strain. Grain boundaries and hydraulic fractures are schematically enlarged to clarify flow paths.

At differential stresses associated with salt creep and low effective stresses associated with elevated pore fluid pressures, dilatant microcracks may form along halite grain boundaries, increasing the permeability of rock salt (Peach and Spiers, 1996; Popp et al, 2001). Furthermore, hydraulic fractures may form if pore fluid pressure is rapidly elevated above the minimum principal stress (Lux, 2005). The extent to which this process operates in nature is not clear. Diffuse dilation due to fluid overpressures has been documented in abandoned solution mines (e.g., Fokker, 1995) and has been proposed as a reason for the presence of hydrocarbons trapped in halite crystals and along grain boundaries (e.g., Kupfer, 1962; Kupfer, 1990; Schoenherr et al., 2007).

Regardless of the mechanism that enhances salt permeability, non-aqueous fluids, such as liquid hydrocarbons, must overcome capillary entry pressure to infiltrate water-wet salt. Using the methodology of Schoenherr et al. (2007), capillary entry pressure can be calculated using Equation 3.1, where  $P_c$  is capillary entry pressure in megapascals,  $\gamma$  is interfacial tension between the oil and brine (0.025 N/m after Hocott, 1938),  $r$  is the pore-throat radius (0.05 microns after Schenk and Urai, 2004), and  $\varphi$  is the wetting angle ( $0^\circ$  for perfectly water-wet salt).

$$P_c = \frac{2\gamma \cos\varphi}{r} \quad (3.1)$$

Assuming density-driven buoyancy, column height can then be calculated using Equation 3.2, where  $z$  is the height of the hydrocarbon column,  $\rho_w$  is the density of the underlying water,  $\rho_h$  is the density of the hydrocarbons, and  $g$  is gravitational acceleration (modified from Smith, 1966).

$$z = \frac{P_c}{(\rho_w - \rho_h)g} \quad (3.2)$$

Using these parameters, capillary entry pressure is 1 MPa, which is large enough to seal a column of oil in excess of ~500 m (Figure 3.3). Thus, even when the permeability of salt is enhanced by these mechanisms it remains a significant barrier to fluid migration.

Salt typically deforms at low differential stresses by dislocation glide (e.g., Carter and Hansen, 1983; Carter et al., 1993) and fluid-assisted diffusion and solution-precipitation creep (e.g., Urai et al., 1987; Ter Heege et al., 2005). However, thin salt may fault to produce a permeable damage zone, allowing focused crossflow of subsurface fluids. Dynamically scaled physical models indicate brittle faulting at the regional scale of salt tectonics is controlled by salt thickness and strain rate; thin evaporites are more susceptible to basement-involved faulting than thick evaporites, which more efficiently decouple deformation above and below salt (Vendeville et al., 1993; Withjack and Callaway, 2000). Thrust and normal faults with offsets ranging from 0.1 – 10 m

have been described in salt and potash mines around the world and in many cases are associated with damage zones and extensional fractures containing recrystallized evaporites or hydrocarbons (Davison et al., 2009). However, faults and fractures through salt may only produce ephemeral pathways for fluid migration; grain boundary migration may completely recrystallize high-permeability zones near intra-salt faults, inhibiting long-term fluid flow (e.g., Kupfer, 1968; Davison, 2009).

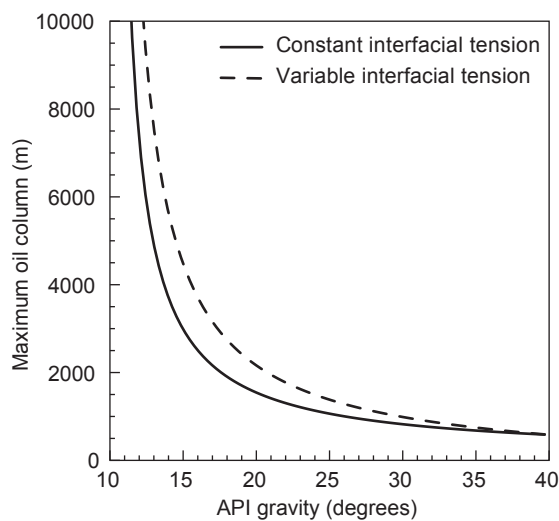


Figure 3.3: The capacity of salt to seal hydrocarbons is controlled by capillary entry pressure. A capillary entry pressure of 1 MPa (calculated in text) can seal tall hydrocarbon columns. Hydrocarbons in a reservoir are commonly pressured because they are less dense than the brines below. The specific gravity of oil is commonly expressed in API gravity, a comparative scale where fresh water is equal to 10° API. The solid curve represents the maximum oil column that can be sealed for a given API gravity assuming a constant interfacial tension between oil and fresh water of 0.025 N/m (25 dynes/cm) (after Hocott, 1938). Interfacial tension is commonly inversely proportionate to API gravity (O'Connor, 2000), and the dashed line represents the maximum oil column that can be sealed using an interfacial tension that varies linearly from 0.025 N/m at 40° API to 0.040 N/m (40 dynes/cm) at 10° API.

## DISSOLUTION

Dissolution at the scale of salt welds has two requirements: 1) an ample supply of subsurface water undersaturated with respect to halite and 2) a hydrodynamic regime that promotes subsurface flow. Meteoric waters are plentiful near the surface of the Earth, where they dissolve soluble evaporites, such as halite. Dissolution leaves a residue of insoluble evaporites, primarily gypsum and anhydrite, as the first stage of reactions that ultimately form an assemblage known as caprock (Murray, 1966; Gussow, 1968). Shallow dissolution by infiltrating meteoric waters also creates sinkholes and karst topography (e.g., Anderson, 1981; Johnson, 1997; Guerrero et al., 2008).

In contrast, salt dissolution in the deep subsurface (> ~1 km deep) is poorly constrained. Deep wells in evaporite basins commonly encounter highly saline formation waters (e.g., > 30 g NaCl per L reported in Land, 1995). The volume of rock salt dissolved to reach these salinities is difficult to estimate because even evaporite-free basins contain salty formation waters. Cartwright et al. (2001) used basin-scale dissolution to explain thickness variations in Zechstein evaporites in the Forth Approaches Basin ~1 km below the North Sea, but they were unable to distinguish the effects of dissolution from the effects of salt creep. Although dissolution is commonly invoked to explain area loss of up to 50% in restored cross sections (e.g., Hossack, 1995), salt flow out of the plane can also explain such volume loss. Where salt is deeply buried and fluid

migration is sluggish, dissolution is likely to be much less important than creep in reducing cross-sectional area of salt. However, the extreme salinities of some subsurface waters are difficult to explain without widespread dissolution (e.g., Land, 1995).

Mass balance can provide a first-order estimate of the fluid volumes required to dissolve salt layers. The solubility of halite in pure water at standard temperature and pressure is 36.0 g NaCl per kg H<sub>2</sub>O (Ford and Williams, 1989) and increases slightly with temperature and the ionic strength of aqueous solutions (e.g., Gavrieli et al., 1989). The volume of water ( $V_w$ ) required to completely dissolve a given volume of rock salt ( $V_s$ ) with a solubility of 36.0 g NaCl per kg H<sub>2</sub>O is given by Equation 3.3, where  $\rho_s$  is halite density 2163 kg/m<sup>3</sup> (Carmichael, 1984),  $\chi$  is weight percent NaCl, and  $\rho_b$  is the brine density. Brine density is calculated using Equation 3.4 where  $\rho_w$  is the density of pure water (1000 kg/m<sup>3</sup>). For a given porosity ( $\phi$ ), the rock volume ( $V_w$ ) that must be drained to provide this water is calculated using Equation 3.5.

$$V_w = \frac{\rho_s V_s}{(0.357 - \chi)\rho_b(\chi)} \quad (3.3)$$

$$\rho_b(X) = \rho_s X + \rho_w(1 - X) \quad (3.4)$$

$$V_r = \Phi V_w \quad (3.5)$$

Although halite is much more soluble than most other common rocks, salt dissolution requires enormous volumes of water (Figure 3.4). Over  $6 \text{ km}^3$  of freshwater (over  $6.5 \text{ km}^3$  of seawater containing 3% NaCl by weight) are needed to completely dissolve  $1 \text{ km}^3$  of halite. Even greater volumes are required to dissolve halite with salty formation waters. If rock salt contains only 1% brine where buried deeper than  $\sim 45 \text{ m}$  (Casas and Lowenstein, 1989), the large volumes of water required for dissolution must be sourced elsewhere. Meteoric waters are reported in aquifers as deep as  $2 \text{ km}$  (e.g., Habermehl, 1980) but this is a spectacular example. Downward migration of meteoric water is limited by the presence of shallow permeability barriers, such as salt sheets, and overpressures. Moreover, the positive buoyancy of fresh water with respect to saline formation waters limits downward migration. Therefore, it seems unlikely that large volumes of meteoric water are readily available to form welds deeper than  $\sim 1 \text{ km}$ .

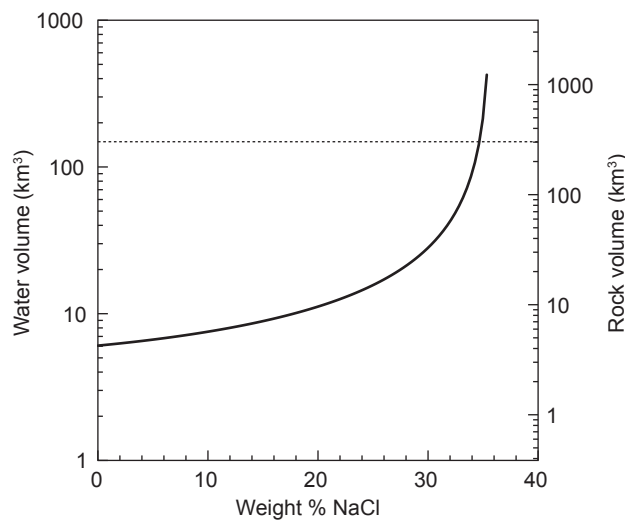
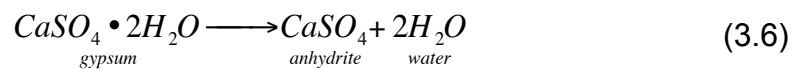


Figure 3.4: Water volume (left axis) and rock drainage volume (right axis) required to completely dissolve 1 km<sup>3</sup> (equivalent to a 100 m thick salt body over an area of 10 km<sup>2</sup>) of pure halite for aqueous NaCl solutions assuming a constant solubility of 36.0 g NaCl per kg H<sub>2</sub>O. Rock volume was calculated assuming a porosity of 26%, which represents closest (rhombohedral) packing porosity for perfect spheres. 100 km<sup>3</sup> is equal to 2.64 × 10<sup>13</sup> gallons. For comparison, Lake Tahoe on the California-Nevada border contains ~150 km<sup>3</sup> of water (dashed line).

Three common sources of water must be responsible for dissolution at depth: 1) connate water or brines expelled during burial compaction of rocks near salt and infra-salt aquifers (Cartwright et al., 2001), 2) dehydration reactions of hydrated evaporites (e.g., Schlöder et al., 2008), and 3) dehydration reactions during prograde diagenesis of other rocks. The volume of water released during burial compaction is controlled by initial porosity and the degree of compaction. Consider a sandstone having an initial porosity of 26% filled with fresh water. Over 24 km<sup>3</sup> of this sandstone must be completely drained of pore fluid to dissolve just 1 km<sup>3</sup> of halite (Figure 3.4). The volume of water released during dehydration of hydrated evaporites or nearby rocks during prograde diagenesis varies depending on the involved lithologies. Consider the dehydration of gypsum to anhydrite (Equation 3.6) at ~1 km depth depending on temperature and pressure conditions (Jowett, 1993).



Gypsum dehydration releases 2 moles of structural water, enough to dissolve just 0.22 moles of halite. Converting to volume, dissolving 1 km<sup>3</sup> of halite requires over 12 km<sup>3</sup> of gypsum dehydration. Alternatively, coseismic strain along normal faults, and to a lesser extent strike-slip faults, can expel up to ~0.1 km<sup>3</sup> per year (Muir-Wood and King, 1993; Blundell et al., 2003). However, salt

deformation is commonly basement detached (e.g., Vendeville et al., 1993) so this mechanism seems unlikely to contribute much water to dissolve salt except in seismically active regions. Obtaining the volumes of water required for salt dissolution at depths more than ~1 km appears problematic.

Even if large volumes of dissolving water are readily available in the deep subsurface, sluggish fluid flow will limit dissolution. Dissolution stops when the water in contact with salt becomes saturated. The volumes of water required for dissolution are much greater than the volumes of salt being dissolved, so fluid migration must replace brine saturated by contact with salt. Fluid flow in the deep subsurface is driven primarily by compaction and buoyancy so flow is largely vertical. Formation waters flow laterally when rising fluids meet a permeability barrier, such as salt, and are deflected updip along the base of the barrier until they escape upward or become trapped. Brines migrating along the base of a salt body that reach saturation can be expelled out the front or sides of the sheet or sink due to their increased density to allow fresher brines to continue dissolving the salt (Figure 3.5a). Furthermore, some of this water may be expelled at the surface as saline springs (e.g., Orange, 1993). If caprock forms in the deep subsurface, it may also retard dissolution. Dissolution by boundary flow will concentrate less-soluble evaporite minerals and inclusions at the edges of the salt layer, armoring the soluble center of the evaporites and inhibiting further dissolution (Figure 3.5b-c).

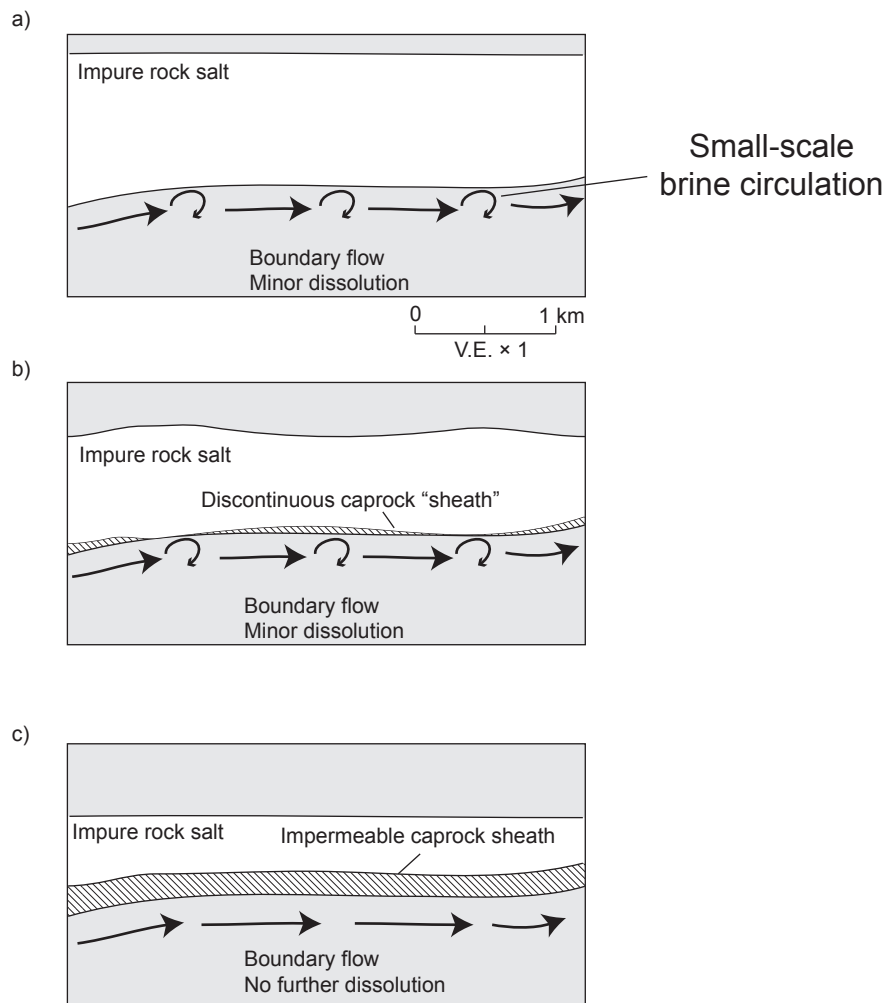


Figure 3.4: Schematic cross sections illustrating the growth of a protective sheath of caprock formed by boundary-flow dissolution. a) Fluids flowing along the base of an impure salt layer dissolve halite and leave a residue of less soluble evaporites and inclusions known as caprock. As the fluids in contact with salt become saturated, they are expelled out from beneath the sheet or sink to allow fresher fluids to continue dissolution. b) As dissolution continues, a patchy caprock veneer coats the base of salt, reducing the volume of water in contact with salt and the rate of dissolution. c) Once a continuous sheath of impermeable caprock protects the base of salt, dissolution largely ceases. The thickness of caprock depends on the proportion of insoluble impurities in the salt and the amount of salt dissolved.

Copper mineralization in the Kupferschiefer ore deposits of Germany and Poland is stratabound along the inferred direction of boundary flow at the base of the Zechstein evaporites (Blundell et al., 2003). Copper was leached from pre-evaporite volcanic rocks, transported as cuprous chloride complexes in brines released by evaporite dissolution, and then precipitated under oxidizing conditions in the Kupferschiefer dolomitic shale and Rotliegend sandstone at the base of the Zechstein. The mineralizing fluids migrated ~30 km updip along the base of the sealing Zechstein evaporites. Similarly, saline formation waters flowed updip along the base of the Jurassic Louann salt in the Texas Gulf Coast (e.g., Land and Prezbrindowski, 1981; Land et al., 1988). In spite of the scale of these examples, their dissolution rates are poorly constrained.

If salt and the surrounding rocks are treated as porous media, Darcy's Law provides a first-order approximation of dissolution. First, flow rate ( $u$ ) in a confined aquifer is calculated using Equation 3.7, where  $k$  is permeability,  $\mu$  is the dynamic viscosity of the fluid,  $dp/dx$  is the pressure head gradient,  $\rho_b$  is the density of the brine, and  $\theta$  is the dip of the aquifer (Turcotte and Schubert, 1982, eq. 9-4). Dissolution rate is then calculated by normalizing flow rate to the geometry of the flow.

$$u = \frac{k}{\mu} \left( \frac{dp}{dx} - \rho_b g \sin \theta \right) \quad (3.7)$$

Analytical models were used to quantify the effect of dissolution by boundary flow and diffuse crossflow (Figure 3.2). By its nature, focused crossflow does not promote widespread dissolution, but can locally remove salt to form a complete weld. For simplicity, salt and sediment density are held constant at 2163 kg/m<sup>3</sup> (density of pure halite from Carmichael, 1984). Input brine salinity, density, and viscosity are also held constant (Table 3.1), and for modeling purpose, all brine in contact with salt is instantly saturated. Input parameters were obtained for an aqueous solution of NaCl and viscosities were calculated for fluids at 90°C using empirical relationships determined by Kestin and Shankland (1984).

Table 3.1 Brine density and viscosity used to model dissolution

Weight % NaCl	Density (kg/m <sup>3</sup> )	Dynamic Viscosity (Pa•s × 10 <sup>-3</sup> )*
0 (freshwater)	1000.0	3.15
3.5 (seawater)	1040.7	3.41
10	1116.3	3.89
20	1232.6	4.73

\*Calculated for aqueous solutions of NaCl at 90° C using Equations 21a and 21b from Kestin and Shankland (1984).

To model dissolution by boundary flow, consider brine flowing along the base of salt sheet dipping at 1° (Figure 3.6a). In this model, brine rises vertically to the base of the sheet and then flows laterally through a carrier bed having  $k =$

$10^{-13} \text{ m}^3$  (0.1 D). Brine flows 10 km along the base of the sheet until it is expelled at hydrostatic pore-fluid pressures. Pore pressure of the input brine at the base of the sheet is incrementally varied from just above hydrostatic (calculated using brine density) to lithostatic along the base of the sheet to investigate how hydraulic gradient affects dissolution. Salt is considered impermeable, so dissolution is restricted to a 10-cm-thick zone along the base of salt. Dissolution rate in the model ranges from 3 to 36 m/m.y. and is proportional to hydraulic gradient and inversely proportional to brine salinity (Figure 3.6b). Dissolution is enhanced by increasing the permeability of the carrier bed beneath the sheet, or by increasing the width of the dissolution zone within salt. Calculated hydraulic gradient ranges from 0.2 to 2.7 MPa/m and flow rate ranges from 0.3 to 2.8 m/y, which approach some of the largest gradients and flow rates inferred in nature (e.g., Blundell, 2003). Therefore, the model results are a plausible upper limit on dissolution during boundary flow in the subsurface. For comparison, known dissolution rates of evaporites at the surface range from 1 m/m.y. for the Salado formation in west Texas (Anderson, 1981) to 50 m/m.y. for Hormuz salt glaciers exposed to rainfall in Iran (Talbot and Jarvis, 1984). Furthermore, Sarkar et al. (1995) predicted similar dissolution rates (3-5 m/m.y.) when modeling free thermohaline pore fluid convection beneath salt sheets in the Gulf of Mexico.

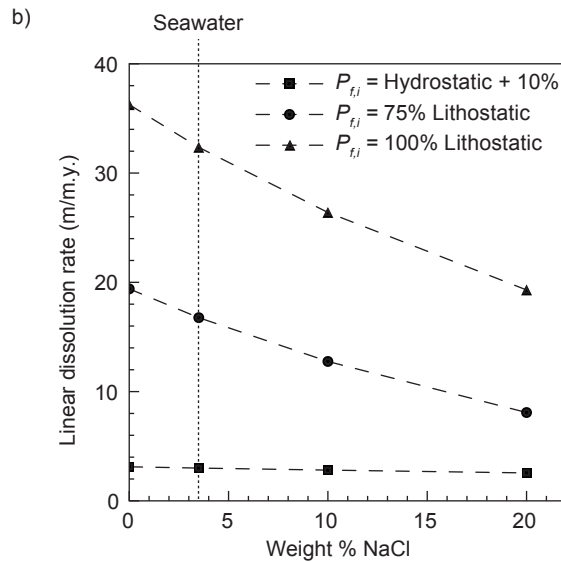
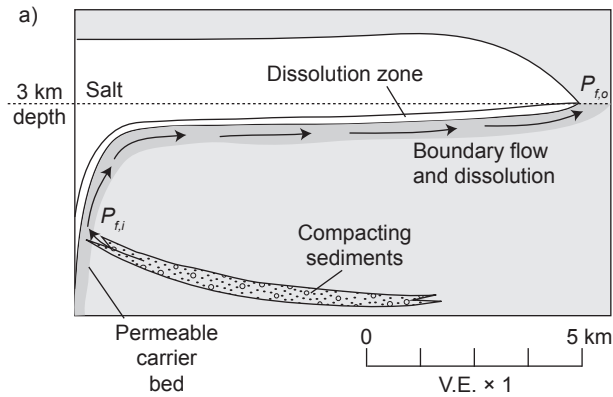


Figure 3.6: Model setup and results for dissolution by boundary flow. a) Overpressured fluids ( $P_{f,i}$ ) expelled from compacting sediments flow 10 km through a permeable carrier bed along the base of a shallowly dipping salt sheet, dissolving a 10-cm-wide zone of salt before being expelled at hydrostatic fluid pressures ( $P_{f,o}$ ) at the front of the sheet. b) Linear dissolution rate in the vertical direction for aqueous NaCl solutions, assuming a constant solubility of 36.0 g NaCl per kg  $H_2O$ . The three curves represent different overpressures in the source brine and were calculated using a neutrally buoyant overburden with an average bulk density of 2163 kg/m<sup>3</sup>. Hydrostatic conditions were calculated assuming a pure mixture of NaCl and  $H_2O$ , so hydraulic gradients vary slightly with brine composition. Dissolution rate increases with hydraulic gradient and decreases with weight % NaCl.

Now consider crossflow of brine through brine-filled grain-boundary tubes at depths of 3 km or more (e.g., Lewis and Holness, 1996). In this model, brine flows upward and through a 100 m-thick salt layer with permeability  $10^{-16} \text{ m}^2$  ( $\sim 10^{-4} D$ ) (Lewis and Holness, 1996), dissolving it along the way (Figure 3.7a). Pore pressure above the salt is held at hydrostatic, and pore pressure below the salt varies. Dissolution rate at the onset of flow versus brine composition and pressure regime is plotted in Figure 3.7b. Dissolution in the model at dm per year rapidly dissolves salt. However, the calculated hydraulic gradients and flow rates are up to six orders of magnitude larger than those inferred in nature, so the extent to which this second model represents natural salt dissolution during crossflow is unclear. Once the salt seal has been breached, any subsalt overpressure will tend to drain into the overburden, decreasing the rate of dissolution. When the rate of fluid escape through the salt sheet is greater than the rate of overpressure generation, dissolution rate will decay and vice versa. However, a vertical hydraulic gradient of just 30 Pa/m above hydrostatic can dissolve  $\sim 30$  m of salt thickness per million years in the model. Thus, diffuse crossflow may effectively dissolve large volumes of buried salt even where only a minor overpressure can be sustained.

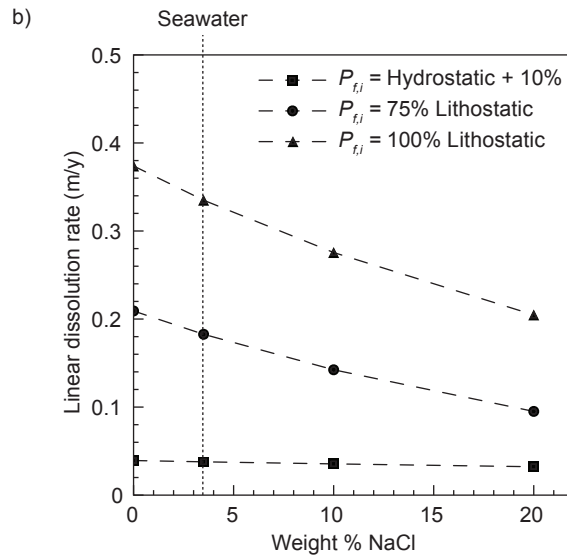
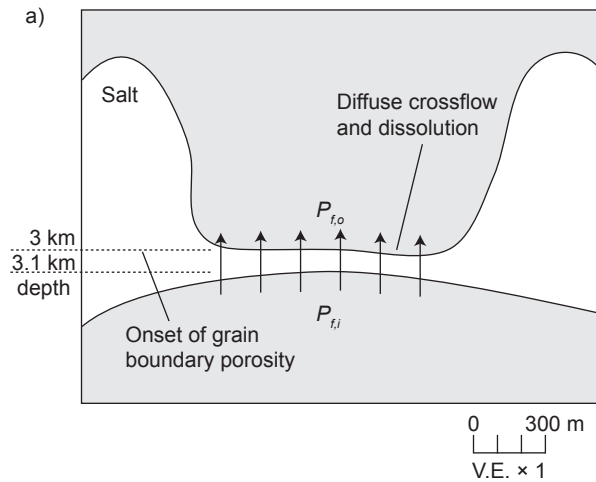


Figure 3.7: Model setup and results for dissolution caused by crossflow. a) Overpressured fluids ( $P_{f,i}$ ) beneath a 100-m-thick salt body percolate through salt with permeability  $10^{-16} \text{ m}^2$  ( $10^{-1} D$ ) (Lewis and Holness, 1996) before being expelled at hydrostatic fluid pressures ( $P_{f,o}$ ) above the salt. b) Linear dissolution rate in the vertical direction for aqueous NaCl solutions, assuming a constant solubility of 36.0 g NaCl per kg  $\text{H}_2\text{O}$ . The three curves represent different overpressures in the source brine and were calculated using a constant overburden density of  $2163 \text{ kg/m}^3$ . Hydrostatic conditions were calculated assuming a pure mixture of NaCl and  $\text{H}_2\text{O}$ , so hydraulic gradients vary slightly with brine composition. Again, dissolution rate increases with hydraulic gradient and decreases with weight % NaCl. As soon as fluids have breached the continuous salt layer, additional dissolving fluids will be drawn toward the breach, causing runaway dissolution.

I conclude that the effect of dissolution welding depends critically on depth. Shallower than ~1 km, meteoric groundwater rapidly dissolves salt to create caprock, sinkholes, and complete welds. Below the depth of meteoric circulation but above ~3 km where halite grains re-equilibrate to form a porous network, dissolution is slow, removing up to several meters of salt per million years. Below ~3 km, diffuse crossflow through permeable salt rapidly dissolves salt in the model, but this dissolution rate can decay as subsalt overpressures are released. In three dimensions, flow of dissolving fluids beneath and through salt bodies may be focused along high-permeability pathways. Salt dissolution near these high-permeability pathways will focus additional dissolving fluids, resulting in runaway dissolution in a few locations.

#### **HYDROCARBON MIGRATION THROUGH SALT WELDS**

Welds are internally complex and heterogeneous structures (e.g., Giles and Lawton, 1999; Jackson et al., 2003; Dyson and Rowan, 2004; Rowan, 2004; Chapter 2). The capacity of a salt weld to seal hydrocarbons or mineralizing fluids depends on lithology, internal structure, geometry, and the availability of fluid migration pathways above, below, and within the weld (Figure 3.8). Ductile, low-permeability rocks, such as evaporites or mudstones, within and surrounding a weld promote sealing. In contrast, brittle, highly permeable rocks, such as porous sandstones or fractured carbonates, within and surrounding a weld

promote leaking. Shear displacement along the weld surface (e.g., Hossack and McGuinness, 1990; Giles and Lawton, 1999; Rowan et al., 1999) has a variable effect on seal capacity. For example, the damage zone associated with faults that form through a weld can enhance permeability, but fault gouge or shale smear can promote sealing (e.g., Rowan, 2004). If dissolution breaches a partial weld, feedback becomes important and more dissolving fluids are drawn toward the leak point. With this in mind, an old weld is more likely to leak than a young weld because any leak points may be enlarged by focused runaway dissolution. Furthermore, dissolution can remove ductile evaporites and leave a brittle residue, which can fault when sheared. Finally, subsurface fluids may also be diverted from welds by salt geometry or adverse hydraulic gradients (e.g., McBride et al., 1998). It is impractical to predict the extent of all these features on subsurface data, so I focus on how weld timing, remnant evaporite thickness, and weld area affect the tendency of welds to seal or leak.

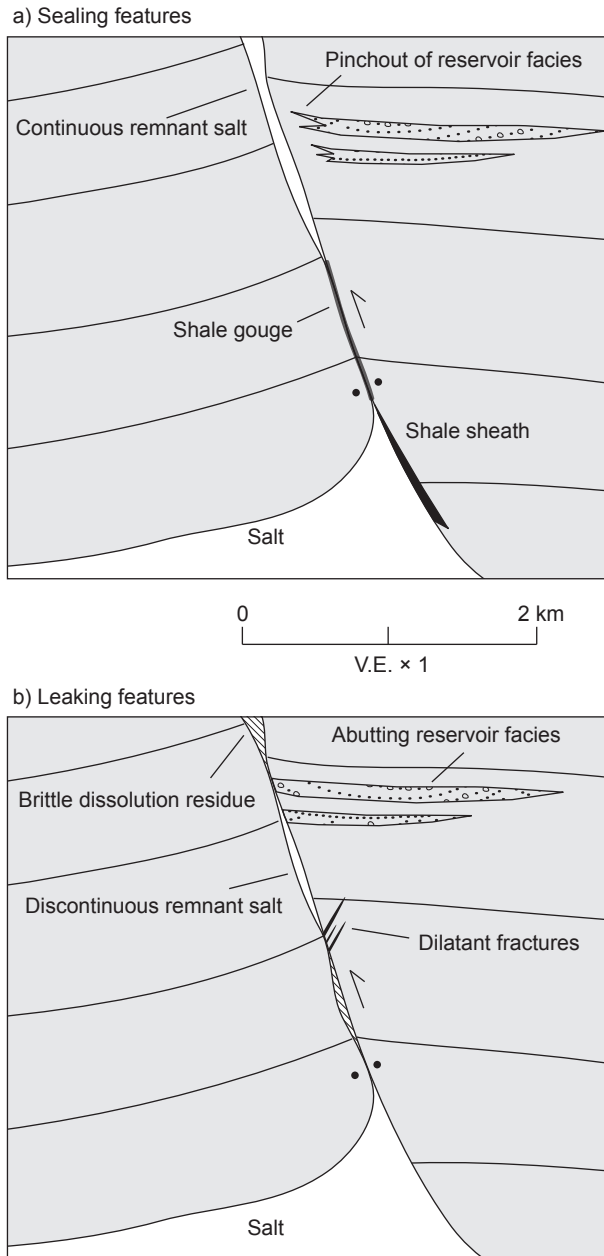


Figure 3.8: a) Structural and stratigraphic features of salt welds that promote sealing include continuous remnant evaporites, a shale sheath that stratigraphically draped the original diapir, shale gouge produced during shear displacement, and lateral pinchout of reservoir facies away from the weld surface. b) Structural and stratigraphic features of welds that promote leaking include gaps between discontinuous remnant evaporites caused by differential salt evacuation or channelized dissolution, the presence of caprock or insoluble residues that are more permeable than salt, brittle faults and the associated damage zone caused by shear displacement, and reservoir facies that abut the weld surface.

Timing is important in any petroleum system, and weld timing is no exception. Hydrocarbon migration from subsalt source rocks to suprasalt reservoirs depends critically on weld timing. For subhorizontal welds, weld timing can be inferred by identifying the cessation of local synkinematic sedimentation above evacuating salt (Figure 3.9a). At the basin scale, the timing of subhorizontal welding can be estimated by mapping variations in overburden thickness through time, but stratal architecture above welds can be used to generate a more robust understanding of primary weld timing (Jackson and Cramez, 1989; Roberts et al., 2005). Subvertical welds form during 1) lateral shortening of subvertical evaporite structures (e.g., Cobbold et al., 1995; Dooley et al., 2009), 2) strike-slip displacement along lateral faults adjacent to salt structures (e.g., Rowan et al., 1999), and 3) minibasin subsidence with rotation (e.g., Jackson and Cramez 1989; Rowan and Weimer, 1998). Thus, the origin of a given subvertical weld must be determined before timing can be established. For example, subvertical welds that form by lateral shortening can typically be correlated to regional shortening events to infer weld timing (e.g., Cobbold et al., 1995; Brun and Fort, 2004; Jackson et al., 2008). The relationship between hydrocarbon charge and timing for welds is simple; welds that form prior to hydrocarbon migration are more likely to act as migration pathways (Figure 3.9b).

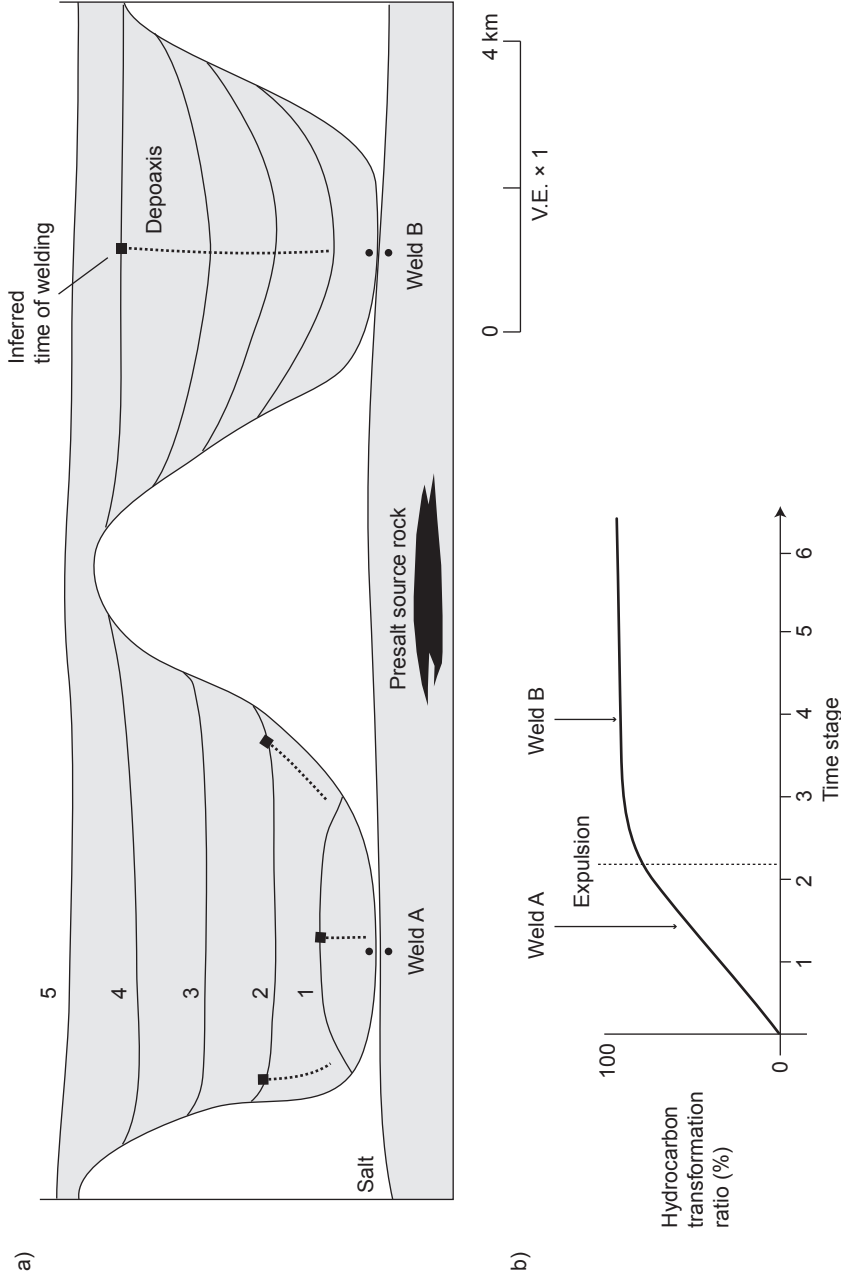


Figure 3.9: a) Schematic cross section illustrating a common method used to infer weld timing (e.g., Jackson and Cramez, 1989). Thickness variations in the sediments above Weld A record two pulses of salt withdrawal. The minibasin above the center of the weld locally subsides until time 1, when the center of the minibasin welded. The flanks of the minibasin subsided until time 2, when the flanks welded. Thickness variations in the sediments above Weld B record a much longer history of salt withdrawal. The minibasin center began to subside at time 2 and continued through time 4 when welding ended. b) Schematic curve of hydrocarbon transformation ratio for the source rock in (a). Here, hydrocarbons are expelled just after time 2 and flow through Weld A into the overburden. Weld B acted as a seal until time 4 so could only act as a migration pathway if residual hydrocarbons were being released at that time.

In spite of mechanisms enhancing salt permeability, continuous evaporites are excellent seals (e.g., Downey, 1984; Warren, 2006). However, a seal is only as strong as its weakest point, so seal continuity is vital to weld seal. Seal continuity depends on remnant evaporite thickness. Thick evaporites are more likely to be continuous than thin evaporites as they are less susceptible to faulting and fracture than thin evaporites and can withstand more dissolution before being breached. Warren (2006) suggested that 30 meters of salt makes an excellent seal. Live oil and solid bitumen is trapped within halite crystals and along grain boundaries up to ~10 m away from self-sourcing carbonate stringers surrounded by rock salt in Oman (Schoenherr et al., 2007). Thus, 10 m is probably a minimum salt thickness required to maintain a seal.

Seal continuity also depends on weld area, but in contrasting ways. On the one hand, broad areas ( $> \sim 25 \text{ km}^2$ ) of partially welded salt are more likely to contain small breaching points or "spot welds" caused by faults or where dissolution is channeled through extensional fractures near faults. On the other hand, analytical and numerical models indicate large welds likely contain thicker remnant evaporites than smaller welds (Chapter 1), increasing their ability to seal.

## **CASE STUDY: CAMPOS BASIN, OFFSHORE BRAZIL**

Salt welds are crucial migration pathways for the prolific post-salt petroleum system of the Campos Basin, offshore Brazil. Most hydrocarbons in the Campos Basin were generated in pre-salt lacustrine shales in the Aptian Lagoa Feia Formation. The hydrocarbons migrated through permeable salt welds and charged overburden reservoirs of Albian carbonate mounds and Upper Cretaceous to Tertiary turbidites (e.g., Guardado et al., 1989; 2000). Enormous volumes of hydrocarbons migrated through welds: proven reserves of at least ten (10) billion barrels of oil equivalent (bboe) exist in post-salt reservoirs the Campos Basin in several giant and supergiant fields, including Albacora (~650 mmboe), Jubarte (~600 mmboe), Marlim (~2 bboe), and Roncador (~3 bboe).

When exploration wells do not encounter commercial accumulations of hydrocarbons, it is difficult to determine the exact element or elements of the petroleum system that are to blame. For example, reservoir facies on the flanks of salt domes and walls may thin or pinch-out before contacting salt (e.g., Levorsen, 1967; Rowan, 2004). After welding, the trap mechanism may still be the original pinchout, which could be below the resolution of seismic imaging. For example, Hudson and Hanson (2010) observed non-biodegraded hydrocarbons in upturned sediments just 5 m away from the La Popa Weld in northern Mexico. Sub-seismic faults, facies changes, changes in reservoir quality, and impermeable lithologies in contact with welds can all serve as traps or seals,

making it difficult to infer the role any given salt weld plays in the petroleum system.

Welds are the only recognized migration pathway from the presalt source rocks to the postsalt reservoirs in the Campos Basin petroleum system. In many wells, hydrocarbons are trapped in reservoirs directly below and in contact with thin (< ~50 m) salt, (e.g., Wahoo discovery), confirming the sealing ability of some welds. Post-salt oils are typically degraded by microbial activity and degassing (Candido and Cora, 1992) and are of low API gravity (typically less than 30°) and high viscosity (greater than  $\sim 4 \times 10^{-3}$  Pa•s (4 cP) for live oil and greater than  $\sim 4 \times 10^{-1}$  Pa•s (400 cP) for dead oil) (Pinto et al., 2003). As a result, widespread oil staining of the overburden records past hydrocarbon flow (Wagner Peres, personal communication, 2007), indicating cross-weld migration occurred even if some other element, such as trap geometry or seal, failed. Where unsuccessful wells encounter unstained reservoir rock in the overburden, one possible cause is a lack of cross-weld migration.

Approximately 8000 km<sup>2</sup> of three-dimensional seismic data spread over three surveys were used to map salt welds in the Campos Basin (Figure 3.10). Remnant evaporite thickness was estimated from amplitude variations of the weld reflection following the guidelines in Chapter 2. Weld area was calculated by determining the area where salt is < 100 m thick. These physical parameters of welds were then compared with exploration outcomes using well and field data

to empirically understand weld permeability. Wells were chosen to investigate the effect of weld area and thickness on migration failure or success, so I avoided wells lacking reservoir or that tested reservoirs above welds that formed after hydrocarbon migration peaked in the Miocene (Guardado et al., 2001). Of 19 wells selected from a database of 65 in the area covered by the available seismic data, five (5) were commercial, four (4) were subcommercial, and 10 were dry holes.

Not surprisingly, thin ( $< \sim 50$  m), broad ( $> \sim 25$  km<sup>2</sup>) partial welds are associated with successful wells (Figure 3.11). Based on well data and seismic interpretation, hydrocarbons in the region migrated through evaporites that are presently as thin as  $\sim 18$  m or as thick as  $\sim 60$  m. Composition may cause this variation; halite is the dominant evaporite mineral in the basin, but anhydrite is common where the evaporites are thin (Chapter 1) and makes a poorer seal than halite (e.g., Downey, 1984). Only one of the wells containing hydrocarbons was associated with a partial weld  $< 10$  km<sup>2</sup> in areal extent.

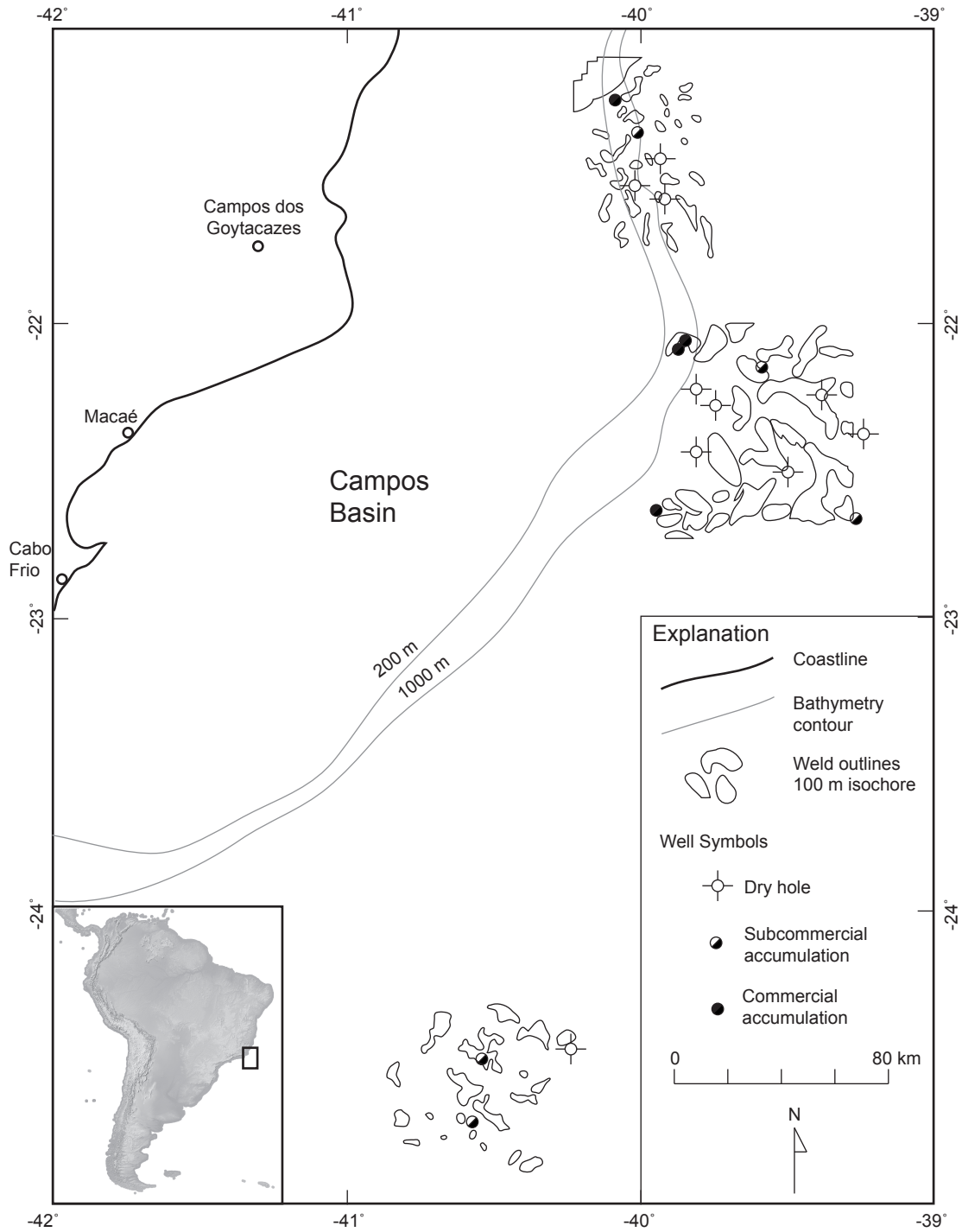


Figure 3.10: Map of the Campos Basin, offshore Brazil, showing the study area (inset). Areas where salt is thinner than 100 m are outlined black and range from less than 1 km<sup>2</sup> to greater than 200 km<sup>2</sup>. Wells are labeled as commercial, subcommercial, or dry holes according to drill reports and independent of the reserves they encounter. Shaded relief map made with Natural Earth, free vector and raster map data at [www.naturalearthdata.com](http://www.naturalearthdata.com).

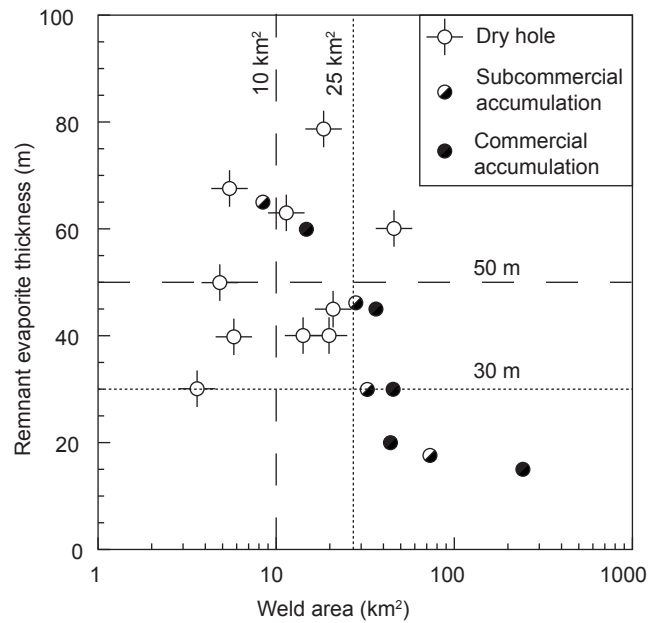


Figure 3.11: Crossplot of partial weld area and remnant evaporite thickness based on three-dimensional seismic mapping and well data from the Campos Basin, offshore Brazil. These data suggest partial welds greater in area than  $\sim 10 \text{ km}^2$  containing evaporites thinner than  $\sim 50 \text{ m}$  tend to act as pathways for migrating hydrocarbons. Only one weld smaller than  $\sim 10 \text{ km}^2$  in area encountered hydrocarbons, and all wells associated with welds broader than  $\sim 25 \text{ km}^2$  containing evaporites thinner than  $\sim 30 \text{ m}$  were successful.

## CONCLUSIONS

Analytical models of fluid flow near and through salt reveals how salt is removed by dissolution. Shallow dissolution by meteoric water can easily remove salt, but analytical models and hydrodynamic considerations suggest that dissolution plays only a minor role in welding deeper than ~1 km. Even at elevated hydraulic gradients and flow rates, boundary-flow dissolution is limited to a few meters per million years. Dissolution by diffuse crossflow may be significant when flow starts and subsalt overpressure is large, but can slow if those overpressures decay. Predicted dissolution rates are significantly slower than the rates of viscous flow, but a partial weld containing ~50 m of remnant salt can be completely dissolved within a few million years. Like the fabled tortoise and hare, viscous flow can rapidly expel enormous volumes of salt, but has trouble finishing the welding race when creep becomes restricted by boundary drag. Slow dissolution can remove the stubborn remaining salt in a few locations to form a complete weld and provide pathways for cross-weld migration.

The tendency of salt welds to act as seals for migrating hydrocarbons depends on a number of factors, including lithology and the availability of migration pathways within and surrounding the weld. Partial welds having thin remnant evaporites (< ~50 m) and large areal extent (> ~25 km<sup>2</sup>) correlate with successful wells and fields in the Campos Basin, offshore Brazil, which can be used to predict whether welds seal or leak in this and other exploration basins.

## **ACKNOWLEDGEMENTS**

I thank Mark Cloos, Ron Steel, and Mrinal Sen at the Jackson School of Geosciences and Frank Peel at BHP Billiton for comments and reviews. Devon Energy for provided access to seismic and well data and facilitated the senior author's research. Additional seismic data was provided by Petroleum Geo-Services. I also thank Richard Jones of Woodside Energy for providing information and insights pertaining to weld seal in the Gulf of Mexico. This work was funded by the Jackson School of Geosciences and the Applied Geodynamics Laboratory, a salt tectonics research consortium at the Bureau of Economic Geology at the University of Texas at Austin.

## **Appendix A: Viscous Flow Equations and Error Analysis**

Here, the errors introduced by assumptions and simplifications behind Equation 1.2 are quantified. First, the results from the Navier-Stokes equations can only be obtained by assuming salt has constant viscosity with respect to strain rate (Newtonian flow) and density. The density of pure halite is  $2163 \text{ kg/m}^3$  (Carmichael, 1984), but impure rock salt typical of the Gulf of Mexico is approximately  $2200 \text{ kg/m}^3$  at surface temperatures (Hudec et al., 2009). Halite is all but incompressible (Carter and Heard, 1970; Voronov and Grigor'ev, 1976), however halite density decreases slightly with increasing temperature due to volumetric thermal expansion. The average thermal expansivity of halite is approximately  $1.30 \times 10^{-4} \text{ K}^{-1}$  (Walker et al., 2004); for a geothermal gradient of  $20 \text{ }^\circ\text{C/km}$ , salt density decreases by only 3% to  $2114 \text{ kg/m}^3$  from surface conditions to 5 km depth. As such, halite density is constant at the scale of subhorizontal welds and nearly constant in subvertical welds. The remaining assumptions and simplifications relate to model geometry and numerical approximation.

### **TEMPORAL AND SPATIAL ACCELERATIONS**

The total time derivative of flow velocity on the left hand side of Equation 1.2 consists of one time-dependent term and three space-dependent terms (Equation A.1). The low Reynolds number associated of salt flow allows these

accelerations to be ignored outright without significant error, but this discussion quantifies the error ignored. Time-dependent accelerations are excluded by assuming the flow is steady-state and has achieved steady-state equilibrium. Space-dependent accelerations are excluded by limiting changes in the flow geometry such that stream lines are parallel (uniform flow), as imposed by the parallel plates in the model system.

$$\frac{Du}{Dt} = \frac{\partial u}{\partial t} + u_x \frac{\partial u}{\partial x} + u_y \frac{\partial u}{\partial y} + u_z \frac{\partial u}{\partial z} \quad (\text{A.1})$$

The time-dependent term above is zero when the flow velocity is not accelerating in time and has reached steady-state equilibrium. The total one-dimensional strain of any solid is the sum of the elastic, plastic, transient creep, steady-state creep, and tertiary creep strains (Carter et al., 1993). Elastic and plastic strains are small at the high strains typical of salt flow, and tertiary creep precedes brittle failure (Carter et al., 1993), so these strains can be ignored in this analysis. Transient creep (Andrade, 1910) is work hardening; readily available deformation pathways are exploited and strain rate decelerates before steady-state viscous flow begins. Experimental observations indicate transient creep in halite is only significant until perhaps 7% to 32% total strain (Ter Heege et al., 2005), and can be safely neglected for modeling natural welds, where strain reaches thousands of percent. Only steady-state creep remains significant,

so that the flow is steady provided the controlling conditions (e.g., temperature, differential stress, grain size, etc.) remain constant.

Addressing the spatial acceleration terms in Equation A.1 is less straightforward. Near the center of a significantly thinned salt layer, wall rock contacts are roughly parallel and salt thickness is fairly uniform. However, away from the center of the weld, salt can thicken markedly toward a diapir. Salt expelled toward a diapir decelerates as streamlines diverge. Furbish (1996) estimated the magnitude of the first spatial term in Equation A.1, the acceleration with respect to distance along flow, using a modified form of Equation A.2. The limit of Equation A.2 as the change in flow thickness increases to infinity is proportional to the square of flow velocity divided by the width of the zone of flow widening or narrowing. As the salt thickness tends to zero, the spatial acceleration term also tends to zero (Figure A.1), and peaks as the square of the unaccelerated flow velocity.

$$O\left(u_x \frac{du}{dx}\right) = \frac{u^2}{2L} \left( \frac{h_1^2 - h_2^2}{h_2^2} \right) \quad (\text{A.2})$$

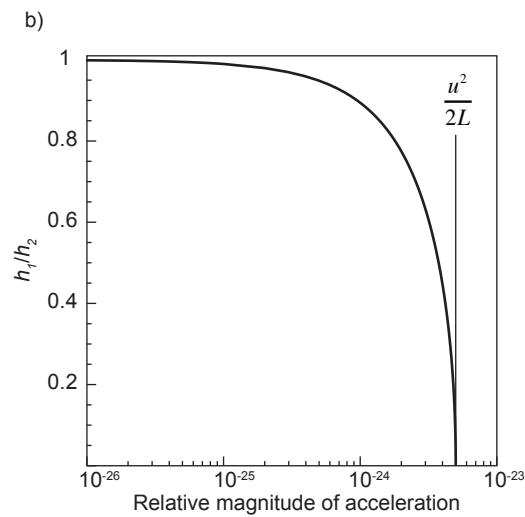
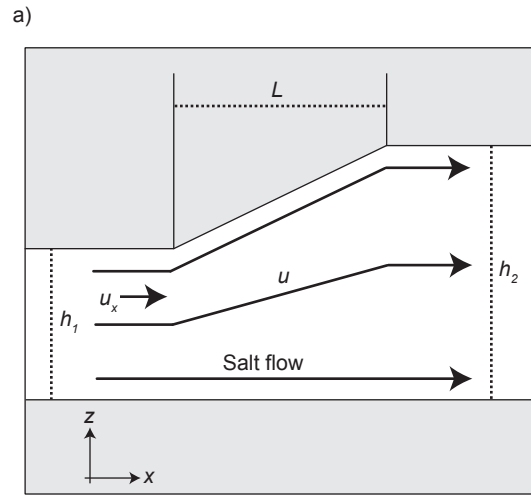


Figure A.1: a) Flow geometry illustrating streamline divergence due to salt flow out of thin salt (approximating a weld) and into thick salt. b) Order-of-magnitude estimate of the deceleration in the x-direction as streamlines diverge as salt thickness increases laterally. Deceleration tends to a small constant as the salt tends to infinite thickness. Flow velocity  $u = 10^{-10}$  m/s and flow length  $L = 10^3$  m.

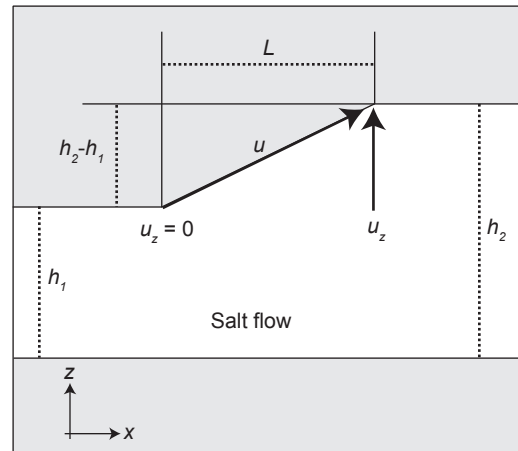
For the special case of rectilinear salt flow in a two-dimensional plane, the second spatial acceleration term is zero. For more natural geometries involving salt flow in three dimensions, consider salt evacuating radially beneath a circular minibasin. The volumetric flux past any two cylindrical surfaces must be equal to conserve volume, and therefore the third spatial acceleration in Equation A.1 (or its equivalent in cylindrical coordinates) is proportional to flow velocity squared and the inverse of flow radius (Equation A3).

$$O\left(\frac{u_\theta}{r} \frac{du_r}{d\theta} - \frac{u_\theta^2}{r}\right) = -\frac{4\pi^2 u_r^2}{r} \quad (\text{A.3})$$

The magnitude of the third spatial acceleration term in Equation A1, the change in vertical velocity can be estimated using Equation A4, and peaks at the upper boundary in the zone of widening, and approaches zero toward the “stationary” wall (Figure A.2).

$$O\left(u_z \frac{du}{dz}\right) = \frac{uz(h_1 - h_2)}{2\mu L} \left(\rho_s g_x + \frac{dp}{dx}\right) \quad (\text{A.4})$$

a)



b)

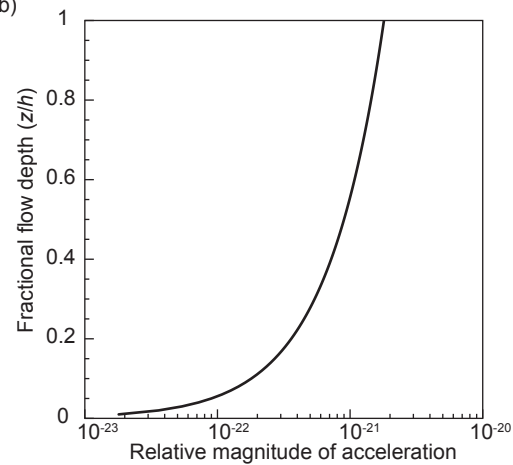


Figure A.2: a) Flow geometry illustrating streamline divergence as salt flows along the upper salt contact from a thinning area to an adjacent thick area. b) Order-of-magnitude estimate of the acceleration in the z-direction caused by streamline divergence as a function of fractional channel height. Deceleration is greatest along the diverging contact, which for salt is presumable the upper salt interface. Flow velocity  $u = 10^{-10}$  m/s and flow length  $L = 10^3$  m.

The total error caused by these spatial accelerations is the sum of these contributions. For typical salt velocities and geometries, the total error is certainly small enough to neglect. Each acceleration term is negative and will result in overestimating flow velocity and salt discharge in the models, and thus predict a thinner weld that forms more rapidly than in nature.

### NUMERICAL APPROXIMATIONS

To model salt evacuation in a fault weld over tens of millions of years, a suitable time step was chosen to ensure the stability, accuracy, and numerical efficiency of the forward difference technique. Equation 1.10 is conditionally stable and conditionally accurate (Equation A.5).

$$t \leq \frac{12\mu L}{6\mu U - h_k^2 \left( \rho g_x + \frac{\Delta p}{L} \right)} \quad (\text{A.5})$$

Error incurred during approximation is greatest early in model runs when salt is thick and flowing rapidly and becomes negligible at longer time scales and once salt has greatly thinned (Figure A.4). After multiple modeling runs and convergence analysis,  $10^3$  years was selected as a suitable time step to investigate welding in the analytical models. Because of the forward-difference approximation, the volumetric flux of salt at each time step was overestimated and the final remnant salt thickness has been underestimated.

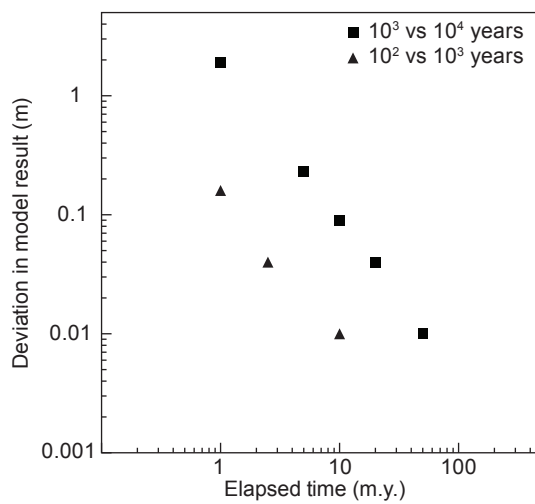


Figure A.3: Numerical error due to time-step size in the forward-difference method used to model salt evacuation between parallel plates having shear displacement (Equation 1.10). Decreasing the time step by an order of magnitude increases the computational time and the resulting accuracy by an order of magnitude. However, using a time step of 103 compared with 104 results in deviations less than 1 m at 1 m.y. elapsed time, which is suitable for modeling. Increasing model time also decreases the error caused by long time steps.

## Appendix B: Viscous Flow MATLAB Code 1

The following code was written in MATLAB 7.6.0.324 (R2008a) by the author to model viscous flow during salt welding for a pure salt layer. Input parameters are defined at the beginning of the code, and then used to define functions *brenner* and *gnoevoi* as input for `ode15s`, a built-in solver designed to handle stiff differential equations. Each function was programmed with three options. The first equation is the standard form included in Equation 1.15 and Equation 2.16. The second equation incorporates thickening of the minibasins during salt expulsion (Equation 1.17 and Equation 1.18) and the third equation incorporates thickening and compaction of the minibasin using the compaction function provided in Hudec et al. (2009) based on Gulf of Mexico well data. The results are then plotted. The function returns as output *b* and *g*, are  $n$  rows  $\times$  4 columns matrix, where  $n$  is the number of time steps used by the solver. Column 1 is the elapsed time in seconds, column 2 is salt thickness, column 3 is the instantaneous rate of change of salt thickness, and column 4 is the elapsed time in millions of years. MATLAB code preceded by percentage signs are used for commenting and are not compiled. Models were run on a MacBook Pro laptop running OSX v. 10.5.8 with a 2.2 GHz Core 2 Duo processor.

To run this MATLAB code, input the desired setup parameters, uncomment the desired equations (by deleting the leading percentage sign as described above) and save the code as a MATLAB m-file (`ODESaltEvacuation.m` extension). Change the MATLAB working directory to the directory where the m-file is stored, and type the following into the command prompt and press enter.

```
>> [b, g] = ODESaltEvacuation();
```

```

function [b,g] = ODESaltEvacuation()

%%MATLAB code to model viscous flow during salt evacuation
%%Written by Bryce H Wagner III, 6/1/2009
%%Release Candidate 1.0d, Edited February 26, 2010

%%Model Parameters
mu = 1e18; %Dynamic Viscosity (Pa-s)
rhos = 2200; %Salt Density (kg/m3)
rhor = 2210; %Overburden Density (kg/m3)
gravity = 9.80655; %Gravitational Acceleration (m/s2)
r = 1000; %Radius (m)
s1 = 4000; %Initial Rock Thickness (m, for Gnoevi Plates)
s2 = 4000; %Initial Rock Thickness (m, optional for Brenner Sphere)
h0 = 1000; %Initial Salt Thickness
tspan = [0, 3.15576E13*200]; %Time Duration in seconds (3.15576E16 s = 1 b.y.)
v = 0; %Initial Velocity 100m, 1500 Pa/m, 1000m, 1e17 Pa-s, -
1.25*10^-12
y0 = [h0; v]; %Initial Value Problem Inputs
xlimit = tspan(2)/3.15576E13; %X Axis Scale (in m.y.)
ylimit = h0; %Y Axis Scale (in meters)
options = odeset('RelTol',1e-6,'AbsTol',1e-12,'NonNegative',1); %ODE options

%%Call ODE Solver and Define Output
[tb,yb] = ode15s(@brenner,tspan,y0,options);
[tg,yg] = ode15s(@gnoevoi,tspan,y0,options);

b = horzcat(tb,yb);
g = horzcat(tg,yg);

%%Convert Time to m. y.
b(:,4) = b(:,1)/(365.25*60*60*24*1000000);
g(:,4) = g(:,1)/(365.25*60*60*24*1000000);

%%Define Functions
%Brenner Sphere Deceleration (Uncomment desired function)
function dydt = brenner(t,y)

%Standard Calculation (Equation 2.15)
%dydt = [y(2); -(9*mu*y(2))/(y(1)*r^2*rhor)+(rhos-rhor)*gravity/rhor];

%Standard Calculation + Thickening(Equation 2.17)
%dydt = [y(2); -(6*pi*mu*y(2))/(y(1)*(2/3*pi*r^2+pi*r*(s2+(h0-y(1))))*rhor)+(rhos-rhor)*gravity/rhor];

%Standard Calculation + Thickening + Compaction
%dydt = [y(2); -(6*pi*mu*y(2))/(y(1)*(2/3*pi*r^2+pi*r*(s2+(h0-y(1))))*rhor)+(rhos-rhor)*gravity/rhor];

end

%Gnoevoi Plate Deceleration (Uncomment desired function)
function dydt = gnoevi(t,y)

```

```

%Standard Calculation (Equation 2.16)
%dydt = [y(2); -(3/2*mu*r^2)/(((s1)*rhor)*y(2)/(y(1)^3)+(rhos-rhor)*gravity/rhor)];

%Standard Calculation + Thickening(Equation 2.18)
dydt = [y(2); -(3/2*pi*mu*r^4)/((pi*r^2*(s1+(h0-y(1))))*rhor)*y(2)/(y(1)^3)+(rhos-rhor)*gravity/rhor];

%Standard Calculation + Thickening + Compaction
dydt = [y(2); -(3/2*pi*mu*r^4)/((pi*r^2*(s1+(h0-y(1))))*(1400+142*(s1+(h0-
y(1)))^0.21))*y(2)/y(1)^3+(rhos-(1400+142*(s1+(h0-
y(1)))^0.21))*gravity/(1400+142*(s1+(h0-      y(1)))^0.21)];

end

%%Plot solutions
figure (1)
plot(b(:,4),b(:,2),'-');
xlim([0 tspan(2)/(1000000*365.25*60*60*24)-(tspan(2)/(1000000*365.25*60*60*24)-xlimit)]);
ylim([0 ylimit]);
title('Brenner Spherical Deceleration');
xlabel('Time (m.y.)');
ylabel('Salt Thickness (m)')

figure (2)
plot(g(:,4),g(:,2),'-');
xlim([0 tspan(2)/(1000000*365.25*60*60*24)-(tspan(2)/(1000000*365.25*60*60*24)-xlimit)]);
ylim([0 ylimit]);
title('Gnoevoi Plate Deceleration');
xlabel('Time (m.y.)');
ylabel('Salt Thickness (m)')

min(g(:,2,,:))

end

```

## Appendix C: Viscous Flow MATLAB Code 2

The following code was written in MATLAB 7.6.0.324 (R2008a) by the author to model viscous flow during salt welding for multilayered evaporites. The code is designed to model evacuation of 10 layers with varying viscosity and thickness but can be used to model fewer layers by setting the layer thickness to zero. The user defines layer thickness, layer viscosity, elapsed time and time step, flow length, flow stress, and initial shear displacement velocity at the beginning of the code. The integer *refine* determines the vertical resolution of the calculations and the output; the number of vertical sampling points is equal to *refine* multiplied by the thickness of the sequence in meters. These parameters are then used to model viscous flow of the layered sequence. Each modeling step is divided into two parts. First, the constants of integration for the system of equations defined by Equation 2.21 are solved using symbolic notation and then used to calculate the velocity throughout the sequence. Second, the velocity function  $u$  is integrated using the built-in quadrature function *quadgk* to calculate the volume (area) of salt expelled during each time step. The function returns *output*, an  $n \times 12$  matrix where  $n$  is the number of time steps and *vout*, an  $m \times 2 \times n$  matrix where  $m$  is the vertical resolution defined as above. Column 1 of *output* is elapsed time in millions of years, column 2 is total salt thickness, and columns 3 - 12 are the thicknesses of the individual layers. Column 1 of *vout* is vertical position within the layered sequence in meters, and column 2 is velocity in meters per second. Models were run on a MacBook Pro laptop running OSX v. 10.5.8 with a 2.2 GHz Core 2 Duo processor.

```

function [output, vout] = LayersInTime()

%%Layered Evaporites Through Time
%%Written by Bryce H Wagner III, 6/22/2009
%%Release Candidate 1.0d, Edited February 26, 2010

format long e

%%Input Parameters
%Dynamic Viscosity (Pa-s)
mu1 = 1e21;
mu2 = 1e23;
mu3 = 1e22;
mu4 = 1e23;
mu5 = 1e22;
mu6 = 1e23;
mu7 = 1e22;
mu8 = 1e23;
mu9 = 1e22;
mu10 = 1e21;

mu = [mu1;mu2;mu3;mu4;mu5;mu6;mu7;mu8;mu9;mu10];

%Layer Thicknesses (m)
% Note: Non-integers may cause problems.
thick1=80;
thick2=70;
thick3=20;
thick4=120;
thick5=50;
thick6=60;
thick7=200;
thick8=75;
thick9=85;
thick10=0;

%Cumulative Thicknesses - DO NOT EDIT
h1 = thick1;
h2 = h1+thick2;
h3 = h2+thick3;
h4 = h3+thick4;
h5 = h4+thick5;
h6 = h5+thick6;
h7 = h6+thick7;
h8 = h7+thick8;
h9 = h8+thick9;
h10 = h9+thick10;
h = [h1;h2;h3;h4;h5;h6;h7;h8;h9;h10];

```

```

Vmmperyear=0.2; %Shear displacement velocity
(mm/year)
Vmpers=(Vmmperyear/(60*60*24*365.25*1000));
L = 1000; %Flow Length (m)
Pa = 1000000; %Flow Stress (Pa)
P = -Pa/L; %Hydraulic Gradient
telapsed = 365.25*24*60*60*1000000*200; %Elapsed Time (s)
tstep = 365.25*24*60*60*1000000;
refine=10; %Refinement Parameter
Bsize=(size(h(:,1),1)-1);

output=zeros(telapsed/tstep+1,size(h(:,1))*2+1);
vout=zeros(h(10)*refine+1,2,size(output,1));

%%Modeling Code
for i=1:size(h(:,1))
    if i==1
        layer(i)=h(i);
    else
        layer(i)=h(i)-h(i-1);
    end
end

for t=0:tstep:telapsed

    B = sym(zeros(Bsize,1));

    for i=2:size(h,1)

        BTEST = sym('BTEST');
        A = sym('A');

        if i==2
            C = solve( h(i-1)^2*1/2*P*1/mu(i-1) + A*h(i-1)/mu(i-1) - h(i-1)^2*1/2*P*1/mu(i) - A*h(i-1)/mu(i) - BTEST/mu(i) );
        else
            C = solve( h(i-1)^2*1/2*P*1/mu(i-1) + A*h(i-1)/mu(i-1) + B(i-2)/mu(i-1) - h(i-1)^2*1/2*P*1/mu(i) - A*h(i-1)/mu(i) - BTEST/mu(i) );
        end

        B(i-1)=vpa(C);

    end

    A = solve( h(9)^2*P*1/2*1/mu(9) + A*h(9)/mu(9) + B(Bsize)/mu(9) - Vmpers - h(9)^2*1/2*P*1/mu(10) - A*h(9)/mu(10) + A*h(10)/mu(10) + h(10)^2*P*1/2*1/mu(10));

    A = eval(A);
    B = eval(B);

```

```

u=@velocity;

v = zeros(h10*refine,2); %Velocity Array

for k=1:h10*refine+1
    v(k,1)=feval(u,(k-1)/refine);
    v(k,2)=(k-1)/refine;
end

output(t/tstep+1,:) = [t/(1000000*365.25*60*60*24);h;layer]';
vout(:,t/tstep+1) = [v];

for s=10:-1:1
    if s==1
        q=quadgk(u,0,h(s));
        layer(s)=h(s)-tstep/L*q;
    else
        q=quadgk(u,h(s-1),h(s));
        layer(s)=((h(s)-h(s-1))-tstep/L*q);
    end
end

for j=1:10
    h(j)=sum(layer(1:j));
end

Percent = t/telapsed*100      %Print Percent Complete

end

function f = velocity(y)
    I1 = (0 <= y) & (y < h(1));
    I2 = (y >= h(1)) & (y < h(2));
    I3 = (y >= h(2)) & (y < h(3));
    I4 = (y >= h(3)) & (y < h(4));
    I5 = (y >= h(4)) & (y < h(5));
    I6 = (y >= h(5)) & (y < h(6));
    I7 = (y >= h(6)) & (y < h(7));
    I8 = (y >= h(7)) & (y < h(8));
    I9 = (y >= h(8)) & (y < h(9));
    I10= (y >= h(9)) & (y <= h(10));
    I0 = ~I1 & ~I2 & ~I3 & ~I4 & ~I5 & ~I6 & ~I7 & ~I8 & ~I9 & ~I10;

f = y;
f(I1) = (y(I1).^2/2*P+A*y(I1))*1/mu(1);
f(I2) = (y(I2).^2/2*P+A*y(I2)+B(1))*1/mu(2);
f(I3) = (y(I3).^2/2*P+A*y(I3)+B(2))*1/mu(3);
f(I4) = (y(I4).^2/2*P+A*y(I4)+B(3))*1/mu(4);
f(I5) = (y(I5).^2/2*P+A*y(I5)+B(4))*1/mu(5);
f(I6) = (y(I6).^2/2*P+A*y(I6)+B(5))*1/mu(6);

```

```
f(l7) = (y(l7).^2/2*P+A*y(l7)+B(6))*1/mu(7);  
f(l8) = (y(l8).^2/2*P+A*y(l8)+B(7))*1/mu(8);  
f(l9) = (y(l9).^2/2*P+A*y(l9)+B(8))*1/mu(9);  
f(l10) = (y(l10).^2/2*P+A*y(l10)-Vmpers-A*h(10)-h(10)^2/2*P)*1/mu(10);  
f(l0) = 0;  
end  
  
end
```

## Appendix D: Synthetic Seismogram MATLAB Code

The following code was written in MATLAB 7.6.0.324 (R2008a) by the author to produce one-dimensional synthetics to characterize the seismic response of evaporite welds. The user defines record length, sampling interval, reflection coefficients of the evaporite layer, peak frequency of the wavelet, depth to the top of the evaporite layer, the thickness range of interest, and the increment thickness at the beginning of the code. Next, a zero-phase Ricker wavelet is created and convolved with a reflection series corresponding to the top and base of the evaporites and then manipulated to obtain output information and for plotting. The function returns  $R$ , an  $n \times 6$  matrix where  $n$  is the number of model steps (*thickrange/increment*) and  $S$ , an  $m \times 2$  matrix where  $m$  is the value of *size $x$* , the total length of the synthetic record after processing. Column 1 of  $R$  contains the approximate apparent thickness in milliseconds, column 2 contains the approximate apparent thickness in meters, column 3 contains the true thickness in milliseconds, column 4 contains true thickness in meters, column 5 contains the maximum positive amplitude of the synthetic, and column 6 contains the maximum negative amplitude of the synthetic. Column 1 of  $S$  contains the vertical depth in milliseconds and column 2 contains the amplitude of the synthetic.  $R$  is designed to help create plots of apparent thickness and amplitude versus true thickness, but obtaining apparent thickness is not straightforward and the results should be vetted when the reflection coefficients are of the same sign (Type II and Type III welds) or for reflection coefficient ratios greater than 2. Models were run on a MacBook Pro laptop running OSX v. 10.5.8 with a 2.2 GHz Core 2 Duo processor.

```

%% 1D Synthetic Program
%%Written By Bryce Wagner
%%Release Candidate 1.0d, Edited February 27, 2010

%%Model Setup and Input Parameters
recordlength=0.5; %Length of Synthetic (s)
dt=0.00005; %Sampling Interval (s)
sizex=recordlength/dt+1;

%Define Salt Layer
topR = 0.5; %Upper Reflection Coefficient
baseR = -0.5; %Lower Reflection Coefficient

%Create Wavelet For Convolution
frequency=50; %Peak Frequency (Hz)
w = ricker(sizex-1,frequency,dt);

%Loop Conditions
topsalt = 300; %TWTT depth of Topsalt (ms)
thickrange = 80; %Thickness range being investigated
(ms)
increment = 0.5; %Thickness increment (ms)
steps = thickrange/increment;
R = zeros(steps,6);

%%Create Synthetics
for g=1:1:steps

    %Initialize Variables Inside Loop
    synth=zeros(sizex,1)'; %Create matrix to store time and amplitude information
    basesalt = topsalt+increment*g; %Calculate Base of Salt (ms)

    %Create Spike In Data
    topsaltcount = topsalt * 0.001 / dt + 1;
    basesaltcount = basesalt * 0.001 / dt + 1;

    synth(int64(topsaltcount)) = topR;
    synth(int64(basesaltcount)) = baseR;

    %Convolve
    convolved = conv(w,synth);

    %Resample for Plot
    resample = convolved(size(w,2)/2+1:size(w,2)/2+sizex);

    %Concatenate for True Scale
    synthetic = zeros(size(resample,2),2);

    for h=1:1:size(resample,2)
        synthetic(h,1) = (h-1)/(0.001/dt);
    end
end

```

```

synthetic(:,2) = resample';

if topR >= 0 && baseR >=0

synthsort = sortrows(synthetic,2);
  ApparentThickness = abs(synthsort(1,1) - synthsort(size(synthsort,1)-1,1));
  TrueThickness = abs(basesalt - topsalt);
  ApparentSaltThickness = 2.250 * ApparentThickness;
  TrueSaltThickness = 2.250 * TrueThickness;
  PeakAmplitude = [synthsort(size(synthsort,1),2) synthsort(size(synthsort,1)-1,2)];

else
  [Cmax,lmax] = max(synthetic);
  [Cmin,lmin] = min(synthetic);

  ApparentThickness = abs(synthetic(lmax(2),1)-synthetic(lmin(2),1));
  TrueThickness = abs(basesalt-topsalt);
  ApparentSaltThickness = 2.250*ApparentThickness;
  TrueSaltThickness = 2.250*TrueThickness;
  PeakAmplitude = [Cmax(2) Cmin(2)];

end

R(g,:) = [ApparentThickness ApparentSaltThickness TrueThickness TrueSaltThickness
PeakAmplitude(1) PeakAmplitude(2) ]; % peakfreq];
S = synthetic;
disp(g/steps*100)
disp('percent complete')

end

hold off
figure(1)
plot(synthetic(:,2),synthetic(:,1));
hold on
plot([-1,1],[topsalt,topsalt]);
plot([-1,1],[basesalt,basesalt]);
set(gca,'YDir','reverse')
title('Synthetic Seismogram')
xlabel('Amplitude')
ylabel('TWTT (ms)')

function [r] = ricker(sizewavelet,freq,dt)           %Wavelet Function

t = -dt*sizewavelet/2+dt : dt : dt*sizewavelet/2;
r = (1-2*pi^2*freq^2*t.^2).*exp(-pi^2*freq^2*t.^2);

end
end

```

## Appendix E: Synthetic Seismogram MADAGASCAR Code

MADAGASCAR v0.98 is a parallel open-source mathematics package developed by geophysicists in the Bureau of Economic Geology at the University of Texas at Austin. MADAGASCAR uses a series of built-in functions and programs that are called through an SConstruct file written as a python script. The SConstruct file included below was used to create two-dimensional seismic synthetics and originally created by Will Burnett, a Ph. D. candidate in the Jackson School of Geosciences and then adapted to the purposes of my dissertation. Shooting and acquisition parameters are specified at the beginning of the code, as well as the model geometry. Geometry is defined by interfaces that separate domains with varying density and p-wave velocity, and each of the points in *layers* is then interpolated using a cubic spline. The model geometry is then passed to the MADAGASCAR program *sfawefd*, which models the acoustic wavefield using finite-difference techniques. The data are then migrated to depth using source-receiver functions and the resulting images are stacked to produce the final image, which is stored as *saltimage.vpl* and can be manipulated using plot programs within MADAGASCAR. The model geometry is stored as *mod1.vpl* (velocity model) and *den1.vpl* (density model).

Models were run on the COREEARTH cluster at the Bureau of Economic Geology using 32 nodes and 8 processing cores per node. For more information or to install MADAGASCAR for your own work, visit <http://www.ahay.org>

NOTE: Loops and conditional statements in Python scripts depend critically on the degree to which lines are indented. If this code is copied for use in MADAGASCAR, it is highly recommended indentations are verified to avoid errors.

```

from rsfproj import *
from math import *

####
##Salt Weld Experiment
####

##### Parameter List #####
par = {
    'nx':2401, 'dx':0.01, 'ox':0,          # horizontal (km)
    'nz':1001, 'dz':0.01, 'oz':0,       # depth (km)
    'nt':2501, 'dt':0.004, 'ot':0,      # time (s)
    'ntfd':10001, 'dtfd':0.001,
    'os':0, 'js':20,                    # shot positions (km)
    'or':0, 'jr':1,                    # receiver positions (km)
    'nw':128, 'jw':1, 'ow':1,          # frequency
    'wvltfreq':10
}

par['ds'] = par['dx']*par['js']
par['dr'] = par['dx']*par['jr']
par['ns'] = int((par['nx']-1)/par['js'])
par['nr'] = int((par['nx']-1)/par['jr'])
par['dh'] = par['dr']/2.0
par['tr'] = int(par['dt']/par['dtfd'])

print par['ds']
print par['ns']
#####

##### Create Velocity Model
#####
## Survey boundaries
xmax = (par['nx']-1)*par['dx']
zmax = (par['nz']-1)*par['dz']

## Layer interface z-coordinates.
## ( Corresponding x-coordinates are equally spaced from 0 to xmax.)
layers = ((3.0, 3.0, 3.0, 3.0, 3.0, 3.0, 3.0, 3.0, 3.0, 3.0),
          (6.5, 6.5625, 6.6250, 6.6875, 6.7500, 6.8125, 6.8750, 6.9375, 7.0, 7.0),
          (7.0, 7.0, 7.0, 7.0, 7.0, 7.0, 7.0, 7.0, 7.0, 7.0),
          (10.0, 10.0, 10.0, 10.0, 10.0, 10.0, 10.0, 10.0, 10.0, 10.0))

## Velocities for layers between interfaces
velocities = (1.50,
              2.50,
              4.50,
              3.00)

```

```

densities = (1.00,
            2.40,
            2.25,
            2.65)

## Quick function to help with scon's rule input
def arr2str(array,sep=' '):
return string.join(map(str,array),sep)

## Grab the size of the layer array for use in model construction
n1 = len(layers[0])
n2 = len(layers)

## Construct interface grid
Flow('layers.asc',None,
    """
echo %s
n1=%d n2=%d o1=0 d1=%g
data_format=ascii_float in=$TARGET
    """ % (string.join(map(arr2str,layers),' '),
n1,n2,xmax/(n1-1)), local=1)

## Convert ASCII to binary
Flow('layers','layers.asc','dd form=native')

## Construct Velocity model :
## First, layer z-coordinates are spline-interpolated to form surfaces.
## sfunif2 is used to actually create the 2-D velocity model.

Flow('mod1','layers',
    """
spline o1=0 d1=%g n1=%d |
unif2 d1=%g n1=%d v00=%s
    """ % (par['dx'],par['nx'],
par['dz'],par['nz'],
arr2str(velocities,'')), local=1)

Flow('den1','layers',
    """
spline o1=0 d1=%g n1=%d |
unif2 d1=%g n1=%d v00=%s
    """ % (par['dx'],par['nx'],
par['dz'],par['nz'],
arr2str(densities,'')), local=1)

## Plot the velocity model
Result('mod1',
    """
grey color=j title="Velocity Model 1"
screenratio=%g screenht=7
allpos=y titlesz=8 labelsz=6

```

```

label1="Depth (km)" scalebar=y barreverse=y
label2="Distance (km)"
    "" % (zmax/xmax), local=1)

## Plot the density model
Result('den1',
    ""

grey color=j title="Density Model 1"
screenratio=%g screenht=7
allpos=y titlesz=8 labelsz=6
label1="Depth (km)" scalebar=y barreverse=y
label2="Distance (km)"
    "" % (zmax/xmax), local=1)

##### Set up sources and receivers
#####

## Specify source and receiver locations using velocity model
Flow('rz','mod1','window squeeze=n n1=1 j2=%d | math output=.01' % par['jr'])
Flow('rx','mod1','window squeeze=n n1=1 j2=%d | math output=x2' % par['jr'])
Flow('rxz',['rx','rz'],'cat axis=1 space=n ${SOURCES[0]} ${SOURCES[1]}' , stdin=0, local=1)

Flow('sz','mod1','window squeeze=n n1=1 j2=%d | math output=.01' % par['js'])
Flow('sx','mod1','window squeeze=n n1=1 j2=%d | math output="x2"' % par['js'])
Flow('sy','mod1','window squeeze=n n1=1 j2=%d | math output=0' % par['js'])
Flow('sxz',['sx','sz'],'cat axis=1 space=n ${SOURCES[0]} ${SOURCES[1]} | transp',stdin=0,
local=1)

## Create source wavelet
Flow('wavelet',None,
    ""

spike nsp=1 n1=%(ntfd)d d1=%(dtfd)g k1=201 |
ricker1 frequency=%(wvltfreq)g | transp
    "" % par)

## Result('wavelet','wiggle')

## Subsample to Migration wavelet
Flow('wvlt','wavelet',
    ""

transp plane=12 |
window squeeze=y n1=%(nt)d f1=0 j1=%(tr)d |
put d1=%(dt)g
    "" % par)

# Prepare migration slowness
Flow('smod','mod1',
    ""

window | math output="1/input" |
transp |
spray axis=2 n=1 d=1. o=0 |

```

```

put label2=y unit2=""
    "")

##### Acoustic Finite Difference Modelling
#####
shotlist=[]
imglist=[]

for i in range(par['ns']):
    srci='sxz'+str(i)
    shoti='data'+str(i)
    par['xS']=float(i)*par['ds']
    shotlist.append(shoti)
        par['h0']=(par['or']-par['xS'])
    Flow(srci,'sxz','window n1=1 f1=%d squeeze=y' % i)

        ##### Acquire the i-th shot. #####
    Flow(shoti,['wavelet','mod1','den1',srci,'rxz'],
        ""

awefd
verb=y free=n snap=n nb=100
vel=${SOURCES[1]}
den=${SOURCES[2]}
sou=${SOURCES[3]}
rec=${SOURCES[4]} |
    transp |

put
label1=Time unit1=s
label2=Position unit2=km
label3=Shot unit3=km
    "" % par)
#####
# Prepare wavefields from data for migration.
par['iS'] = i

# FFT and setting coordinates
rfft='rfft'+str(i)
sfft='sfft'+str(i)
Flow(rfft,shoti,
    ""

window squeeze=n n1=%(nt)d f1=0 j1=%(tr)d |
put d1=%(dt)g o2=%(h0)g d2=%(dr)g label2=Offset |
fft1 | window squeeze=n n1=%(nw)d min1=%(ow)g j1=%(jw)d |
spray axis=3 n=1 o=0 d=1 label=hy | spray axis=5 n=1 o=0 d=1 label=sy |
put n4=1 d4=1 o4=%(xs)g
    "" % par)

# w, hx, hy, sx, sy
Flow(sfft,'wvlt',
    ""

```

```

fft1 | window squeeze=n n1=%(nw)d min1=%(ow)g |
put label1=w n2=1 o2=%(xS)g d2=1
    "" % par)

allrwv='allrwv'+str(i)
allswv='allswv'+str(i)
Flow([allrwv, allswv],[rfft, sfft], 'srsyn verb=y nx=%(nx)d dx=%(dx)g ox=%(ox)g
wav=${SOURCES[1]} swf=${TARGETS[1]}' % par)
    # w, x, y, s

# Transpose
rwfl = 'rwfl'+str(i)
swfl = 'swfl'+str(i)
Flow(rwfl,allrwv,'transp plane=12 | transp plane=23')
Flow(swfl,allswv,'transp plane=12 | transp plane=23')
    # x, y, w, s

##### Migrate the i-th shot. #####
saltimage='saltimage'+str(i)
Flow(saltimage,[swfl, rwfl, 'smod'],
    ""

srmig3 readwrite=y verb=y nrmax=3 dtmax=5e-05 eps=0.1
tmx=16 itype=o verb=n slo=${SOURCES[2]} rwf=${SOURCES[1]}
    "",split=[3,par['nw'],[0,1]],reduce='add')
#####
imglist.append(saltimage)

## Save shot gathers as a dataset.
Flow('salt_dataset',shotlist,'cat ${SOURCES[1:%d]} axis=3 | window squeeze=y' % par['ns'])

## Add individually migrated shots together to form image.
Flow('saltimage',imglist,'add ${SOURCES[1:%d]} | window squeeze=y' % par['ns'])
Result('saltimage',
    ""

transp | tpow tpow=1.5 |
grey pclip=99 title=Migrated\ Image
label1=Depth unit1=km label2=Position unit2=km
screenratio=%g screenht=7
titlesz=8 labelsz=6
scalebar=y barreverse=y
    ""% (zmax/xmax), local=1)
End()

```

## Glossary

**Salt Weld** – A general term referring to any structure that results from the complete or near-complete removal of rock salt by viscous flow, dissolution, or faulting. This term can be used to refer to complete welds, partial welds, and fault welds.

**Complete Weld** - The structure joining two bodies of rock formerly separated by salt. Some combination of viscous evacuation, layer-parallel wall rock translation, and dissolution is necessary to form a complete weld, which is equivalent to the classic definition of a salt weld by Jackson and Cramez (1989).

**Partial Weld** – A region of partially thinned salt up to ~50 m thick. This threshold is based on analytical and numerical models that indicate evaporites thinner than ~50 m tend to strongly resist additional viscous evacuation (Chapter 1), but depends critically on salt viscosity, driving forces, and flow geometry.

**Fault Weld** – A salt weld formed by shear displacement of the salt contacts (see Figure 1.5). Originally defined by Hossack and McGuinness (1990).

**Seismic Weld** – The composite reflection produced by evaporites thinner than the temporal resolution of seismic data. Below the limit of temporal resolution, ~25-50 m for seismic surveys with peak frequencies of ~10-30 Hz, it is impossible to distinguish between partial and complete welds using travel time information alone (Chapter 2). Most salt welds identified in the literature would be better described as seismic welds because they were identified on seismic data and the thickness of any remnant salt is unknown.

**Evaporite Weld** – A weld that results from the removal of any evaporite-rich rocks, not just rock salt.

## References

- Alkattan, M., Oelkers, J. D., Dandurand, J.-L., and Schott, J., 1997a,  
Experimental studies of halite dissolution kinetics, 1 The effect of  
saturation state and the presence of trace metals: *Chemical Geology*, v.  
137, p. 201-219.
- Alkattan, M., Oelkers, J. D., Dandurand, J.-L., and Schott, J., 1997b,  
Experimental studies of halite dissolution kinetics: II. The effect of  
saturation state and the presence of trace metals: *Chemical Geology*, v.  
143, p. 17-26
- Anderson, R. Y., 1981, Deep-seated salt dissolution in the Delaware basin,  
Texas and New Mexico: *New Mexico Geological Society Special  
Publication 10*, p. 133-145.
- Anderson, R. Y., and Kirkland, D. W., 1980, Dissolution of salt deposits by brine  
density flow: *Geology*, v. 8, p. 66-69.
- Andrade, E. N. da C., 1910, On the viscous flow in metals, and allied  
phenomena: *Proceedings of the Royal Society of London*, v. 84, p. 1-12.
- Balkwill, H. R., 1978, Evolution of Sverdrup Basin, Arctic Canada: *American  
Association of Petroleum Geologists Bulletin*, v. 62, p. 1004-1028.

- Birch, F., 1966, Compressibility; elastic constants in Clark, S. P., Handbook of Physical Constants: Geological Society of America Memoir, v. 97, p. 97-173.
- Blundell, D. J., Karnkowski, P. H., Alderton, D. H. M., Oszecepski, S., and Kucha, H., 2003, Copper mineralization of the Polish Kupferschiefer: a proposed basement fault-fracture system of fluid flow: Economic Geology, v. 98, p. 1487-1495.
- Bosworth, W., 1981, Strain-induced preferential dissolution of halite: Tectonophysics, v. 78, p. 509-525.
- Bourbié, T., Coussy, O., Zinszner, B., 1987, Acoustics of Porous Media, 1<sup>st</sup> ed., CRC press, 334 p.
- Bredehoeft, J. D., 1988, Will salt repositories be dry?: Eos, Transactions of the American Geophysical Union, v. 69, p. 121-131.
- Bruthans, J., Fillipi, M., Gersl, M., Zare, M., Melková, J., Pazdur, A., Bosak, P., 2006, Holocene marine terraces on two salt diapirs in the Persian Gulf, Iran: age, depositional history and uplift rates: Journal of Quaternary Science, v. 21, p. 843-857.
- Bruus, H., 2008, Theoretical Microfluidics: Oxford University Press, 346 p.
- Brun, J.-P., and Mauduit, T. P.-O., 2008, Rollovers in salt tectonics: the inadequacy of the listric fault model: Tectonophysics, v. 457, p. 1-11.

- Buchanan, P. G., Bishop, D. J., and Hood, D. N., 1996, Development of salt-related structures in the Central North Sea: results from section balancing in Alsop, G. I., Blundell, D. J., and Davison, I., eds., *Salt Tectonics*, Geological Society, London, Special Publications, v. 100, p. 1-10.
- Burliga, S., 1996, Kinematics within the Klodawa salt diapir, central Poland, in Alsop, G. I., Blundell, D. J., and Davison, I., eds., *Salt Tectonics*: Geological Society, London, Special Publications, v. 100, p. 11-21.
- Burollet, P. F., 1975, Tectonique en radeaux en Angola: *Bulletin de la Société Géologique de France*, v. 17, no. 4, p. 503–504.
- Candido, A., and Cora, C. A. G., 1992, The Marlim and Albacora giant fields, Campos Basin, offshore Brazil, Halbouty, T., ed., *Giant oil and gas fields of the decade 1978-1988: American Association of Petroleum Geologists Memoir*, v. 54, p. 123-135.
- Carcione, J. M., Helle, H. B., and Gangi, A. F., 2006, Theory of borehole stability when drilling through salt formations: *Geophysics*, v. 71, p. F31-F47.
- Carmichael, R. S., ed., 1984, *CRC Handbook of Physical Properties of Rocks*: Boca Raton, CRC Press, v. 3, 340 p.
- Carozzi, A. V., Falkenhein, F. U. H., Lucchesi, C. F., Franke, M. R., 1979, Depositional-diagenetic history of Macaé carbonate reservoirs (Albian-

- Cenomanian), Campos Basin, offshore Rio de Janeiro, Brazil: American Association of Petroleum Geologists Bulletin, v. 63, p. 429.
- Carter, N. L., and Hansen, F. D., 1983, Creep of rocksalt: Tectonophysics, v. 92, p. 275-333.
- Carter, N. L., and Heard, N. L., 1970, Temperature and rate-dependent deformation of halite: American Journal of Science, v. 269, p. 193-249.
- Carter, N., Horseman, S. T., Russell, J. E., and Handin, J., 1993, Rheology of rocksalt: Journal of Structural Geology, vol. 15, p. 1257-1271.
- Cartwright, J., Stewart, S., Clark, J., 2001, Salt dissolution and salt-related deformation of the Forth Approaches Basin, UK North Sea: Marine and Petroleum Geology, v. 18, p. 757-778.
- Casas, E., and Lowenstein, T. K., 1989, Diagenesis of saline pan halite: comparison of petrographic features of modern, Quaternary and Permian halites: Journal of Sedimentary Petrology, v. 59, p. 724-739.
- Chattervedi, L., 1986, Evaluation of dissolution for radioactive waste repositories in salt deposits: International Association of Engineering Geology Bulletin, v. 34, p. 11-14.
- Chimney, P., and Kluth, C., 2002, Evidence for low-angle, subhorizontal hanging faults in rotate fault blocks, Cabinda, offshore Angola: The Leading Edge, v. 21, p. 1084-1090.

- Christy, R. N., 1956, Creep of sodium chloride and sodium bromide at high temperature: *Acta Metallurgica*, v. 4, p. 441-443.
- Clauser C., and Huenges, E., 1995, Thermal properties of rocks and minerals, in Ahrens, T., ed., *Rock Physics and Phase Relations: a Handbook of Physical Constants*, American Geophysical Union Reference Shelf Series, v. 3, p. 105-126.
- Cobbold, P. R., Szatmari, P., Demercian, L. S., Coelho, D., Rossello, E. A., 1995, Seismic and experimental evidence for thin-skinned horizontal shortening by convergent radial gliding on evaporites, deep-water Santos Basin, Brazil, in Jackson, M. P. A., Roberts, D. G., and Snelson, S., eds., *Salt Tectonics: a global perspective*: American Association of Petroleum Geologists Memoir, v. 65, p. 29-40.
- Cohen, H. A., and Hardy, S., 1996, Numerical modelling of stratal architectures resulting from differential loading of a mobile substrate, in Alsop, G. I., Blundell, D. J., and Davison, I., eds., *Salt Tectonics*, Geological Society, London, Special Publications, v. 100, p. 265-273.
- Cotton, J. T., and Koyi, H. A., 2000, Modeling of thrust fronts above ductile and frictional detachments: application to structures in the Salt Range and Potwar Plateau, Pakistan: *Geological Society of America Bulletin*, v. 112, p. 351-363.

Cox, R. G., and Brenner, H., 1967, The slow motion of a sphere through a viscous fluid towards a plane surface-II Small gap widths, including inertial effects: *Chemical Engineering Science*, v. 22, p. 1753-1777.

Davis, D. M., and Engelder, T., 1985, The role of salt in fold-and-thrust belts: *Tectonophysics*, 119, p. 67-88.

Davison, I., 2009, Faulting and fluid flow through salt, *Journal of the Geological Society of London*, v. 166, p. 205-216.

Davison, I., Alsop, I., Blundell, D., 1996a, Salt tectonics: some aspects of deformation mechanics, in Alsop, G. I., Blundell, D. J., and Davison, I., eds., *Salt Tectonics*, Geological Society, London, Special Publications, v. 100, p. 1-10.

Davison, I., Bosence, D., Alsop, G. I., and Al-Aawah, M. H., 1996b, Deformation and sedimentation around active Miocene salt diapirs on the Tihama Plain, northwest Yemen, in Alsop, G. I., Blundell, D. J., and Davison, I., eds., *Salt Tectonics*, Geological Society, London, Special Publications, v. 100, p. 23-39.

Diegel, F. A., Karlo, J. F., Schuster, D. C., Shoup, R. C., and Tauvers, P. R., 1995, Cenozoic structural evolution and tectono-stratigraphic framework of the northern Gulf Coast continental margin, in Jackson, M. P. A., Roberts,

- D. G., and Snelson, S., eds., Salt Tectonics: A Global Perspective:  
American Association of Petroleum Geologists Memoir, v. 65, p. 109-151.
- Dix, O. R., and Jackson, M. P. A., 1982, Lithology, microstructures, fluid  
inclusions, and geochemistry of rock salt and the cap-rock contact in  
Oakwood Dome, east Texas; significance for nuclear waste storage:  
Report of Investigations, no. 120, Bureau of Economic Geology, The  
University of Texas at Austin, 59 p.
- Dobrin, M. B., 1941, Some quantitative experiments on a fluid salt dome model  
and their geological implications: EOS, Transactions of the American  
Geophysical Union, vol. 22, p. 528-542.
- Dooley, T., Jackson, M. P. A., and Hudec, M. R., 2009, Inflation and deflation of  
deeply buried salt stocks during lateral shortening: Journal of Structural  
Geology, v. 31, p. 582-600.
- Downey, M. W., 1984, Evaluating seals for hydrocarbon accumulations:  
American Association of Petroleum Geologists Bulletin, v. 68, p. 1752-  
1762.
- Dutton, D. M., and Trudgill, B. D., 2009, Four-dimensional analysis of the Sembo  
relay system, offshore Angola: implications for fault growth in salt-  
detached settings: American Association of Petroleum Geologists Bulletin,  
v. 93, p. 763-794.

- Duval, B. C., Cramez, C., and Jackson, M. P. A., 1992, Raft tectonics in the Kwanza Basin, Angola: *Marine and Petroleum Geology*, v. 9, p. 389-404.
- Dyson, I. A., and Rowan, M. G., 2004, Geology of a welded diapir and flanking mini-basins in the Flinders Ranges of South Australia in Post, P. J., Olson, D. L., Lyons, K. T., Palmes, S. L., Harrison, P. F., and Rosen, N. C., eds., *Salt-sediment interactions and hydrocarbon prospectivity: concepts, applications, and case studies for the 21st century*, 24th Annual Gulf Coast Section Society of Economic Paleontologists and Mineralogists Foundation Bob F. Perkins Research Conference, p. 40–54.
- Escher, B. G., and Kuenen, H., 1929, Experiments in connection with salt domes: *Leidsche Geologische Mededeelingen*, v. 3, p. 151-182.
- Evans, H. T., 1979, The thermal expansion of anhydrite to 1000° C, *Physics and Chemistry of Minerals*, v. 4, p. 77-82.
- Fokker, P. A., Urai, J. L., and Steeneken, P. V., 1995, Production-induced convergence of solution mined caverns in magnesium salts and associated subsidence, in Barends, F. B. J., Brouwer, F. J. J., and Schröder, F. H., eds., *Land subsidence. Natural causes, measuring techniques, the Groningen gas field: Proceedings of the Fifth International Conference on Land Subsidence*, Den Haag, Netherlands, p. 281-289.

- Ford, D. C., and Williams, P., 1989, Karst Geomorphology and Hydrology, Unwin Hayman, London, 601 p.
- Furbish, D. J., 1996, Fluid physics in geology: Oxford University Press, 476 p.
- Gansser, A., 1960, Über Schlammvulkane und Salzdome: Naturforschende Gesellschaft in Zürich Vierteljahrsschrift, v. 105, p. 1-46.
- Gardner, G. H. F., Gardner, L. W., and Gregory, A. R., 1974, Formation velocity and density—the diagnostic basics for stratigraphic traps, Geophysics, v. 4, p. 770-780.
- Gavrieli, I., Starinsky, A., and Bein, A., 1989, The solubility of halite as a function of temperature in the highly saline Dead Sea brine: Limnology and Oceanography, v. 34, p. 1224-1234.
- Ge, H., and Jackson, M. P. A., 1998, Physical modeling of structures formed by salt withdrawal: implications for deformation caused by salt dissolution: American Association of Petroleum Geologists Bulletin, v. 82, p. 228-250.
- Ge, H., Jackson, M. P. A., and Vendeville, B. C., 1997, Kinematics and dynamics of salt tectonics driven by progradation: American Association of Petroleum Geologists Bulletin, v. 81, p. 398-423.
- Giles, K. A., and Lawton, T. F., 1999, Attributes and evolution of an exhumed salt weld, La Popa basin, northeastern Mexico: Geology, v. 27, p. 323-326.

Gottschalk, R. R., Anderson, A. V., Walker, J. D. and Da Silva, J. C., 2004, Modes of shortening salt tectonics in Angola Block 33, Lower Congo basin, West Africa in Post, P. J., Olson, D. L., Lyons, S. L., Palmes, P. F., Harrison, P. F., and Rosen, N. C., eds., Salt-sediment interactions and hydrocarbon prospectivity: concepts, applications, and case studies for the 21st century, 24th Annual Gulf Coast Section Society of Economic Paleontologists and Mineralogists Foundation Bob F. Perkins Research Conference, p. 705-734.

Gnoevoi, A. V., Klimov, D. M., Petrov, A. G., and Chesnokov, V. N., 1996, Viscoplastic flow between two approaching or parallel circular plates: Fluid Dynamics, v. 31, p. 6-13.

Griggs, D., 1940, Experimental flow of rocks under conditions favoring recrystallization: Geological Society of America Bulletin, v. 51, p. 1001-1022.

Guardado, L. R., Gamboa, L. A. P., and Lucchesi, C. F., 1989, Petroleum geology of the Campos Basin, a model for a producing Atlantic-type basin, Edwards, J. D., and Santogrossi, P. A., eds., Divergent/Passive Margin Basins: American Association of Petroleum Geologists Memoir, v. 48, p. 3-79.

Guardado, L. R., Spadini, A. R., Brandão, J. S. L., and Mello, M. R., 2000, Petroleum system of the Campos Basin, Brazil, in Mello, M. R., and Katz,

- B. J., eds., Petroleum systems of South Atlantic margins, American Association of Petroleum Geologists Memoir, v. 73, p. 317-324.
- Guerrero, J., Gutiérrez, F., and Lucha, P, 2008, Impact of halite dissolution subsidence on Quaternary fluvial terrace development: case study of the Huerva River, Ebro Basin, NE Spain: *Geomorphology*, v. 100, p. 164-179.
- Guillopé, M., and Poirier, J. P., 1979, Dynamic recrystallization during creep of single-crystalline halite: an experimental study, *Journal of Geophysical Research*, v. 84, p. 5557-5567.
- Gussow, W. C., 1968, Salt diapirism: importance of temperature and energy source of emplacement, Braunstein, J., O'Brien, G. D., eds., *Diapirs and diapirism: American Association of Petroleum Geologists Memoir*, v. 8, p. 16-52.
- Habermehl, M. A., 1980, The Great Artesian Basin, Australia, *BMR: Journal of Australian Geology and Geophysics*, v. 5, p. 9-38.
- Hall, S. H., 2002, The role of autochthonous salt inflation and deflation in the northern Gulf of Mexico: *Marine and Petroleum Geology*, v. 19, p. 649-682.
- Hardie, L. A., 1967, The gypsum-anhydrite equilibrium at one atmosphere pressure, *The American Mineralogist*, v. 52, p. 171-200.

- Harrison, J. C., and Jackson, M. P. A., 2008, Bedrock geology, Strand Fiord-Expedition Fiord area, western Axel Heiberg Island, northern Nunavut (parts of NTS 59E, F, G, and H): Geological Survey of Canada, Open File, 5590, CD-ROM.
- Hocott, C. R., 1938, Interfacial tension between water and oil under reservoir conditions: American Institute of Mining Metallurgical and Petroleum Engineers Petroleum Transactions, v. 32, p. 184-190.
- Höfer, K. H., 1958, The principles of creep in rock salt and their general significant to mining engineering: International Strata Control Congress, Leipzig, 1958, Deutsche Akademie der Wissenschaften, Berlin, Sektion Bergbau, p. 49-63.
- Hossack, J. R., 1995, Geometric rules of section balancing for salt structures, in Jackson, M. P. A., Roberts, D. G., and Snelson, S., eds., Salt Tectonics: a global perspective: American Association of Petroleum Geologists Memoir, v. 65, p. 29-40.
- Hossack, J. R. and D. B. McGuinness, 1990, Balanced sections and the development of fault and salt structures in the Gulf of Mexico: Geologic Society of America, Abstracts with Programs, v. 22, p. A48.
- House, W. M., and Pritchett, J. A., 1995, Fluid migration and formation pressures associated with allochthonous salt sheets in the northern Gulf of Mexico,

- in Travis, C. J., Harrison, H., Hudec, M. R., Vendeville, B. C., Peel, F. J., and Perkins, B. F., eds., Salt, Sediment and Hydrocarbons, 16<sup>th</sup> Annual Research Conference Gulf Coast Section Society of Economic Paleontologists and Mineralogists, p. 121-124.
- Hudec, M. R., and Jackson, M. P. A., 2004, Regional restoration across the Kwanza Basin, Angola; salt tectonics triggered by repeated uplift of a metastable passive margin: American Association of Petroleum Geologists Bulletin, v. 88, p. 971-990.
- Hudec, M. R., and Jackson, M. P. A., 2006, Advance of allochthonous salt sheets in passive margins and orogens: American Association of Petroleum Geologists Bulletin, v. 90, p. 1535-1564.
- Hudec, M. R. and Jackson, M. P. A., 2007, Terra Infirma: Understanding salt tectonics: Earth Science Reviews, v. 82, p. 1-28.
- Hudec, M. R., Jackson, M. P. A., and Schultz-Ela, D. D., 2009, The paradox of minibasin subsidence into salt, Clues to the evolution of crustal basins: Geological Society of America Bulletin, v. 121, p. 201-221.
- Hunsche, U., and Hampel, A., 1999, Rock salt-the mechanical properties of the host rock material for a radioactive waste repository: Engineering Geology, v. 52, p. 271-291.

- Hsü, K. J., Cita, M. B., Ryan, W. B. F., 1973, The origin of the Mediterranean evaporites, in Ryan, W. B. F., Hsü, K. J., eds., Initial Reports from the Deep Sea Drilling Program, United States Government Printing Office, v. 13, p. 1203-1232.
- Ings, S. J., and Shimeld, J. W., 2006, A new conceptual model for the structural evolution of a regional salt detachment on the northeast Scotian margin, offshore eastern Canada: American Association of Petroleum Geologists Bulletin, v. 90, p. 1407-1423.
- Jackson, M. P. A., Cornelius, R. R., Craig, C. H., Gansser, A., Stöcklin, J., and Talbot, C. J., 1990, Salt diapirs of the Great Kavir, central Iran: Geological Society of America Memoir, v. 177, 139 p.
- Jackson, J. D., and Symmons, G. R., 1966, An investigation of laminar radial flow between two parallel discs: Applied Science Research, v. 15, p. 59-75.
- Jackson, M. P. A., and Seni, S. J., 1983, Geometry and evolution of salt structures in a marginal rift basin of the Gulf of Mexico, east Texas: Geology, v. 11, p. 131–135.
- Jackson, M. P. A., Schultz-Ela, D. D., Hudec, M. R., Watson, I. A., and Porter, M. L., 1998, Structure and evolution of Upheaval Dome: a pinched-off salt diapir: Geological Society of America Bulletin, v. 110, p.1547–1573.

Jackson, M. P. A., and Talbot, C. J., 1986, External shapes, strain rates, and dynamics of salt structures: Geological Society of America Bulletin, v. 97, p. 305-323.

Jackson, M. P. A., and Talbot, C. J., 1989, Anatomy of mushroom-shaped diapirs: Journal of Structural Geology, v. 11, p. 211-230.

Jackson, M. P. A., and Talbot, C. J., 1991, A Glossary of Salt Tectonics: Bureau of Economic Geology, Geological Circular 91-4, Austin, Texas, 44 p.

Jackson, M. P. A., and Cramez, C., 1989, Seismic recognition of salt welds in salt tectonics regimes, in Proceedings, 10<sup>th</sup> Annual Research Conference Gulf Coast Section of Society of Economic Paleontologists and Mineralogists, p. 66–71.

Jackson, M. P. A., Hudec, M. R., Jennette, D. C. and Kilby, R. E., 2008, Evolution of the Cretaceous Astrid thrust belt in the ultradeep-water Lower Congo Basin, Gabon: American Association of Petroleum Geologists Bulletin, v. 92, p. 487–511.

Jackson, M. P. A., Vendeville, B., and Schultz-Ela, D. D., 1994, Structural dynamics of salt systems: Annual Reviews of Earth and Planetary Sciences, v. 22, p. 93-117.

Jackson, M. P. A., Warin, O. N., Woad, G. M., and Hudec, M. R., 2003, Neoproterozoic allochthonous salt tectonics during the Lufilian orogeny in

- the Katangan Copperbelt, central Africa: Geological Society of America Bulletin, v. 115, p. 314-330.
- Johnson, K. S., 1997, Evaporite karst in the United States: Carbonates and Evaporites, v. 12, p. 2-14.
- Jordan, P. G., 1987, The deformational behaviour of bimineralic limestone-halite aggregates: Tectonophysics, v. 135, p. 185–197.
- Jowett, E. C., Cathles, L. M., Davis, B. W., 1993, Predicting depths of gypsum dehydration in evaporitic sedimentary basins: American Association of Petroleum Geologists Bulletin, v. 77, p. 402-413.
- Kallweit, R. S., and Wood, L. C., 1982, The limits of resolution of zero-phase wavelets: Geophysics, v. 47, pp 1035-1046.
- Kehle, R. O., 1988, The origin of salt structures, in Schreiber, B. C., ed., Evaporites and hydrocarbons: Columbia University Press, New York, p. 345–404.
- Kent, P. E., 1979, The emergent Hormuz salt plugs of Southern Iran: Journal of Petroleum Geology, v. 2, p. 117-144.
- Kestin, J., and Shankland, I. R., 1984, Viscosity of aqueous NaCl solutions in the temperature range 25-100° C and in the pressure range 0.1-30 MPa: International Journal of Thermophysics, v. 5, p. 241-262.

Koefoed, O., and de Voogd, N., 1980, The linear properties of thin layers, with an application to synthetic seismograms over coal seams: *Geophysics*, v. 45, p. 1254-1268.

Koyi, H. A., 2001, Modeling the influence of sinking anhydrite blocks on salt diapirs targeted for hazardous waste disposal: *Geological Society of America Bulletin*, v. 29, p. 387-390.

Kupfer, D. H., 1968, Relationship of internal to external structure of salt domes, in Braunstein, J., and O'Brien, G. D., eds., *Diapirism and diapirs*, American Association of Petroleum Geologists Memoir, v. 8, p. 79-89.

Kupfer, D. H., 1990, Anomalous features in the Five Islands salt stocks, Louisiana: *Transactions of the Gulf Coast Association of Geological Societies*, v. 40, p. 425-437.

Land, L. S., 1995, Na-Ca-Cl saline formation waters, Frio Formation (Oligocene) south Texas, USA: products of diagenesis, *Geochimica et Cosmochimica Acta*, v. 59, p. 2163-2174.

Land, L. S., Kupecz, J. A., and Mack, L. E., 1988, Louann salt geochemistry (Gulf of Mexico sedimentary basin, U. S. A.): a preliminary synthesis, *Chemical Geology*, v. 74, p. 25-35.

- Land, L. S., and Prezbindowski, D. R., 1981, The origin and evolution of saline formation water, lower Cretaceous carbonates, south-central Texas, U. S. A.: *Journal of Hydrology*, v. 54, p. 51-74.
- Laubscher, H. P., 1961, Die Fernschubhypothese der Jurafaltung: *Eclogae Geologicae Helvetiae*, v. 54, p. 221-282.
- Levorsen, A. I., 1967, *Geology of Petroleum*, W. H. Freeman and Company, 724 p.
- Lewis, S., and Holness, M., 1996, Equilibrium halite-H<sub>2</sub>O dihedral angles: high rock salt permeability in the shallow crust?: *Geology*, v. 24, p. 431-434.
- Lipscomb, G. G., and Denn, M. M., 1984, Flow of bingham fluids in complex geometries: *Journal of Non-Newtonian Fluid Mechanics*, v. 14, 337-346.
- Lister, G. S., and Snoke, A. W., 1984, S-C Mylonites: *Journal of Structural Geology*, v. 6, p. 617-638.
- Lohmann, H. H., 1972, Salt dissolution in the subsurface of British North Sea as interpreted from seismograms: *American Association of Petroleum Geologists Bulletin*, v. 56, p. 472-479.
- Lux, K.-H., 2005, Long-term behaviour of sealed liquid-filled salt cavities – a new approach for physical modeling and numerical simulation – basics from theory and lab investigations: *Erdöl Erdgas Kohle*, v. 121, p. 414-422.

- Macrae, G. and Watkins, J. S., 1992, Evolution of Destin dome, offshore Florida, north-eastern Gulf of Mexico: *Marine and Petroleum Geology*, v. 9, p. 501-509.
- Mandl, G., 1988, *Mechanics of Tectonic Faulting*: Amsterdam, Elsevier, *Developments in Structural Geology*, v. 1, 407 pp.
- Massimi, P., Quarteronia, A., Saleri, F., and Scrofani, G., 2007, Modeling of salt tectonics: *Computational Methods in Applied Mechanics and Engineering*, v. 197, p. 281-293.
- Marfurt, K., and R., Kirlin, 2001, Narrow-band spectral analysis and thin-bed tuning, *Geophysics*, v. 66, pp 1274-1283.
- Mauduit, T. and Brun, J. P., 1998, Growth fault/rollover systems: birth, growth, decay: *Journal of Geophysical Research*, v. 103, p. 18,119-18,136.
- McBride, E. F., Land, L. S., and Mack, L. E., 1987, Diagenesis of eolian and fluvial feldspathic sandstones, Norphlet Formation (Upper Jurassic), Rankin County, Mississippi, and Mobile County, Alabama: *American Association of Petroleum Geologists Bulletin*, v. 71, p. 1019-1034.
- McBride, B. C., Weimer, P., and Rowan, M. G., 1998, The effect of allochthonous salt on the petroleum systems of northern Green Canyon and Ewing Bank (offshore Louisiana), northern Gulf of Mexico: *American Association of Petroleum Geologists Bulletin*, v. 82, 1083-1112.

- McDonnell, A., Hudec, M. R., and Jackson, M. P. A., 2008, Distinguishing salt welds from shale detachments on the inner Texas shelf, western Gulf of Mexico: *Basin Research*, v. 21, pp 47-59.
- Means, W. D., 1989, Stretching faults: *Geology*, v. 17, p. 893-896.
- Meckel, L. D., and Nath, A. K., 1977, Geologic considerations for stratigraphic modeling and interpretation: *American Association of Petroleum Geologists Special Memoir 26*, p. 417-438.
- Meisling, K. E., Cobbold, P. R., and Mount, V. S., 2001, Segmentation of an obliquely rifted margin, Campos and Santos basins, southeastern Brazil: *American Association of Petroleum Geologists Bulletin*, v. 85, p. 1903 - 1924.
- Miralles, L., Sans, M., Galí, S., Santanach, P., 2001, 3-D rock salt fabrics in a shear zone (Súria Anticline, South-Pyrenees): *Journal of Structural Geology*, v. 23, p. 675-691.
- Moffatt, H. K., 1964, Viscous and resistive eddies near a sharp corner: *Journal of Fluid Mechanics*, v. 18, p. 1-18.
- Mohriak, W. U., Macedo, J. M., Castellani, R. T., Rangel, H. D., Barros, A. Z. N., Latge, M. A. L., Ricci, J. A., Mizusaki, A. M. P., Szatmari, P., Demercian, L. S., Rizzo, J. G., and Aires, J. R., 1995, Salt tectonics and structural styles in the deep-water province of the Cabo Frio region, Rio de Janeiro,

- Brazil, in Jackson, M. P. A., Roberts, D. G., and Snelson, S., eds., Salt Tectonics: a global perspective: American Association of Petroleum Geologists Memoir, v. 65, p. 273 - 304.
- Muir-Wood, R., and King, G. C. P., 1993, Hydrologic signatures of earthquake strain: Journal of Geophysical Research, v. 98B, p. 22035-22068.
- Murray, G. E., 1966, Salt structures of the Gulf of Mexico basin – a review: American Association of Petroleum Geologists Bulletin, v. 50, p. 439-478.
- Neidell, N. S., and Poggiagliolmi, E., 1977, Stratigraphic modeling and interpretation – Geophysical principles and techniques: American Association of Petroleum Geologists Special Memoir 26, p. 389-416.
- Niemann, J. C., 1997, Gulf of Mexico subsalt deformation zones: weak formation integrity rather than anomalous high pressure zones: Transactions of the Gulf Coast Association of Geological Societies, v. 42, p. 403-411.
- Nettleton, L. L., 1934, Fluid mechanics of salt domes: American Association of Petroleum Geologists Bulletin, vol. 18, p. 1175 – 1204.
- O'Connor, S. J., 2001, Hydrocarbon-water interfacial tension values at reservoir conditions: inconsistencies in the technical literature and the impact on maximum oil and gas column height considerations: American Association of Petroleum Geologists Bulletin, v. 84, p. 1537-1541.

- Odé, H., 1968, Review of mechanical properties of salt relating to salt-dome genesis, in Braunstein, J., and O'Brien, G. D., eds., Diapirs and diapirism: American Association of Petroleum Geologists Memoir, v. 8, p. 53-78.
- Orange, D. L., Saffer, D., Jeanjean, P., Al-Khafaji, Z., Humphrey, G., and Riley, G., 2003, Measurements and modeling of the shallow pore pressure regime at the Sigsbee Escarpment: successful prediction of overpressure and ground-truthing with borehole measurements: The Leading Edge, v. 22, p. 906-913.
- Partyka, G. A., Gridley, J. A., and Lopez, J. A., 1999, Interpretationl aspects of spectral decomposition in reservoir characterization: The Leading Edge, v. 18, p. 353-360.
- Peach, C. J., and Spiers, C. J., 1996, Influence of crystal plastic deformation on dilatancy and permeability development in synthetic salt rock: Tectonophysics, v. 256, p. 101-128.
- Peel, F. J., Travis, C. J., and Hossack, J. R., 1995, Genetic structural provinces and salt tectonics of the Cenozoic offshore U. S. Gulf of Mexico: a preliminary analysis, in Jackson, M. P. A., Roberts, D. G., and Snelson, S., eds., Salt Tectonics: a global perspective: American Association of Petroleum Geologists Memoir, v. 65, p. 153-175.

- Pequeno, M. A., 2009, Albian/Maastrichtian tectono-stratigraphic evolution of central Santos Basin, offshore Brazil, University of Texas at Austin Dissertation.
- Pinto, A. C. C., Branco, C. C. M., de Matos, J. S., Vieira, P. M., da Silva Guedes, S., Pedroso Jr., C., Coelho, A. C. D., and Ceceliano, M. M., 2003, Offshore heavy oil in Campos Basin: the Petrobras experience: Offshore Technology Conference, Houston, Texas, p. 1-12.
- Popp, T., Kern, H., and Schulze, O., 2001, Evolution of dilatancy and permeability in rock salt during hydrostatic compaction and triaxial deformation: *Journal of Geophysical Research*, v. 106, p. 4061-4078.
- Pratson, L. F., and Haxby, W. F., 1996, What is the slope of the U. S. continental margin?: *Geology*, v. 24, p. 3–6.
- Price, R. H., 1982, Effects of anhydrite and pressure on the mechanical behavior of synthetic rocksalt: *Geophysical Research Letters*, v. 9, p. 1029–1032.
- Puryear, C. I., and Castagna, J. P., 2006, An algorithm for calculation of thin bed thickness and reflection coefficients from amplitude spectrum: 76<sup>th</sup> Annual International Meeting of the Society of Exploration Geophysicists, p. 1767-1770.

- Raymer, D. G., Tommasi, A., and Kendall, J-M, 2000, Predicting the seismic implications of salt anisotropy using numerical simulations of halite deformation: *Geophysics*, v. 65, p. 1272-1280.
- Ricker, N., 1953, Wavelet shortening, wavelet expansion, and the control of seismic resolution: *Geophysics*, v. 18, pp 769-772.
- Roberts, M. J., Metzgar, C. R., Liu, J., and Lim, S. J., 2004, Regional assessment of salt weld timing, Campos Basin, Brazil, in Post, P. J., Olson, D. L., Lyons, K. T., Palmes, S. L., Harrison, P. F., and Rosen, N. C., eds., *Salt-sediment interactions and hydrocarbon prospectivity: concepts, applications, and case studies for the 21st century*, 24th Annual Gulf Coast Section Society of Economic Paleontologists and Mineralogists Foundation Bob F. Perkins Research Conference, p. 371–389.
- Ross, J. V., Bauer, S. J. and Hansen, F. D., 1987, Textural evolution of synthetic anhydrite-halite mylonites: *Tectonophysics*, v. 140, p. 307-326.
- Ross J. V. and Bauer, S. J., 1992, Semi-brittle deformation of anhydrite-halite shear zones simulating mylonite formation: *Tectonophysics*, v. 213, p. 303-320.
- Rouby, D., Raillard, S., Guillocheau, F., Bouroullec, R., Nalpas, T., 2002, Kinematics of a growth fault/raft system on the West African margin using 3D restoration: *Journal of Structural Geology*, v. 24, p. 783-796.

- Rowan, M. G., 1995, Structural styles and evolution of allochthoous salt, central Louisiana outer shelf and upper slope, in Jackson, M. P. A., Roberts, D. G., and Snelson, S., eds., Salt Tectonics: a global perspective: American Association of Petroleum Geologists Memoir, v. 65, p. 199-228.
- Rowan, M. G., 1993, A systematic technique for the sequential restoration of salt structures: Tectonophysics, v. 228, p. 331-348.
- Rowan, M. G., 2004, Do salt welds seal? in Post, P. J., Olson, D. L., Lyons, K. T., Palmes, S. L., Harrison, P. F., and Rosen, N. C., eds., Salt-sediment interactions and hydrocarbon prospectivity: concepts, applications, and case studies for the 21st century, 24th Annual Gulf Coast Section Society of Economic Paleontologists and Mineralogists Foundation Bob F. Perkins Research Conference, p. 390–403.
- Rowan, M. G., and Weimer, P., 1998, Salt-sediment interaction, northern Green Canyon and Ewing Bank (offshore Louisiana), northern Gulf of Mexico: American Association of Petroleum Geologists Bulletin, v. 82, p. 1055-1082.
- Rowan, M. G., Jackson, M. P. A., and Trudgill, B. D., 1999, Salt-related fault families and fault welds in the northern Gulf of Mexico: American Association of Petroleum Geologists Bulletin, v. 83, p. 1454.

- Rowan, M. G., Lawton, T. F., Giles, K. A., and Ratliff, R. A., 2003, Near-salt deformation in La Popa basin, Mexico, and the northern Gulf of Mexico: a general model for passive diapirism: *American Association of Petroleum Geologists Bulletin*, v. 87, p. 733-756.
- Rubin, T., Johnston, H. L., and Altman, H. W., 1961, Thermal expansion of rock salt: *Journal of Physical Chemistry*, v. 65, p. 65-68.
- Rubino, J. G., Velis, D., 2009, Thin-bed prestack spectral inversion: *Geophysics*, v. 74, p. R49-R57.
- Salvador, A., 1987, Late Triassic-Jurassic paleogeography and origin of the Gulf of Mexico basin: *American Association of Petroleum Geologists Bulletin*, v. 71, p. 419-451.
- Sarkar, A., Nunn, J. A., and Hanor, J. S., 1995, Free thermohaline convection beneath allochthonous salt sheets: An agent for salt tectonics and fluid flow in Gulf Coast sediments, in C. J. Travis, H. Harrison, M. R. Hudec, B. C. Vendeville, F. J. Peel and B. F. Perkins, eds., *Salt, Sediment and Hydrocarbons*, 16<sup>th</sup> Annual Research Conference Gulf Coast Section Society of Economic Paleontologists and Mineralogists , p. 245-252.
- Schlöder, Z., Urai, J. L., Nolle, S., and Hilgers, C., 2008, Solution-precipitation creep and fluid flow in halite: a case study in Zechstein (Z1) rocksalt form

- Neuhof salt mine (Germany): *International Journal of Earth Science*, v. 97, p. 1045-1056.
- Schenk, O., and Urai, J. L., 2004, Microstructural evolution and grain boundary structure during static recrystallization in synthetic polycrystals of sodium chloride containing saturated brine: *Contributions to Mineralogy and Petrology*, v. 146, p. 671-682.
- Schoenherr, J., Urai, J. L., Kukla, P. A., Littke, R, Schléder, Z., Larroque, J., Newall, M., Al-Abry, N., Al-Siyabi, H. A., and Rawahi, Z., 2007, Limits to the sealing capacity of rock salt: A case study of the infra-Cambrian Ara Salt from the South Oman salt basin: *American Association of Petroleum Geologists Bulletin*, v. 91, p. 1541-1557.
- Schulze, O., Popp, T, and Kern, H., 2001, Development of damage and permeability in deforming rock salt: *Engineering Geology*, v. 61, p. 163-180.
- Schultz-Ela, D. D., 2003, Origin of drag folds bordering salt diapirs: *American Association of Petroleum Geologists Bulletin*, v. 87, p. 757-780.
- Schuster, D. C., 1995, Deformation of allochthonous salt and evolution of related salt-structural systems, eastern Louisiana Gulf Coast, in Jackson, M. P. A., Roberts, D. G., and Snelson, S., eds., *Salt Tectonics: a global*

- perspective: American Association of Petroleum Geologists Memoir, v. 65, p. 177-198.
- Schwerdtner, W. M., and Clark, A. R., 1967, Structural analysis of Mokka Fiord and South Fiord Domes, Axel Heiberg Island, Canadian Arctic: Canadian Journal of Earth Sciences, v. 4, p. 1229–1245.
- Seni, S. J., and Jackson, M. P. A., 1983, Evolution of salt structures, east Texas diapir province, part 1: sedimentary record of halokinesis, American Association of Petroleum Geologists Bulletin, v. 67, p. 1219-1244.
- Smith, D. A., 1966, Theoretical considerations of sealing and non-sealing faults: American Association of Petroleum Geologists Bulletin, v. 50, p. 363-374.
- Sok, R. M., 1994, Permeation of small molecules across a polymer membrane: a computer simulation study [Ph. D. Thesis]: Rijksuniversiteit Groningen, 136 p.
- Spiers, C. J., Schutjens, P. M. T. M., Brzesowsky, R. H., Peach, C. J., Liezenberg, J. L., and Zwart, H. J., 1990, Experimental determination of constitutive parameters governing creep of rocksalt by pressure solution, in Knipe, R. J., and Rutter, E. H., eds., Deformation Mechanisms, Rheology, and Tectonics: Geological Society, London, Special Publications, v. 54, p. 215-227.

- Strohmenger, C., Voigt, E., Zimdars, J, 1996, Sequence stratigraphy and cyclic development of Basal Zechstein carbonate-evaporite deposits with emphasis on Zechstein 2 off-platform carbonates (Upper Permian, Northeast Germany): *Sedimentary Geology*, v. 102, p. 33-54.
- Sun, L., Xiadong, Z., Jingsong, L., and Hao, S., 2009, Thin-bed thickness calculation formula and its approximation using peak frequency, *Applied Geophysics*, v. 6, p. 234-240.
- Sun, Z., 1994, Seismic anisotropy in salt from theoretical study, modelling, and field experiments: M. Sc. thesis, University of Calgary.
- Talbot, C. J., 1979, Fold trains in a glacier of salt in Southern Iran: *Journal of Structural Geology*, v. 1, p. 5-18.
- Talbot, C. J., 1968, Thermal convection in the Archean crust?: *Nature*, v. 220, p. 552-556.
- Talbot, C. J., 1999, Ductile shear zones as counterflow boundaries in pseudoplastic fluids: *Journal of Structural Geology*, v. 21, p. 1535-1551.
- Talbot, C. J., Aftabi, P., 2004. Geology and models of salt extrusion at Qum Kuh, central Iran: *Journal of the Geological Society, London*, 161, 321–334.
- Talbot, C. J., and Jackson, M. P. A., 1987, Internal kinematics of salt diapirs: *American Association of Petroleum Geologists Bulletin*, v. 71, p. 1068-1093.

- Talbot, C. J., and Jackson, M. P. A., 1989, Internal kinematics of salt diapirs: reply, *American Association of Petroleum Geologists Bulletin*, v. 73, p. 946-950.
- Talbot, C. J., and Jarvis, R. J., 1984, Age, budget and dynamics of an active salt extrusion in Iran: *Journal of Structural Geology*, v. 6, p. 521-533.
- Talbot, C. J., Medvedev, S., Alavi, M. Alavi, Shahrivar, H., and Heidari, E., 2000, Salt extrusion rates at Kuh-e-Jahani, Iran: June 1994 to November 1997, in Vendeville, B. C., Y. Mart, and J. L. Vigneresse, eds., *Salt, shale and igneous diapirs in and around Europe: Geological Society of London, Special Publications*, 174, p. 93–110.
- Talbot, C. J., and Rogers, E. A., 1980, Seasonal movements in a salt glacier in Iran: *Science*, v. 208, p. 395-397.
- Ter Heege, J. H., De Bresser, J. H. P., Spiers, C. J., 2005a, Dynamic recrystallization of wet synthetic polycrystalline halite: dependence of grain size distribution on flow stress, temperature and strain: *Tectonophysics*, v. 396, p. 35-57.
- Ter Heege, J. H., De Bresser, J. H. P., Spiers, C. J., 2005b, Rheological behavior of synthetic rocksalt: the interplay between water, dynamic recrystallization and deformation mechanisms: *Journal of Structural Geology*, v. 27, p. 948-963.

Trudgill, B., Banbury, N., and Underhill, J., 2004, Salt evolution as a control on structural and stratigraphic systems: northern Paradox Foreland Basin, southeast Utah, USA in Post, P. J., Olson, D. L., Lyons, S. L., Palmes, P. F., Harrison, P. F., and Rosen, N. C., eds., Salt-sediment interactions and hydrocarbon prospectivity: concepts, applications, and case studies for the 21st century, 24th Annual Research Conference Gulf Coast Section Society of Economic Paleontologists and Mineralogists, p. 705-734.

Trusheim, F., 1960, Mechanism of salt migration in Northern Germany: American Association of Petroleum Geologists Bulletin, v. 44, p. 1519-1540.

Tucker, M. E., 1991, Sequence stratigraphy of carbonate-evaporite basins: models and application to the Upper Permian (Zechstein) Of northeast England and adjoining North Sea: Journal of the Geological Society, London, v. 148, p. 1019-1036.

Turcotte, D. I., and Schubert, G., 1982, Geodynamics: Applications of Continuum Physics to Geological Problems, New York, Wiley, 459 p.

Urai, J., Spiers, C. J., Zwart, H., and Lister, G., 1986, Weakening of rock salt by water during long-term creep: Nature, v. 324, p. 554–556.

Urai, J. L., Spiers, C. J., Peach, C. J., Franssen, R. C. M. W., and Liezenberg, J. L., 1987, Deformation mechanisms in naturally deformed halite rocks as

- deduced from microstructural investigations: *Geologie en Mijnbouw*, 66, 165–176.
- Usiglio, J., 1849, *Analyse de l'eau de la Méditerranée sur les côte de France*: *Annales des Chimie et des Physique*, v. 27, p. 92-108.
- van Keken, P. E., Spiers, C. J., van den Berg, A. P., and Muyzert, E. J., 1993, The effective viscosity of rocksalt: implementation of steady-state creep laws in numerical models of salt diapirism: *Tectonophysics*, v. 225, p. 457–476.
- Vendeville, B., and Jackson, M. P. A., 1992a, The rise of diapirs during thin-skinned extension: *Marine and Petroleum Geology*, v. 9, p. 331–353.
- Vendeville, B., and Jackson, M. P. A., 1992b, The fall of diapirs during thin-skinned extension: *Marine and Petroleum Geology*, v. 9, p. 354–371.
- Vendeville, B. C., Jackson, M. P. A., and Ge., H., 1993, Detached salt tectonics during basement-involved extension: *American Association of Petroleum Geologists Annual Convention*, p. 195 (abstract).
- Voronov, F. F., and Grigor'ev, S. B., 1976, Influence of pressures up to 100 kbar on elastic properties of silver, sodium, and cesium chlorides : *Soviet Physics Solid State*, v. 18, p. 325-328.
- Warren, J., 2006, *Evaporites: Sediments, Resources, and Hydrocarbons*: Springer-Verlag Berlin Heidelberg, 438 p.

- Walker, R. G., 1984, Facies models; second edition: Waterloo, Ontario, Geological Association of Canada, 317 p.
- Walker, D., Verma, P. K., Cranswick, L. M. D., Jones, R. L., Clark, S. M., and Buhre, S., 2004, Halite-sylvite thermoelasticity: *American Mineralogist*, v. 89, p. 204-210.
- Wang, C. Y., 1991, Exact solutions of the steady-state Navier-Stokes equations: *Annual Reviews in Fluid Mechanics*, v. 23, p. 159-177.
- Weber, L. J. and Sarg, J. F., 2005, Play element prediction; carbonate plays in subaqueous evaporite settings: Abstracts of the Annual Meeting of the American Association of Petroleum Geologists, v. 14, p. A150.
- Weijermars, R., 1986, Polydimethylsiloxane flow defined for experiments in fluid dynamics: *Applied Physics Letters*, v. 48, p. 109–111.
- Weijermars, R., Jackson, M. P. A. and Vendeville, B., 1993, Rheological and tectonic modeling of salt provinces: *Tectonophysics*, v. 217, p. 143-174.
- Weinberger, R., Lyakhovsky, V., Baer, G., Begin, Z. B., 2006, Mechanical modeling and InSAR measurements of Mount Sedom uplift, Dead Sea basin: implications for effective viscosity of rock salt: *Geochemistry Geophysics Geosystems*, AGU, v. 7, 20 p.
- Wenkert, D. D., 1979, The flow of salt glaciers: *Geophysical Research Letters* v. 6, p. 523-526.

- Widess, M. B., 1973, How thin is a thin bed?: *Geophysics*, v. 38, p. 1176-1180.
- Withjack, M. O., and Callaway, J. S., 2000, Active normal faulting beneath a salt layer -- an experimental study of deformation in the cover sequence: *American Association of Petroleum Geologists Bulletin*, v. 84, p. 627-651
- Willis, J. J., Lock, B. E., Cornell, K C., Ruberg, D. A., 2001, An exposed evaporite weld and related deformational structures, Edwards Plateau, I-10 corridor, Kerrville-Junction-Sonora area, Texas: *Transactions of the Gulf Coast Association of Geological Societies*, v. 51, p. 389-396.
- Worrall, D. M., and Snelson, S., 1989, Evolution of the northern Gulf of Mexico, with emphasis on Cenozoic growth faulting and the role of salt, in Bally, A. W., ed., *The geology of North America: Boulder, Geological Society of America*, p. 97-138.
- Yaramanci, U., 1994, Relation of in situ resistivity to water content in salt rocks: *Geophysical Prospecting*, v. 41, p. 229-239.
- Yiantsios, S. G., and Higgins, B. G., 1988, Linear stability of plane Poiseuille flow of two superposed fluids: *Physics of Fluids*, v 31, p. 3225-3238.
- Zak, I., and Freund, R., 1980, Strain measurements in eastern marginal shear zone of Mount Sedom salt diapir, Israel: *American Association of Petroleum Geologists Bulletin*, v. 64, p. 568-581.

Zulauf, G., Zulauf, J., Bornemann, O., Kihm, N., Peini, M., and Zanella, F., 2009,  
Experimental deformation of a single-layer anhydrite in halite matrix under  
bulk constriction. Part 1: geometric and kinematic aspects, *Journal of  
Structural Geology*, v. 31, p. 460-474.

## **Vita**

Bryce Hedrick Wagner III was born in Kansas City, Missouri and grew up on a small farm outside Lathrop, Missouri. After graduating from Lathrop High School, he enrolled in the Department of Geology and Geophysics at the University of Missouri in Rolla, Missouri (now the Missouri University of Science and Technology). He graduated Summa Cum Laude with a Bachelor of Science degree in May, 2006. In August 2006, he entered the Jackson School of Geosciences at the University of Texas at Austin. His research interests include salt tectonics, structural geology, and exploration geophysics.

Permanent Address:       705 Golden Bear Lane  
  McKinney, TX 75070

This thesis was typed by the author.